Spring 5-7-2021

FACILE SYNTHESIS OF METAL OXIDES, SULPHIDES, AND PHOSPHIDES FOR ENHANCED ENERGY APPLICATIONS

Alfred Nkhama
Pittsburg State University, ankhama@gus.pittstate.edu

FACILE SYNTHESIS OF METAL OXIDES, SULPHIDES, AND PHOSPHIDES FOR ENHANCED ENERGY APPLICATIONS

A Thesis Submitted to the Graduate School
in Partial Fulfillment of the Requirements
for the Degree of Master of Science

Alfred Emil Nkhama

Pittsburg State University

Pittsburg, Kansas

May, 2021

FACILE SYNTHESIS OF METAL OXIDES, SULPHIDES AND PHOSPHIDES
FOR ENHANCED ENERGY APPLICATIONS

Alfred Emil Nkhama

APPROVED:

Thesis Advisor _____
Dr. Ram K. Gupta, Department of Chemistry

Committee member _____
Dr. Serif Uran, Department of Physics

Committee member _____
Dr. Khamis Siam, Department of Chemistry

ACKNOWLEDGEMENTS

First and foremost, I would like to thank God for the countless blessings he granted me through the entire period I have been to Pittsburg State University.

I would like to dedicate my gratitude and appreciation to my thesis advisor, Dr. Ram K. Gupta, for the enormous support and time he devoted to ensuring that I could successfully accomplish this research work; without him, it would not have been possible. His instructions, direction, and patience greatly enabled and improved my research and writing skills.

I would also like to express my thanks to my thesis committee members; Dr. Serif Uran, and Dr. Khamis Siam, for accepting the role to serve in my thesis work.

May I also take this opportunity to express my thanks to the Department of Physics, Pittsburg State University, for the support they provided to me as a graduate teaching assistant; and to the Kansas Polymer Research Center, where I conducted my research.

I also appreciate the valuable support by Jonghyun Choi, a research graduate student, with regard to this research.

And last but not least, I dedicate my thanks to Dr. Sanjay Mishra, University of Memphis, for recording SEM and XRD images of my samples.

FACILE SYNTHESIS OF METAL OXIDES, SULPHIDES, AND PHOSPHIDES
FOR ENHANCED ENERGY APPLICATIONS

An abstract of the Thesis by
Alfred Emil Nkhama

Access to a reliable, sustainable, eco-friendly, and cost-effective energy supply is being challenged by the global increase in population and rapid technological advancement. Sophisticated systems, machinery, and various devices being innovated require a steady energy supply for their operations and applicability. To have this reliable energy, much research is being conducted through various approaches across the world. In this work, a facile approach in investigating and tuning the materials' properties was employed to improve the energy properties of metal oxides. Nanostructured NiFe oxide and CoFe oxide were synthesized using a facile coprecipitation method. It was revealed that nanostructured materials have favorable structures which promote their electrochemical efficiency. The structural and electrochemical properties of oxides were studied. To further investigate their properties, they were sulfurized and phosphorized using a hydrothermal and thermal process, respectively. The sulfides and phosphides showed impressive property improvement as compared to their respective oxides. NiFe-oxide showed impressive oxygen evolution reaction and hydrogen evolution reactions with 298 mV and 54 mV overpotentials, respectively. After sulfurization, their results were further improved, except NiFe-oxide nanocubes (NiFe-NCs), whose HER overpotential was increased from 54 to 177 mV; while the rest of the samples showed

improvement of OER and HER overpotentials; from 298 for NiFe-NCs to 241 mV for NiFeS-NCs in OER, 258 for NiFe-oxide nanoparticles (NiFe-NPs) to 216 mV for NiFeS-NPs in OER; and 187 for NiFe-NPs to 152 mV for NiFeS-NPs in HER. Likewise, the materials' specific capacitance increased from 69 to 605 F/g for sulfurized NiFe-NCs and 186 to 515 F/g for sulfurized NiFe-NPs. The energy density of materials increased from 2 to 20 Wh/kg for NiFe-NCs and NiFeS-NCs, and from 6 to 17 Wh/kg for NiFe-NPs and NiFeS-NPs respectively, at 1 A/g.

CoFe oxide samples showed good electrocatalytic and storage behavior. Their overpotentials decreased from 113 for CoFe-NCs to 52 mV for CoFeS-NCs and from 161 for CoFe-NPs to 122 mV for CoFeS-NPs. Their specific capacitance was also increased: specific capacitance of CoFe-NCs increased from 123 to 484 F/g for CoFeS-NCs and 161 of CoFe-NPs to 244 F/g for CoFeS-NPs. The energy density of CoFe-NCs increased from 4 to 17 Wh/kg after sulfurization, whereas for CoFe-NPs; the energy density increased from 5 to 8 Wh/kg, at 1 A/g.

Upon phosphorization, the overpotentials values of 300, 330, 340, and 360 mV for phosphorized NiFe-nanoparticles (NiFeP-NPs), phosphorized CoFe-nanocubes (CoFeP-NCs), phosphorized NiFe-nanocubes (NiFeP-NCs) and phosphorized CoFe-nanoparticles (CoFeP-NPs) respectively, were observed, with some deviations from their unphosphorized counterparts which showed 256, 300, 298, and 300 mV overpotentials, respectively. The overpotentials for HER seemed to decrease when compared to their unphosphorized counterparts; 135, 121, 118, and 84 mV were determined for NiFeP-NPs, NiFeP-NCs, CoFeP-NPs, and CoFeP-NCs as compared to their unphosphorized samples

overpotentials of 187, 54, 161, and 113 mV respectively. Specific capacitances of phosphorized samples were significantly improved; for CoFe-NCs, it increased from 123 to 248 F/g, 161 to 464 F/g for CoFe-NPs, 69 to 424 F/g for NiFe-NCs, and 186 to 214 F/g for NiFe-NPs. At the same time, the energy densities increased after phosphorization as shown in the following order; from 4 Wh/kg for CoFe-NCs to 9 Wh/kg for CoFeP-NCs, from 5 Wh/kg for CoFe-NCs to 16 Wh/kg for CoFeP-NPs, from 2 Wh/kg for NiFe-NCs to 15 Wh/kg for NiFeP-NCs, and from 6 Wh/kg for NiFe- NPs to 7 Wh/kg for NiFeP-NPs.

The results of this study suggest that facile sulfurization and phosphorization of nanostructured NiFe oxides and CoFe oxides could significantly improve their electrocatalytic and capacitive behavior.

TABLE OF CONTENTS

LIST OF TABLES

TABLE PAGE

LIST OF FIGURES

CHAPTER I

INTRODUCTION

Following the economic growth and breakthrough innovations, the energy supply from conventional sources has been insufficient to meet the current global demand. Technological advancements in diverse areas have been going hand in hand with the increase in energy consumption. The rapid increase of new and sophisticated innovations in transport, healthcare, aerospace, telecommunication, sporting and recreation, defense and security, has necessitated the need for cutting-edge research to find energy solutions for the latest global needs.

For decades, fossil fuels have been the core source of energy. However, they are being depleted as a result of population increase and the consequent increase in consumption. This has resulted in an increase in costly hydrocarbons exploration and production from the deep sea. On top of that, carbon emissions from fossil fuels have been the source of the greenhouse effect, which has greatly changed and negatively impacted the global climate. With such challenges arising from dependence on fossil fuels as the prime global energy source, the development of new, eco-friendly, and cost-effective energy alternatives, such as hydro, wind, and geothermal energy is inevitable. Also, there are promising green energy devices including solar cells, supercapacitors,

batteries, and fuel cells. These have the advantages of high efficiency, sustainability, and low costs for processing and operations. This thesis discusses environmentally friendly energy sources in general, but a detailed study was carried out with energy conversion and storage devices.

Wind energy is the energy possessed by the moving wind. The wind impinges on the turbine blades, which in turn converts the wind's kinetic energy into mechanical energy. The rotating blades turn the shaft of the turbine. The shaft spins the generator housed within strong magnets and produces electricity. Hydro-energy or hydro power is the energy possessed by fast-moving water. The force of moving water is converted into electrical energy when water falls on the turbines. The high-speed turbines spin the generator, which produces electricity.

Geothermal energy is the energy harnessed from heat generated deep inside the earth. As a result of high temperature and pressure in the interior of the earth, superheated water in the form of steam is generated. This steam can be harnessed by drilling through the earth and can be used to generate electricity by rotating turbines which in turn spin generators. The heat drawn from the interior of the earth can also be used directly for heating households.

Solar energy is the energy harnessed from sunlight. The sun radiates a huge amount of radiant energy. Over centuries, solar energy has been used for various applications. Ancient societies used solar energy for warming, drying, and cooking. Currently, solar energy is also used in generating electricity and supplying power to remote areas without access to national power grids, and in running satellites and other

devices in space. Solar cells or photovoltaics are devices used to convert solar radiant energy into electricity. There are three categories of solar cells depending on the type of materials used for their fabrication. First-generation solar cells were the earliest solar cells to be introduced and are made from silicon. Second-generation solar cells are relatively smaller in size when compared with first-generation solar cells, with thin layers (a few micrometers thick) of semiconductor materials: hence their common name “thin-film solar cells.” The use of fewer materials lowers fabrication processing costs, which leads to lower selling prices for solar panels. The third generation of solar cells includes new materials besides silicon, such as dye-sensitized, concentrated, nano crystal, and polymer-based solar cells; these have high efficiency and are cost-effective [1].

The energy generated by these cells can be stored for future application whenever is needed. Energy storage devices include capacitors, batteries, and fuel cells. Capacitors are devices that store energy in the form of electric fields. When energy is stored in the electrical double layer formed between an electrolyte and a conductor, then such capacitor is known as an electrochemical capacitor. Supercapacitors have higher capacitance than traditional capacitors. They have high energy and power density [2].

A battery is the simplest source of electricity. Energy is generated by chemical reactions once the active components are allowed to circulate their electrons in an external circuit. Batteries are grouped into two types; primary and secondary batteries. A primary battery is the one that is used once. It is charged before it is used, and when its charge is exhausted, a battery is disposed of. A common example of primary batteries is alkaline batteries. Another type of battery is secondary batteries. Secondary batteries are

the ones that can be charged and re-used by using an applied electric current after their charge has been consumed. They are also known as rechargeable batteries. Lead-acid batteries, which are used in vehicles, and lithium-ion batteries for portable electronics are examples of secondary batteries [2, 3].

A fuel cell is a system that converts hydrogen chemical energy into electricity. Hydrogen can produce potential clean energy for powering homes, hospitals, or company buildings to be free from power shortages from the normal electrical grid supply. Fuel cells need a constant supply of reacting materials, such as hydrogen and oxygen for their continuous operation (Figure 1.1). An electrochemical reaction between hydrogen and oxygen causes the flow of electrons between one electrode and another which generates electricity. Fuel cells can have backup parts and batteries for supplying reactants or energy for start-up respectively. Reactions in the fuel cell generate energy, heat, and water [2, 4].

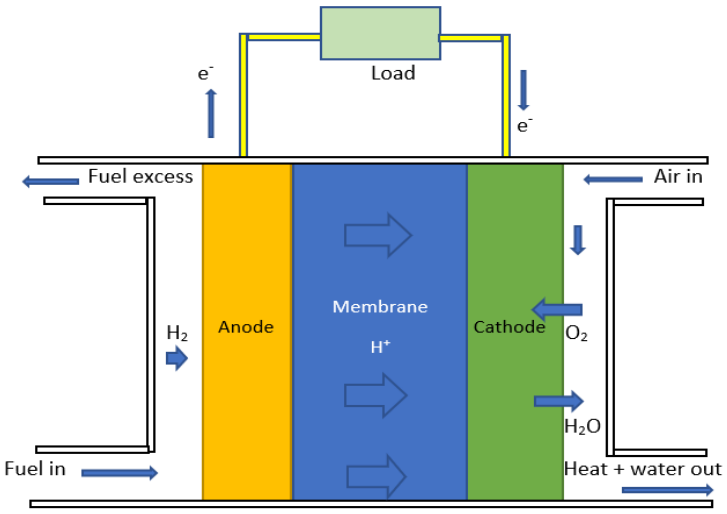

Figure 1.1: A schematic of a fuel cell.

The thesis will discuss in detail water splitting (hydrogen and oxygen evolution reactions) and supercapacitors and how the structure/phase of electrode active materials impact their electrochemical properties. Because of their high power density, supercapacitors have triggered attention among the energy-related research community. They have steady cycling and can be applied together with rechargeable batteries to supply supplemental energy needed on different occasions, such as in electrical vehicles and hybrid vehicles. This helps to safeguard rechargeable batteries from high-frequency and fast discharge-charge processes. Supercapacitors find applications in solar energy systems, wind energy systems, defense systems, aerospace, and electric vehicles [5, 6]

1.1 Conventional capacitors

Traditional capacitors are also known as condensers. They contain dielectric materials such as glass or plastic sandwiched between two conducting, oppositely charged plates (electrodes) as seen in Figure 1.2. When a potential difference is applied across the conducting plates, an electric field is created in the dielectric layer and is directly proportional to the magnitude of charges on the plates. Capacitance is the ability of a capacitor’s charge storage and is measured in Farad (F). A capacitance (C) can be calculated from the given equation below[7]

$$C= \frac{A*\varepsilon}{d} \qquad \text{………………………………………………………………} (1)$$

where *A* is the surface area of the conducting plates, ε is the permittivity of the dielectric material, and *d* is the distance between the plates.

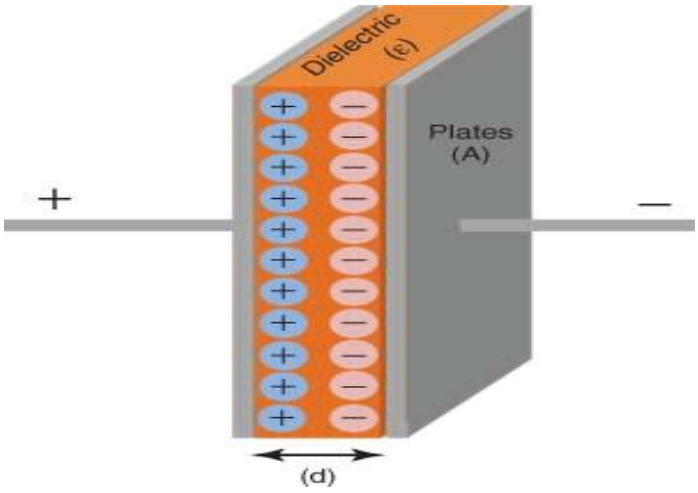

Figure 1.2: Charge alignment in a dielectric material in a charged state of conventional capacitors. Reproduced with permission from reference [7]. Copyright 2015, John Wiley and Sons.

By considering their charge storage principle, capacitors are grouped into three; supercapacitors or electric double-layer capacitors (EDLCs), pseudocapacitors, and hybrid capacitors (Figure 1.3).

1.2 Electric double-layer capacitors

Electric double-layer capacitors store electrical energy through the physical adsorption of ions at the surface of porous electrodes. The electrode and electrolyte interfaces play a major role in EDLCs energy storage. The benefit of EDLCs as compared to batteries is their rapid charging kinetics, enormous power densities, and good cycling resilience [8].

1.3 Pseudocapacitors

Apart from EDLCs, which store charge by electrostatic means, pseudocapacitors store charge Faradaically by the passage of charges between electrode and electrolyte through electrosorption or reversible redox reactions [9].

1.4 Hybrid capacitors

Hybrid capacitors are made from dissimilar electrodes. A resulting capacitor is an asymmetric one, known as a hybrid supercapacitor. Hybrid supercapacitors have shown a promising future in energy storage as compared to EDLCs [10].

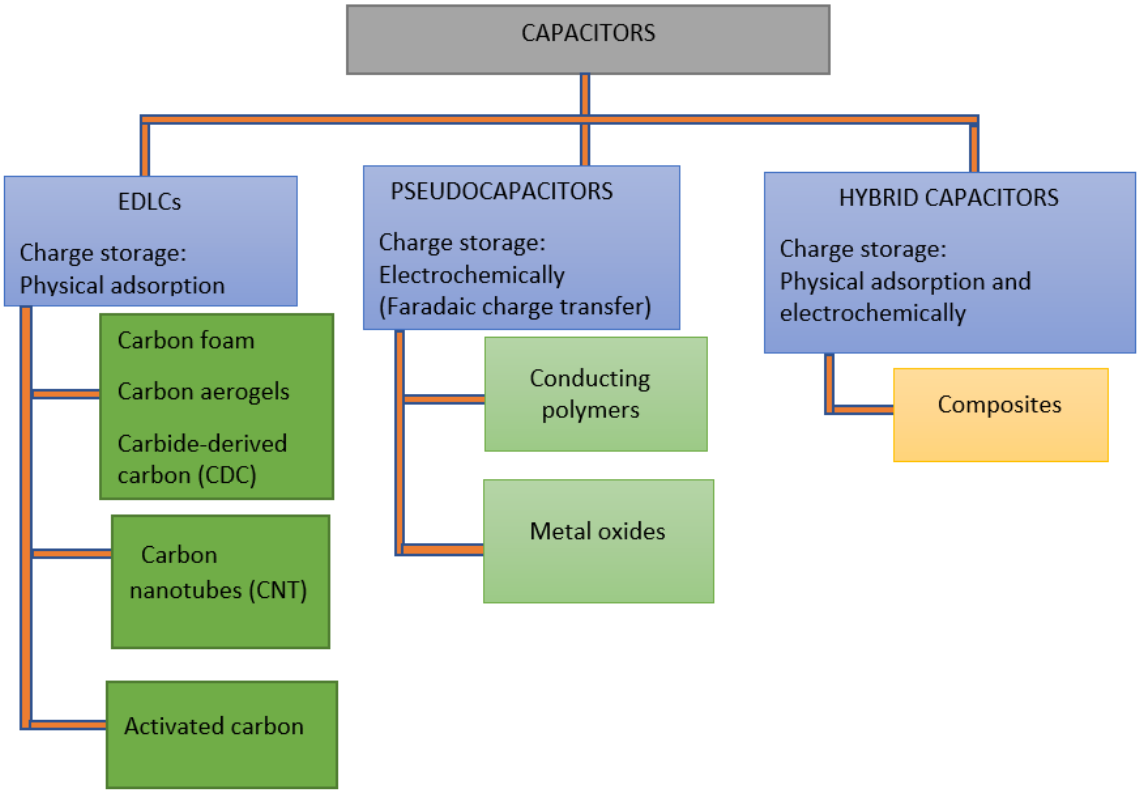

Figure 1.3: Types of capacitors and the materials used.

1.5 Specific capacitance

The specific capacitance of a capacitor is the charge stored per unit mass of the active material in the electrode, calculated by the given equation [11].

$$C_s = \frac{I\Delta t}{m\Delta V}, \quad \text{..} \ (2)$$

where C_s is the specific capacitance, Δt is the discharge time, m is the mass of the active electrode material, and I is the discharge current.

1.6 Energy and power density

The energy and power densities of a supercapacitor are important in gauging their performance for actual applications. Cyclic voltammetry (CV) and galvanostatic charge-discharge (GCD) techniques are used to evaluate both energy and power densities.

1.6.1 Energy density

Specific energy density (Wh/kg) is expressed by the equation below [7].

$$E = \frac{1}{2} C_s (\Delta V)^2 = \frac{1}{2}\frac{C}{m}(\Delta V)^2 \ \text{..} \ (3)$$

where Cs is the specific capacitance obtained from CV or GCD, and ΔV is the operating potential range

1.6.2 Power density

Specific power density (W/kg) gives the hint of how a device transfers energy per unit mass or per unit volume. The maximum specific power density is evaluated using the following equation [7].

$$P_{max} = \frac{(\Delta V)^2}{4mR_{\mathrm{ESR}}} \ \text{...} (4)$$

where ΔV is the potential range, m is the mass of the active materials, and R_{ESR} is the equivalent series resistance (ESR) of the cell. The ESR combines the ohmic resistance of the electrolytic solution and resistance offered by the cell architecture. The average power density can be calculated from the energy density using the equation below [7].

$$P_{average} = \frac{E}{\Delta t} \quad \text{.....(5)}$$

where Δt is the rate at which the cell discharges.

1.7 Ragone plot

The relationship between the power and density of energy storage and conversion devices can be viewed by plotting power density against the energy density of a device. This famous plot is known as a Ragone plot (Figure 1.4). The Ragone plot indicates the performance of a device with regard to energy and power. From this relationship, all devices show the decrease of power with the increase in energy density, including supercapacitors [7].

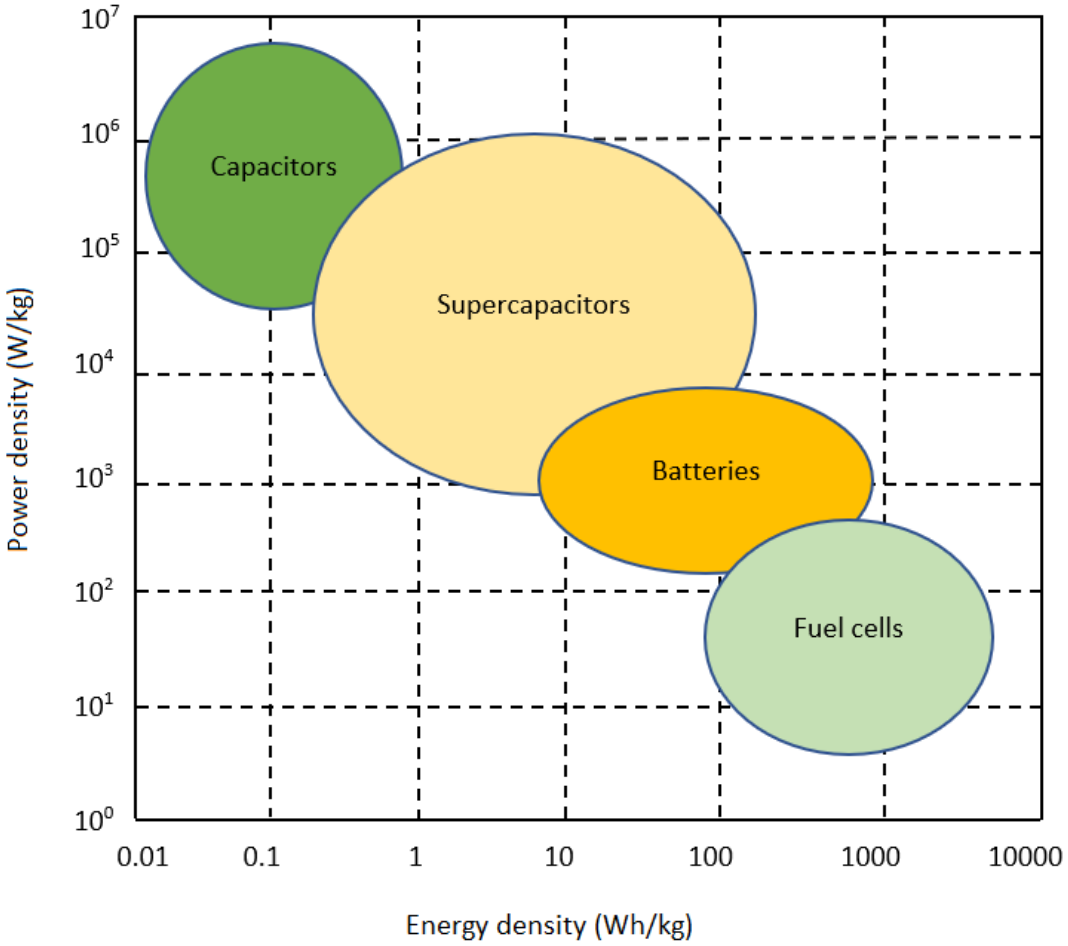

Figure 1.4: Variation of power density versus energy density. Adapted with permission from reference [7]. Copyright 2015, John Wiley and Sons.

1.8 Literature survey

Several research works have been done relating to materials phases and their energy efficiencies. We will look into some research findings and their recommendations.

Lu et al. found, "It is remarkable that many merits have been afforded by nano-engineering to promote the enhancement of supercapacitor technologies" [10]. Nanoengineered materials have unique features that render them to having favorable configurations and structures for effective kinetics and intercalation mechanisms. The

nanoengineered materials were found to have oriented mesopores that enhanced electrochemical processes and capacitive capability due to their active surfaces and interfaces. They found and realized that nano-engineering would revolutionize the future supercapacitors by optimizing and widen their usability in many more technological areas such as in lightweight durable devices and micro-energy sources in micro-electromechanical systems.

Young et al., while working with TiVCrMn alloys, found that there was a variation in hydrogen storage properties in the gaseous phase and electrochemistry by partially substituting Mn with B, Si, Ni, Zr, N, Mo, and La [12]. Except for La, the remainder of the substitutions resulted in a base-centered cube (BCC), phase. A formed phase was found to have a robust catalytic effect, observed through hydrogenation rate and highly performing electrochemical discharge capacity. The new phase (BCC-only alloy) could be used for electrochemical purposes without the need for another phase contribution with a huge discharge capacity of 247 mAh/g from a $Ti_{40}V_{30}Cr_{15}Mn_{13}Mo_2$ alloy with a catalytic hydride phase at around 0.3 MPa and an enlarged BCC unit cell.

CHAPTER II

EXPERIMENTAL DETAILS

2.1 Materials and synthesis

The starting materials needed to synthesize nanocubes (NCs) and nanoparticles (NPs) were nickel (II) nitrate hexahydrate [$Ni(NO_3)_2.6H_2O$], cobalt nitrate hexahydrate [$Co(NO_3)_2.6H_2O$], potassium hexacyanoferrate [$K_3Fe(CN)_6$], iron (III) nitrate nonahydrates [$Fe(NO_3)_3.9H_2O$], trisodium citrate dihydrate [$Na_3C_6H_5O_7.2H_20$], sodium sulfide (Na_2S), and sodium hydrophosphite monohydrate ($NaPO_2H_2.H_2O$).

2.1.1 Synthesis of NiFe oxide nanocubes

For the synthesis of NiFe-oxide nanocubes (NiFe-NCs), 1.5 mmol of $Ni(NO_3)_2.6H_2O$ and 2.25 mmol of $Na_3C_6H_5O_7.2H_2O$ were dispersed in 50 mL of distilled water to form solution A. 1 mmol of $K_3Fe(CN)_6$ was dispersed in 50 mL of deionized water to form solution B. Solutions A and B were mixed incorporating vigorous stirring for 10 minutes. The mixture was kept undisturbed at room temperature for 7 days. The product was collected by centrifugation, washed with ethanol and water, and dried at 60 °C overnight.

NiFe oxide NCs powder was calcined in air at 350 °C for 2 hours at a heating rate of 2.5 °C /min to form porous NiFe-NCs.

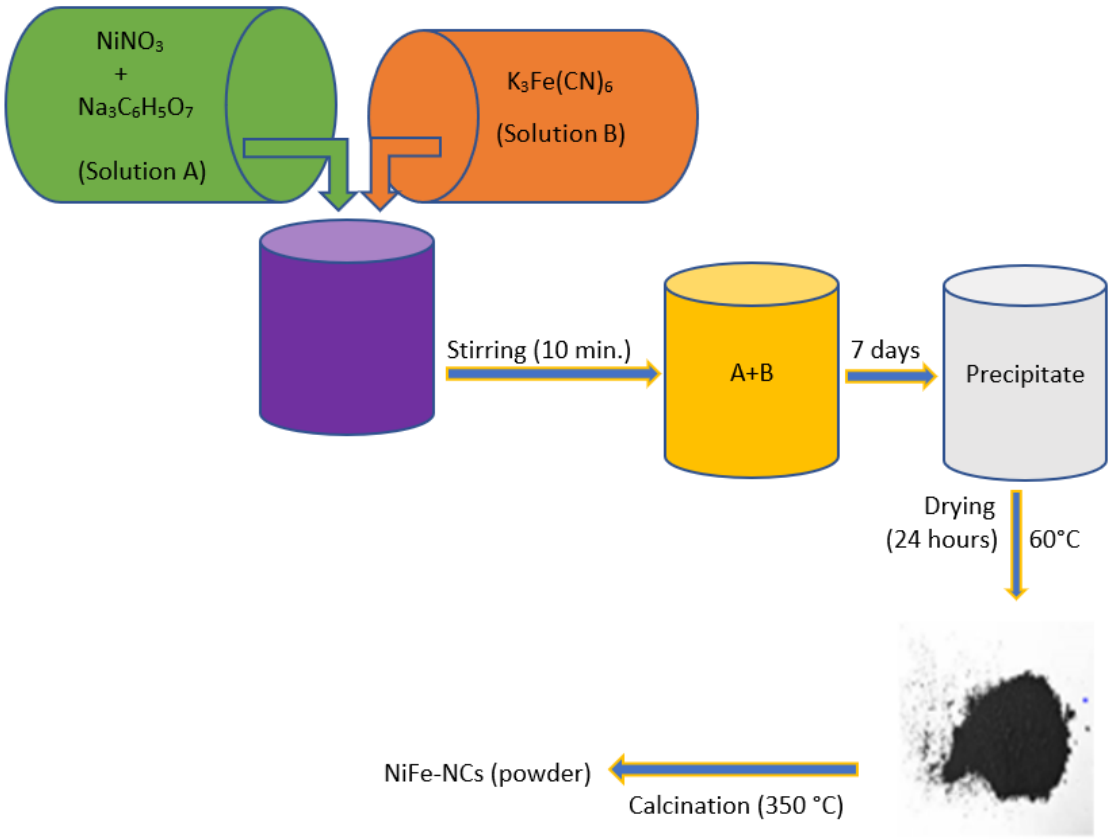

Figure 2.1: Synthesis of NiFe-NCs.

2.1.2 Synthesis of NiFe oxide nanoparticles

The materials used for the synthesis of NiFe oxide nanoparticles (NiFe-NPs) were $Ni(NO_3)_2.6H_2O$ and $Fe(NO_3)_3.9H_2O$. The homogeneous solution was obtained by dissolving 1.5 mmol of $(NiNO_3).9H_2O$ and 1 mmol of $Fe(NO_3)$ in 100 mL of deionized water. 2M NaOH was added drop by drop until a pH balance of 13 was attained. The solution was warmed at 80 °C for 60 minutes, and the resultant precipitate was collected by centrifugation, washed several times with deionized water and ethanol, and finally dried at 60 °C overnight. The dried precipitate was calcined in air at 350 °C for 2 hours in a furnace at a heating rate of 2.5 °C/min.

2.1.3 Synthesis of NiFe sulfide nanoparticles

NiFe-sulfide nanoparticles (NiFeS-NPs) were synthesized hydrothermally**.** 1.5 mmol of ($NiNO_3$).$9H_2O$ and 1 mmol of Fe(NO_3) were dissolved in 100 mL of distilled water. 2M NaOH was added drop by drop until a pH balance of 13 was attained. The solution was warmed at 80 °C for 60 minutes, and the resultant precipitate was collected by centrifugation, washed several times with deionized water and ethanol, and finally dried at 60 °C overnight. The dried precipitate was calcined in air at 350 °C for 2 hours in a furnace at a heating rate of 2.5 °C /min. 250 mg of the powder was added in 30 mL of 0.3M (700 mg) Na_2S solution in a 45 mL capacity Teflon-lined autoclave. The autoclave was sealed and maintained at 140 °C for 24 hours. After cooling to room temperature naturally, the powder was collected and, washed with deionized water and alcohol. The powder was dried in a vacuum at 60 °C for 6 hours.

2.1.4 Synthesis of NiFe sulfide nanocubes

1.5 mmol of nickel nitrate and 2.25 mmol of trisodium citrate dehydrate were dispersed in 50 mL of distilled water to form solution A. 1 mmol of potassium hexacyanoferrate was dispersed in 50 mL of distilled water to form solution B. Solutions A and B were mixed incorporating vigorous stirring for 10 minutes. The mixture was kept undisturbed at room temperature for 7 days. The product was collected by centrifugation, washed with ethanol and water, and dried at 60 °C overnight. 250 mg of the powder was added in 30 mL of 0.3M Na_2S solution in a 45 mL capacity Teflon-lined autoclave. The autoclave was sealed and maintained at 140 °C for 24 hours. After cooling to room

temperature naturally, the powder was collected and washed with distilled water and alcohol. The powder was dried in a vacuum at 60 °C for 6 hours.

Table 2.1: Materials and synthesis of NiFe nanocubes and NiFe nanoparticles.

Sample Name	**Starting materials**					
	$Ni(NO_3).6H_2O$ (mmol)	$C_6H_5Na_3O_7.2H_2O$ (mmol)	$K_3Fe(CN)_6$ (mmol)	$Fe(NO_3).9H_2O$ (mmol)	Calcination Temperature (^0C)	Heating rate (^0C/min)
NiFe-NCs	1.5	2.25	1	-	350	2.5
NiFe-NPs	1.5	-	-	1	350	2.5
NiFeS-NPs	1.5	-	-	1	-	-
NiFeS-NCs	1.5	2.25	1	-	-	-

2.2 Synthesis of CoFe nanocubes and CoFe nanoparticles

CoFe-NCs and CoFe-NPs were prepared by the same procedure used in preparing NiFe-NCs and NiFe-NPs. Their corresponding sulfides (CoFeS-NCs and CoFeS-NPs) were also synthesized using a similar hydrothermal process and the same amount of 3M Na_2S for sulfurization.

2.3 Synthesis of CoFeP-NCs, CoFeP-NPs, NiFeP-NCs, and NiFeP-NPs

To further investigate the materials' change or improvement of properties, samples were phosphorized by using sodium hypophosphite monohydrate ($NaPO_2H_2.H_2O$). Materials were doped with phosphorus at the ratio of 1:20 (sample to $NaPO_2H_2.H_2O$ ratio) at 250 °C in a tube furnace, at a heating rate of 5 °C /min for 6 hours.

2.4 Preparation of electrodes

Electrodes were prepared for each respective sample before electrochemical measurements.

2.4.1 NiFe oxide nanocubes electrode

NiFe-NCs electrodes were synthesized by using Ni foam, polyvinylidene difluoride (PVDF) polymer, N-methyl pyrrolidinone (NMP), acetylene black, and the NiFe-NCs calcined powder. The overall materials amount was 20 mg, of which 80 wt.% was NiFe-NCs powder, 10 wt.% PVDF, and 10wt%. acetylene black. PVDF's role in the solution was to steadily adhere the materials together. It has good electrochemical and thermal stability. Acetylene black is a specialty additive that provides the highest degree of structural aggregation, along with increased thermal and conductive properties. NMP was used as a solvent. It has good solvency for a wide range of organic and inorganic compounds. Ni foam was used as a substrate due to its very high porosity.

2.4.1.1 Cleaning a Ni foam

Ni foam of about 20 mm by 8 mm was drowned into 3M HCl, sonicated for 10 minutes to clean it and remove the surface oxide layer (NiO). It was then washed with deionized water and ethanol several times. The foam was dried by air pressure and further dried in a vacuum chamber for about 30 minutes.

2.4.1.2 Sample preparation

10 wt.% of the PVDF was weighed and dissolved in NMP to form a solution. The solution was mixed with 80 wt.% of NiFe-NCs powder and 10 wt.% of acetylene black. The NiFe-NCs electrode was made by dip coating the dried Ni foam in the solution. The

electrode was dried in a vacuum chamber for 48 hours before electrochemical measurements.

2.4.2 NiFe oxide nanoparticles electrode

The NiFe-NPs electrode was prepared in a similar way to the NiFe-NCs electrode. The NiFe-NPs electrode was made by dip-coating dry Ni foam in the solution. The electrode was dried in a vacuum chamber for 48 hours before electrochemical measurements.

2.4.3 NiFe sulfide nanoparticles electrode

The NiFe sulfide nanoparticles were prepared in a similar way to the NiFe-NCs electrode. The NiFeS-NPs electrode was made by dip-coating Ni foam in the solution. The electrode was dried in a vacuum chamber for 48 hours before electrochemical measurements.

2.4.4 NiFe sulfide nanocubes electrode

The NiFe-sulfide nanocubes were prepared in a similar way to the NiFe-NCs electrode. The NiFeS-NCs electrode was made by dip coating the dry Ni foam in the solution. The electrode was dried in a vacuum chamber for 48 hours before electrochemical measurements. The electrodes of CoFe-NCs, CoFe-NPs, CoFeS-NCs, CoFeS-NPs, CoFeP-NCs, CoFeP-NPs, NiFeP-NCs, NiFeP-NPs were prepared using the same procedure as the one used for NiFe samples.

2.5 Materials characterization

Characterization tools were employed in studying the features of the fabricated materials. These methods include scanning electron microscopy (SEM), X-ray diffraction (XRD), X-ray photoelectron spectroscopy (XPS), and electrochemical techniques.

2.5.1 Scanning electron microscopy

By scanning the surface of the material by using a focused beam, scanning electron microscopy generates an image of a sample. This is brought about by the interaction of the material's atoms with the electrons, generating signals that have information concerning the sample's surface compositional and topographical features (Figure 2.2). Due to its wide range of observation and resolution (nm to µm), SEM has remained to be an important tool in the area of materials science. The morphologies of the fabricated powders were studied using a JEOL JSM-840A scanning electron microscope which is mounted with an Oxford INCA 250 silicon drift X-ray energy dispersive spectrometer (EDX).

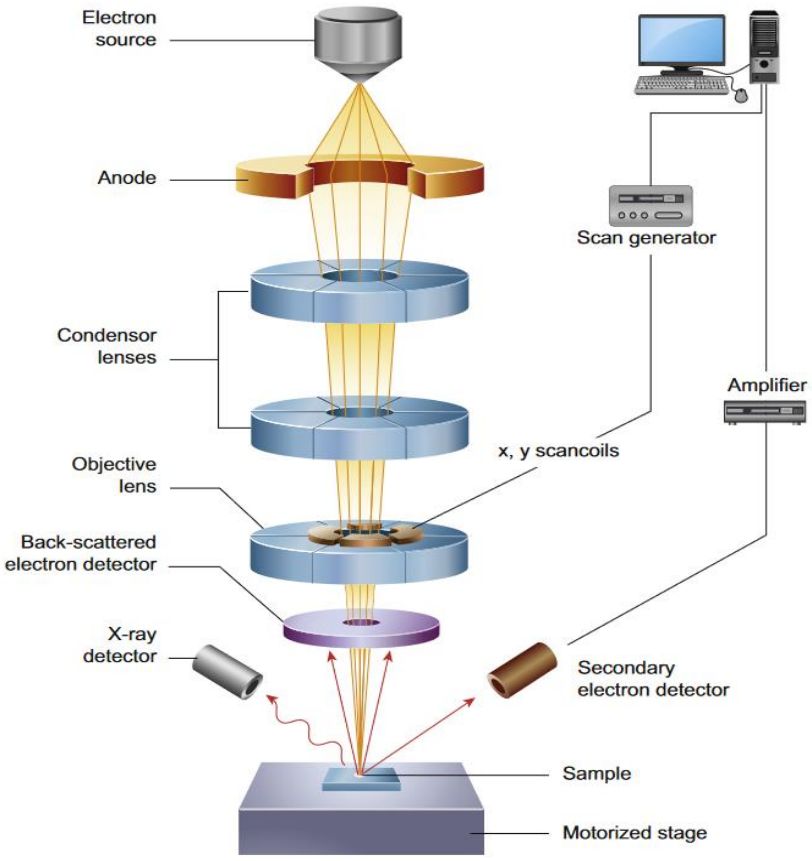

Figure 2.2: Schematic diagram of core components of a scanning electron microscope. Reproduced with permission from reference [13]. Copyright 2016, Elsevier.

2.5.2 X-ray diffraction

The structural assessment of the synthesized samples was performed by means of X-rays beams generated by an X-ray diffractometer. A Shimadzu X-ray diffractometer operating at 40 kV and a current of 30 mA was set on 2θ-θ scan with $CuK_{\alpha 1}$ (λ=1.5406 Å) rays. Diffractions patterns were obtained in the form of counts while the sample was simultaneously rotated through 2θ = 25° - 70°. To satisfy the Bragg's law conditions, the detector was placed in such a way that, the angle it subtends with atomic planes is 2θ (Figure 2.3).

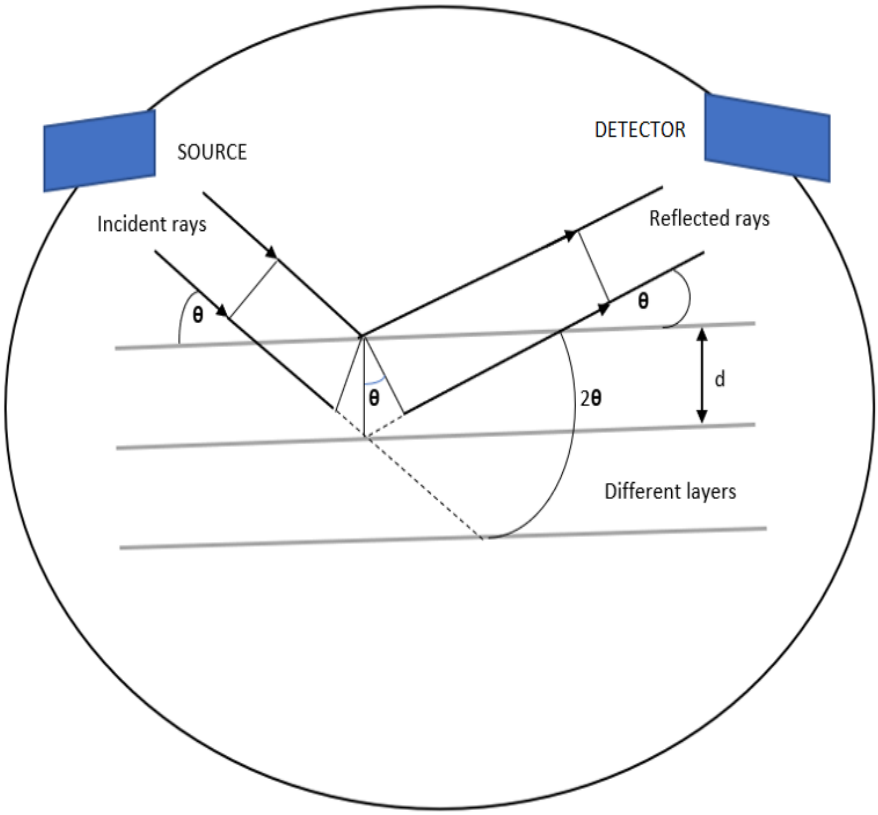

Figure 2.3: Principle of X-ray diffractometer. Adapted with permission from reference [14]. Copyright 2016, Elsevier.

2.6 Electrochemical measurements

The electrochemical characterizations were conducted to evaluate the performance of synthesized materials. Measurements were performed by using a three-cell electrode system that consisted of a working electrode (synthesized sample), a saturated calomel reference electrode, and a platinum wire counter electrode (Figure 2.4). During measurements, the potential is controlled in the working electrode (WE) while the current is measured on it. The role of the reference electrode (RE) is to measure the potential of the working electrode. The circuit of the cell is completed by the counter electrode (CE), and it conveys the current away from the solution.

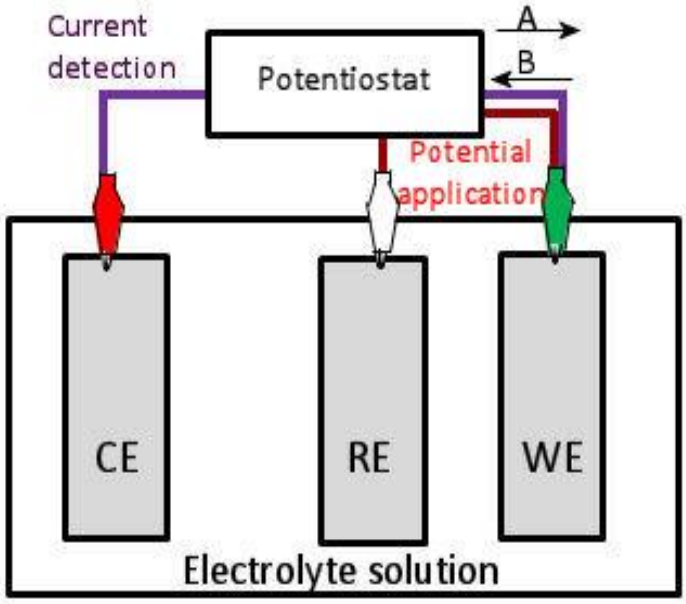

Figure 2.4: A three-cell electrode schematic diagram.

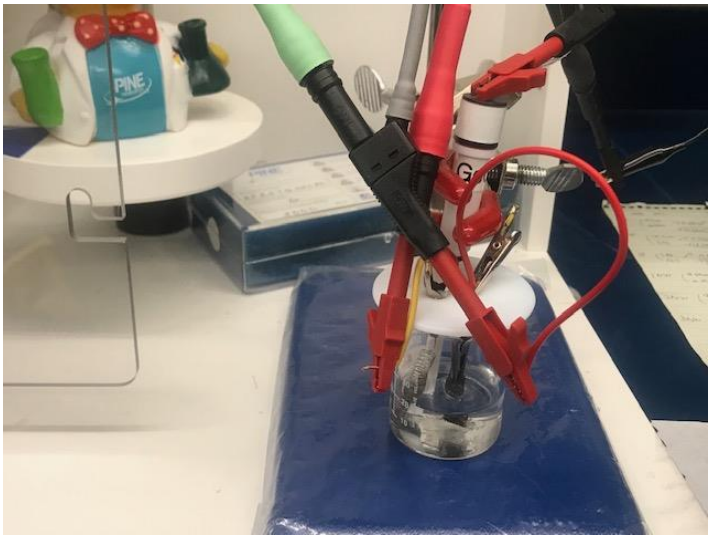

Figure 2.5: Experimental setup of three cell electrochemical measurement system.

The electrochemical tests were performed using a PARSTAT MC (AMETEK) electrochemical workstation (Princeton Applied Research, USA). Hydrogen evolution

reaction (HER), oxygen evolution reaction (OER), cyclic voltammetry, and galvanostatic charge-discharge measurements were performed to study the electrochemical behavior of the synthesized metal oxides, sulfides, and phosphides.

CHAPTER III

RESULTS AND DISCUSSION

3.1 Structural characterization

3.1.1 Scanning electron microscopic analysis

The topography and morphology of the samples were studied using a scanning electron microscope. The micro and nano scale sizes of the samples revealed that materials with small sizes (high area to volume ratio) were successfully synthesized which showed highly improved properties because of their low resistance. The SEM images for all samples are shown in the following figures.

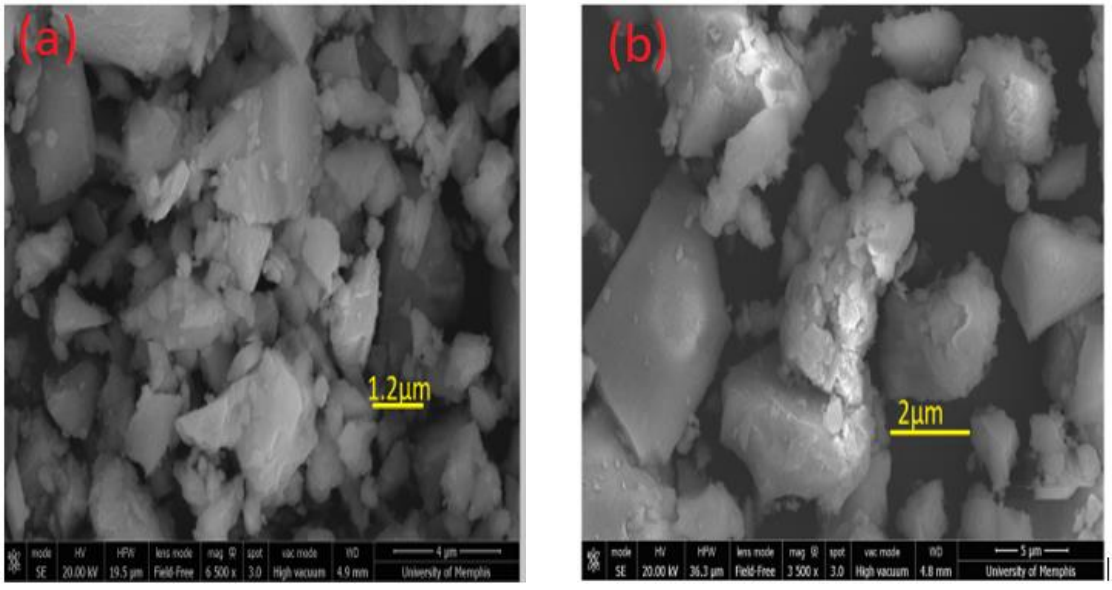

Figure 3.1: SEM images of NiFe-NPs powder at various magnifications.

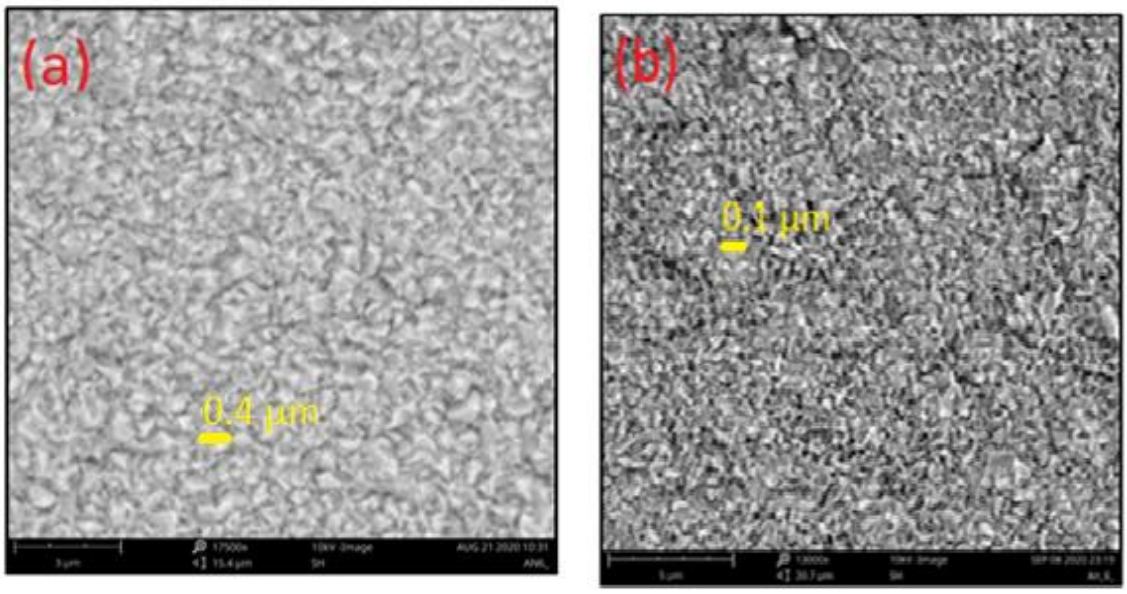

Figure 3.2: SEM images of NiFeS-NPs powder at various magnifications @Ni foam.

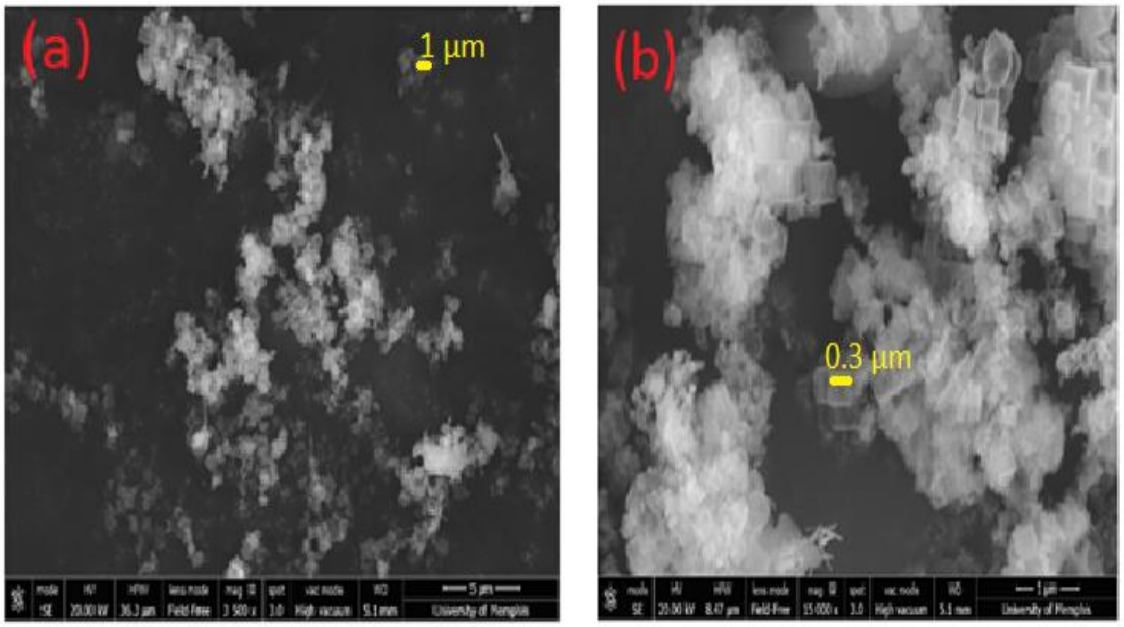

Figure 3.3: SEM images of CoFe-NCs powder at various magnifications.

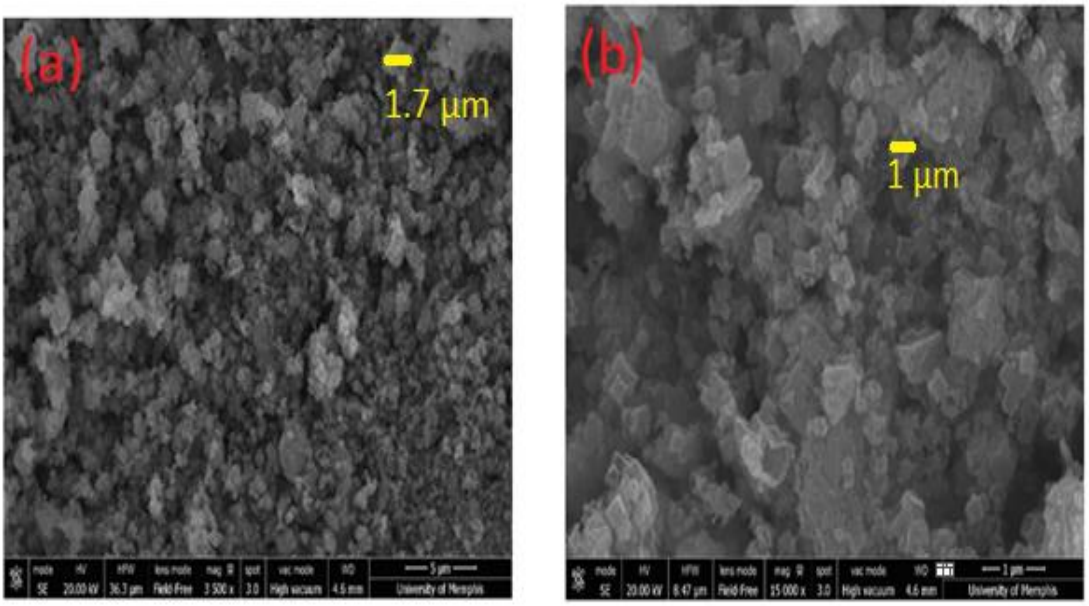

Figure 3.4: SEM images of CoFeS-NCs powder at various magnifications.

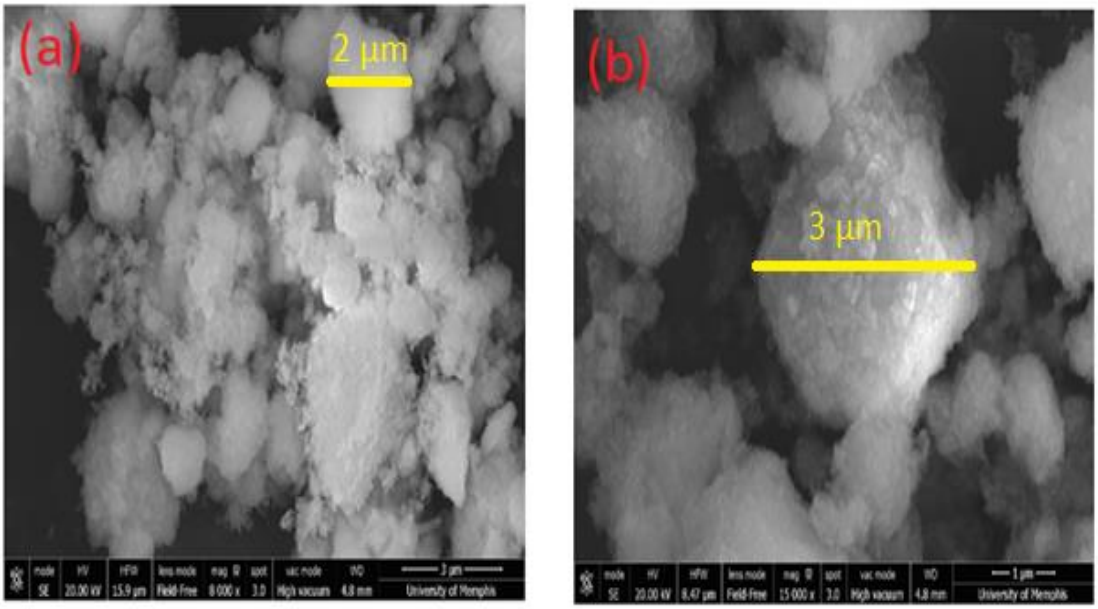

Figure 3.5: SEM images of CoFe-NPs powder at various magnifications.

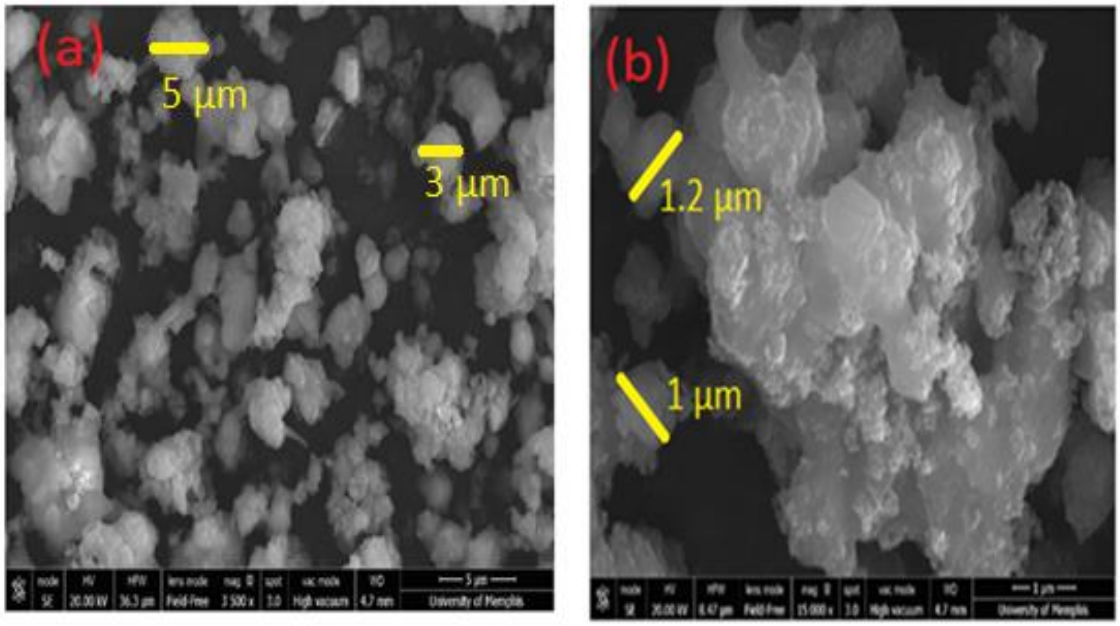

Figure 3.6: SEM images of CoFeS-NPs powder at various magnifications.

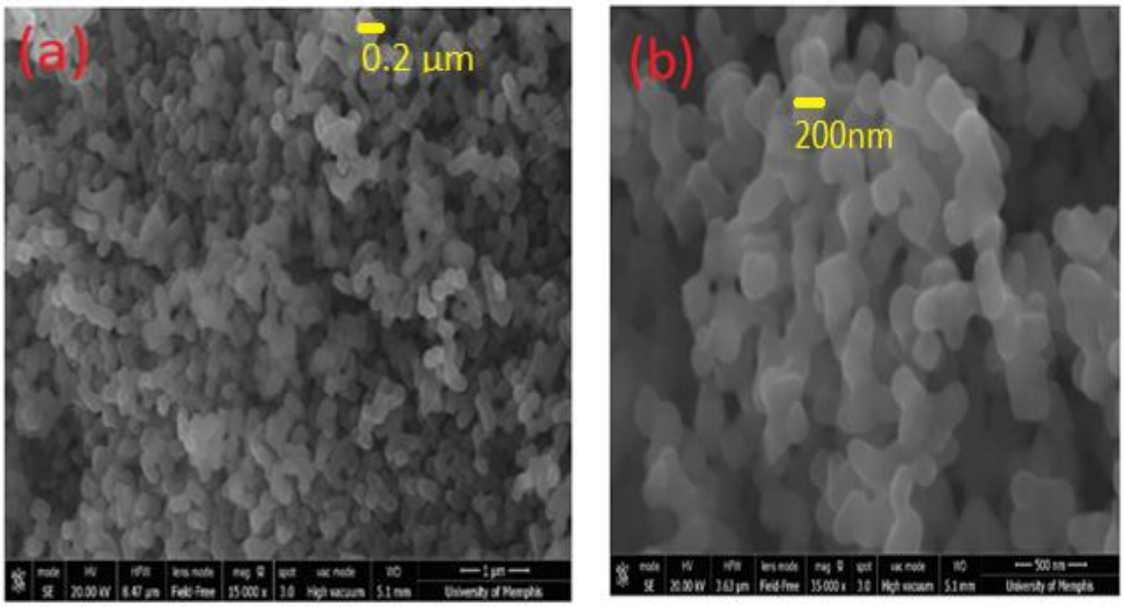

Figure 3.7: SEM images of NiFeP-NCs powder at various magnifications.

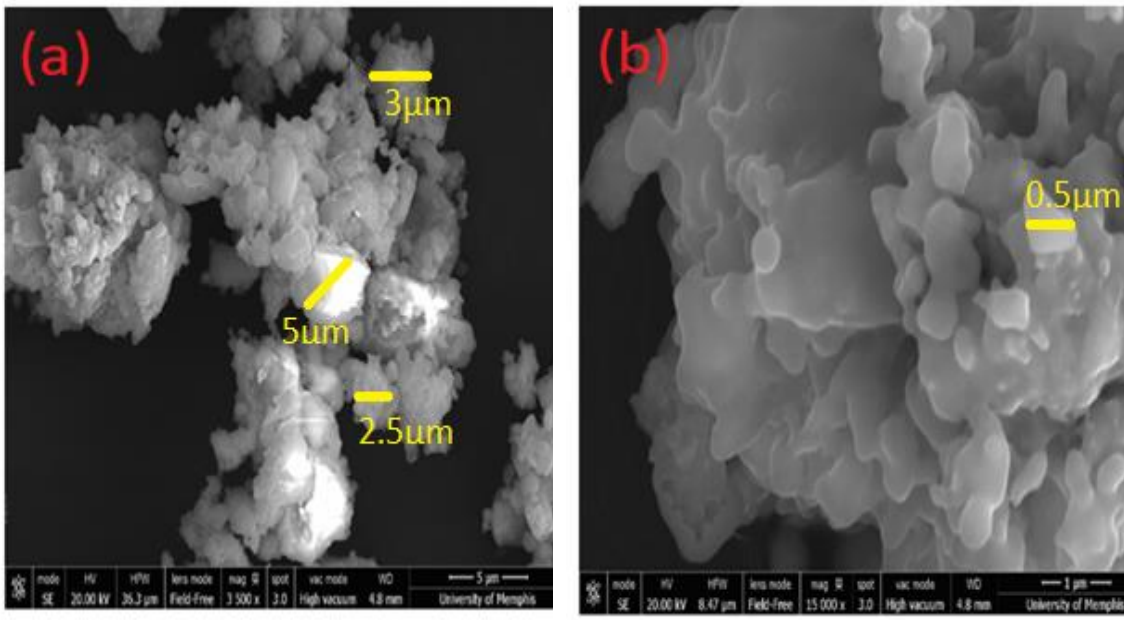

Figure 3.8: SEM images of NiFeP-NPs powder at various magnifications.

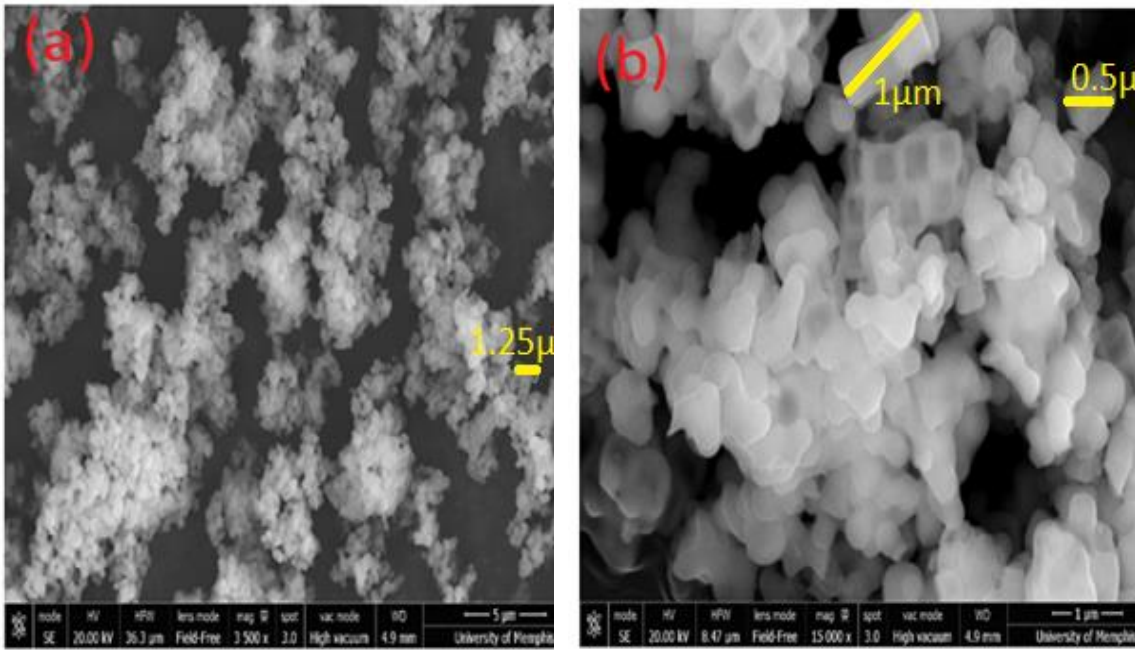

Figure 3.9: SEM images of CoFeP-NCs powder at various magnifications.

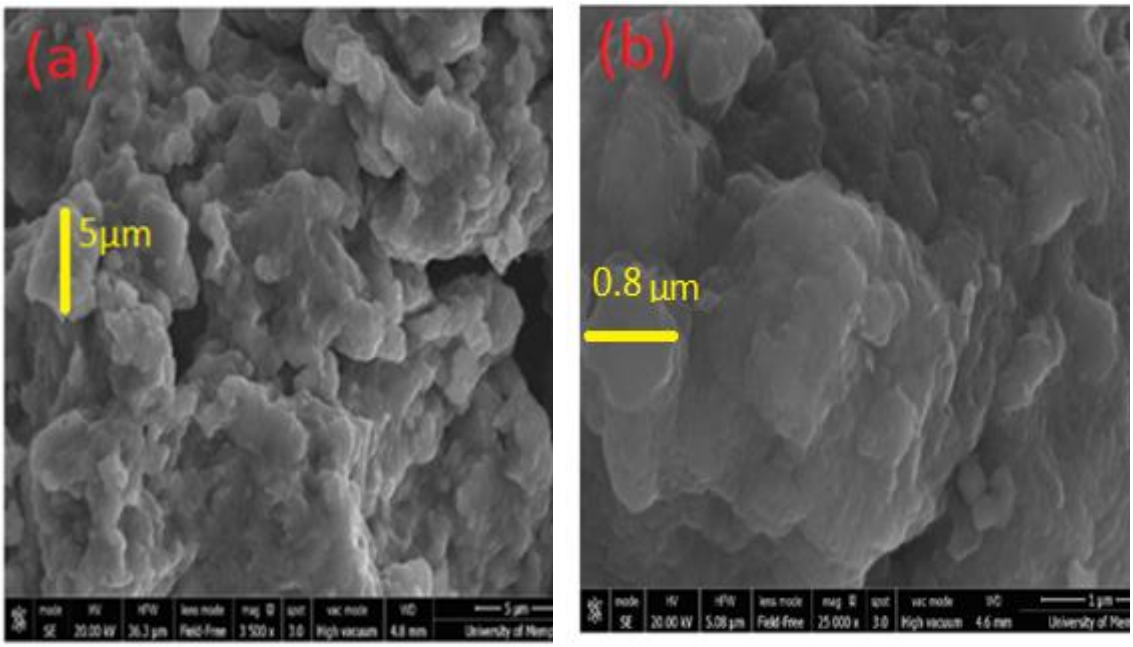

Figure 3.10: SEM images of CoFeP-NPs powder at various magnifications.

The elemental composition, binding energies, and chemical states were performed by using X-ray photoelectron spectroscopy. The XPS spectra patterns confirmed the presence of nickel, iron, oxygen, nitrogen, carbon, potassium, and sodium, which constituted the precursor materials; and sulfur after sulfurization (Figures 3.11a-d). The following full survey XPS spectra figures reveal the elemental composition of NiFe-NCs, NiFe-NPs, NiFeS-NPs, and NiFeS-NPs samples.

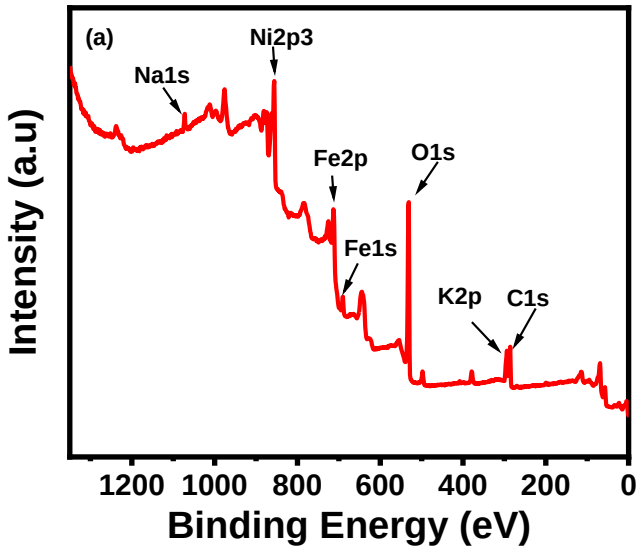

Figure 3.11a: Full survey spectra of NiFe-NCs.

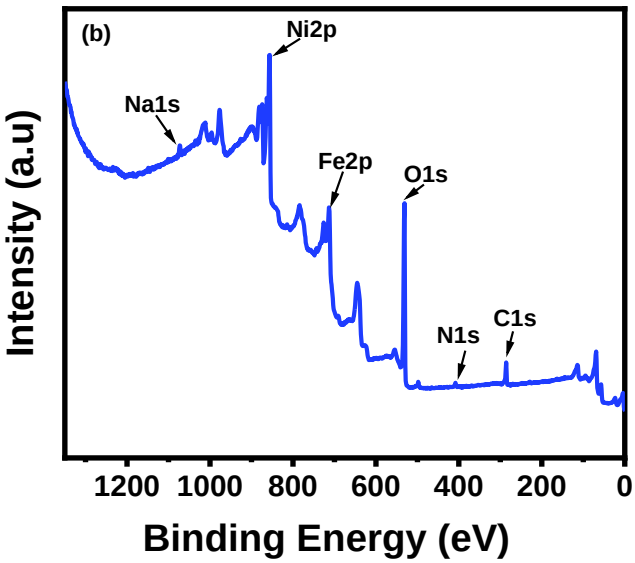

Figure 3.11b: Full survey spectra of NiFe-NPs.

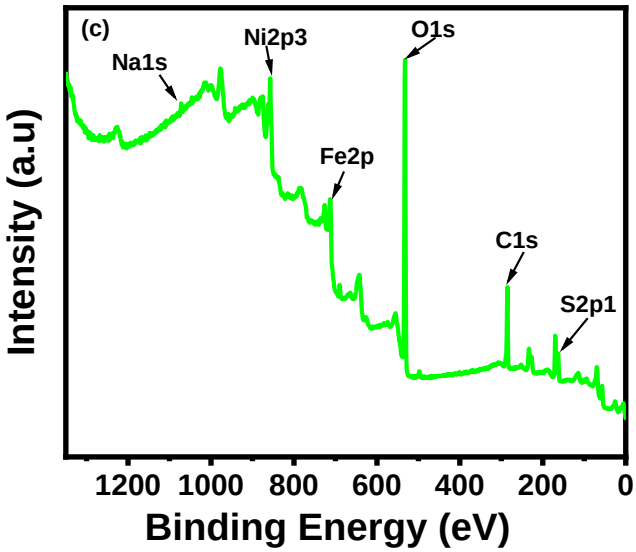

Figure 3.11c: Full survey spectra of NiFeS-NPs.

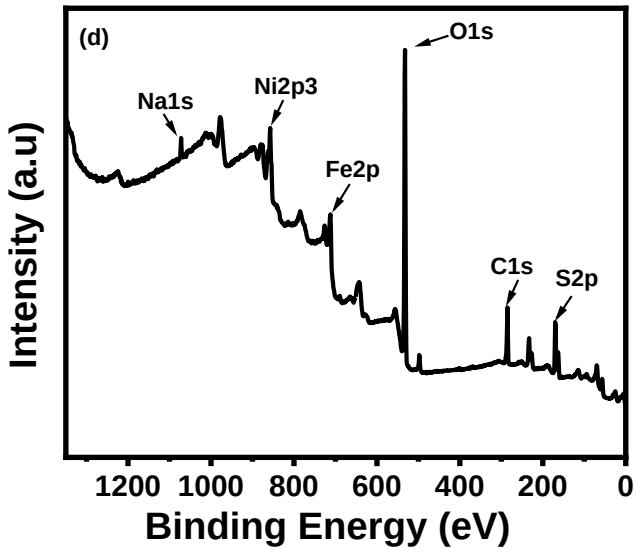

Figure 3.11d: Full survey spectra of NiFeS-NCs.

The XPS analysis was representatively studied using the NiFeS-NPs as it contained most of the elements found in other samples. The high-resolution spectrum for Ni2p

showed the presence of $2p_{1/2}$ and $2p_{3/2}$ peaks of nickel (Figure 3.12a). The XPS spectra of NiFeS hinted the existence of Ni^{3+} $2p_{3/2}$ peak near the 856.8 eV signal, proposing the possibility of chemical bonding of nickel to sulfur and iron atoms [15]. The 862.3 eV signal evidenced a chemical state of Ni^{2+} corresponding to nickel sulfide, with a shift of 0.2 eV, from a typical Ni-S oxidation state [16–18]. The peaks marked at 724.8 and 711.5 eV in Fe2p orbital (Figure 3.12b) are associated with F^{3+} species [19]. Four distinctive peaks were observed from the high-resolution XPS spectrum of O1*s* (Figure 3.12c), at 530.4, 531.5, 532.2, and 533.1 eV respectively. The 530.4 eV peak is affiliated with composites' O^{2-} ions [20]. The 531.5 eV corresponds to oxygen vacancies on the composite surface [21]; and the peaks marked at 532.2 and 533.1 eV are associated with oxygen weak bonds on the materials surface, for example, OH groups bonds [22]. C1s spectra (Figure 3.12d) of NiFeS-NPs show the peaks associated with C-C/C=C, C-O/C-N, C-O/C=O, and O-C=O/O-C having binding energies of 284.9, 285.5, 287.1, and 288.9 eV respectively [23]. Figure 3.12e displays the S2p spectra, the peak spotted at 169.2 eV is associated with the oxidation state of Ni-Fe-S whereas the 161.9 eV binding energy is typical for metal disulfide, proposing the bonding in Ni_2FeS_4 [24, 25] . The 164.1 eV peak authenticated the existence of adsorbed oxygen on the Ni–S surface, and more proof of the existence of surface oxygen was revealed from the sulfoxide signal marked at 165.5 eV [24–26]. The binding energies and chemical states of materials were evaluated by high-resolution XPS spectra as displayed in Figures 3.12a-e.

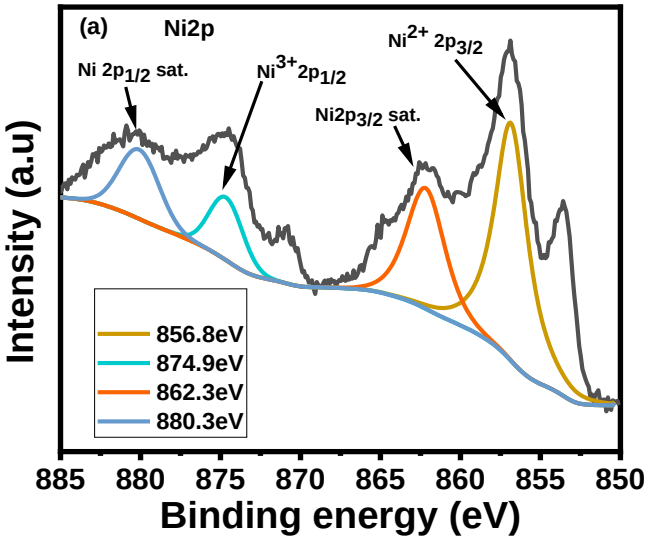

Figure 3.12a: High resolution XPS spectra of Ni2p.

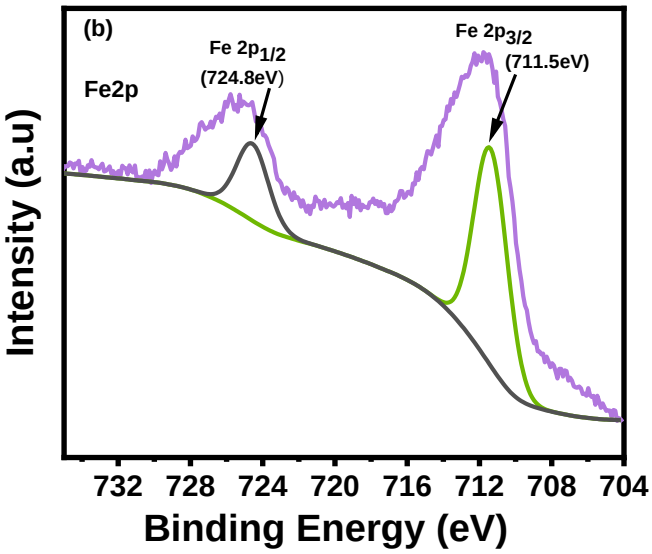

Figure 3.12b: High resolution XPS spectra of Fe2p.

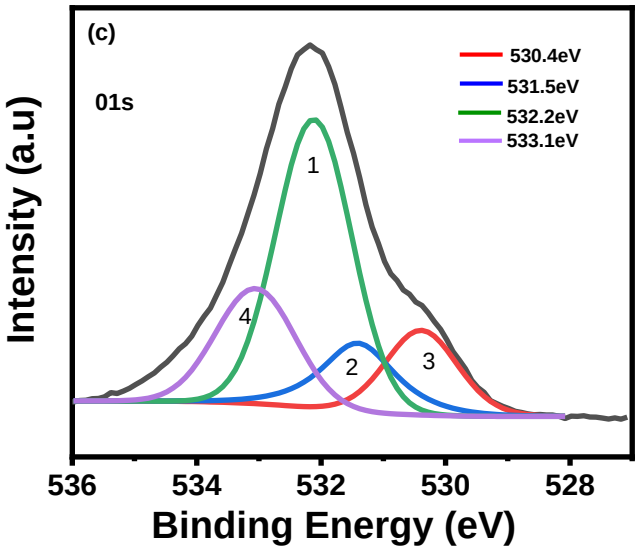

Figure 3.12c: High resolution XPS spectra of O1s.

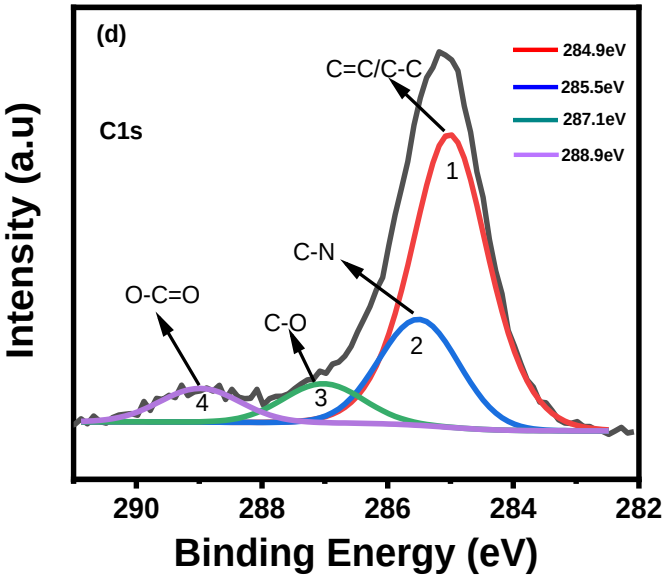

Figure 3.12d: High resolution XPS spectra of C1s.

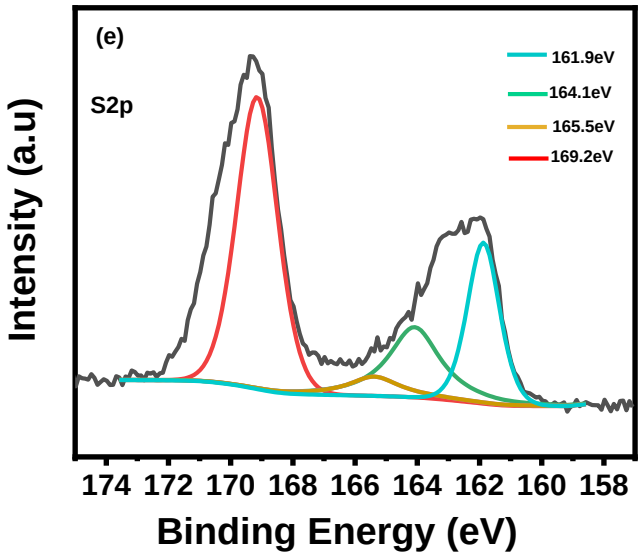

Figure 3.12e: High resolution XPS spectra of S2p.

3.1.2 X-ray diffraction analysis

The materials structures were studied and demonstrated by XRD patterns. The diffracted patterns of the samples were recorded in a range of 25-70 degrees as shown in Figure 3.13.

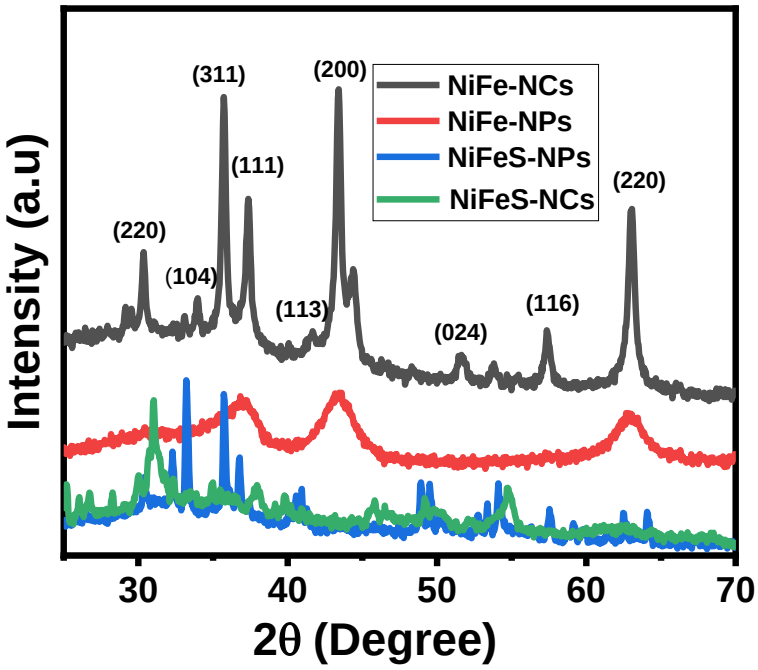

Figure 3.13: XRD patterns of NiFe-NCs, NiFe-NPs, NiFeS-NPs, and NiFeS-NCs.

Powder X-ray diffraction confirmed that NiFe-NCs and NiFe-NPs samples are phase pure. Their diffraction lines can be assigned to the spinel of NiFe-NCs and NiFe-NPs respectively (JCPDS:47-1049, JCPDS:39-1346, and JCPDS:24-0072). On the other hand, the patterns for NiFeS-NPs and NiFeS-NCs suggested the existence of impurity/amorphous structures in the samples due to no obvious feature peaks.

3.2 Electrochemical characterizations

The electrochemical measurements of the samples were carried out to assess the oxygen evolution reaction and hydrogen evolution reaction overpotentials as well as the supercapacitance properties of the materials.

3.2.1 Oxygen evolution reaction

An oxygen evolution reaction is a limiting reaction in the process of generating molecular oxygen through chemical reactions, such as the oxidation of water during oxygenic photosynthesis, electrolysis of water into oxygen and hydrogen, and electrocatalytic oxygen evolution from oxides and oxoacids. The catalysts performance was investigated in 1M KOH solution in a typical three-electrode set up as shown in Figure 2.5. The OER activities of samples were compared. Figure 3.14a demonstrates linear sweep voltammetry (LSV) polarization curves at 2 mV/s scan rate and their respective overpotentials to deliver a current density of 10 mA/cm^2. The polarization curves reported in figures are the second sweeps; the first sweeps normally suffer from residual and capacitance currents. The sweeps were corrected against the cell potential drop (IR compensation). The polarization curves for 1 and 1000 cycles were very close (Figures 3.15a-d), implying the good electrochemical stability of the materials. The OER results for NiFe-NCs, NiFe-NPs, NiFeS-NCs, and NiFeS-NPs are shown in the following figures.

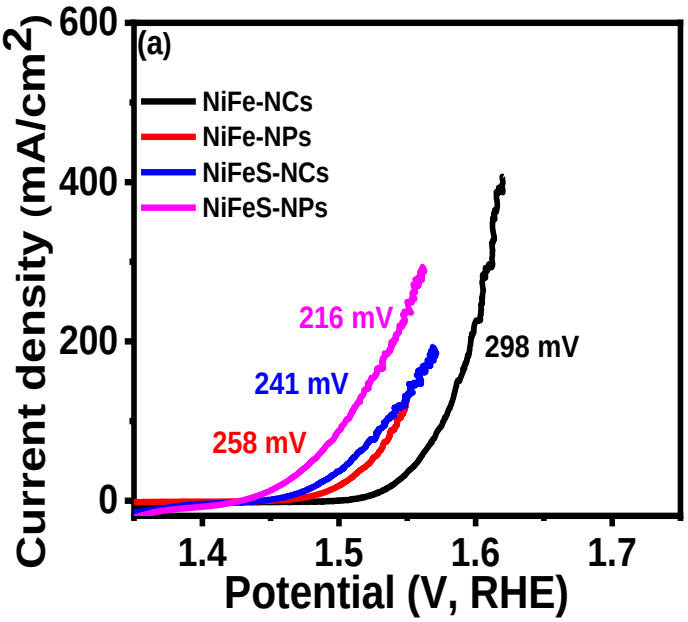

Figure 3.14a: LSV curves of NiFe samples.

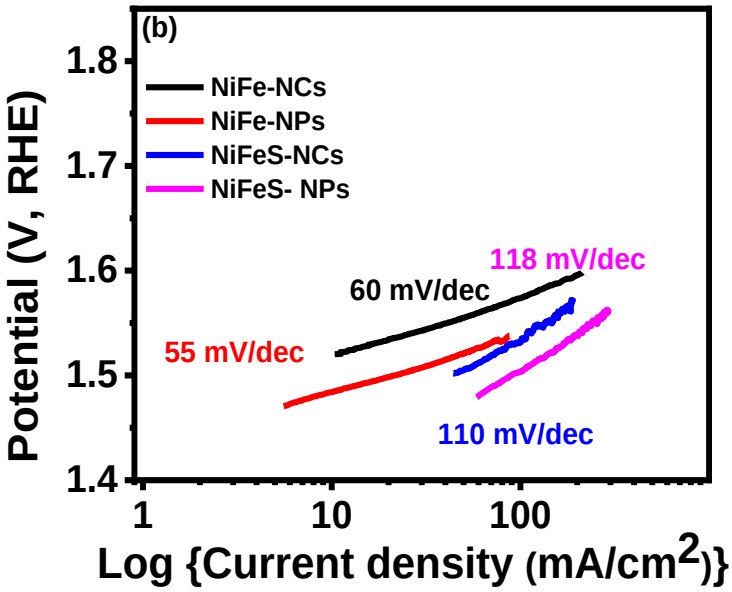

Figure 3.14b: Tafel plots of NiFe samples.

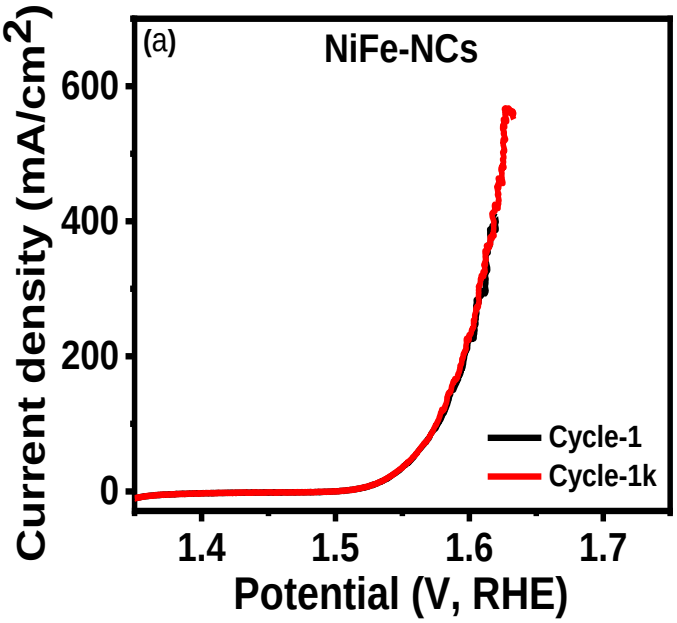

Figure 3.15a: LSV curves of NiFe-NCs at 1 and 1000 cycles.

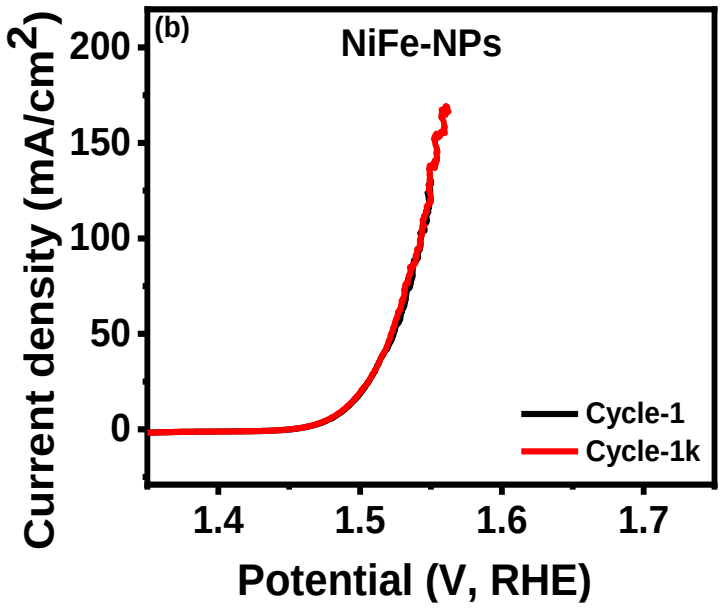

Figure 3.15b: LSV curves of NiFe-NPs at 1 and 1000 cycles.

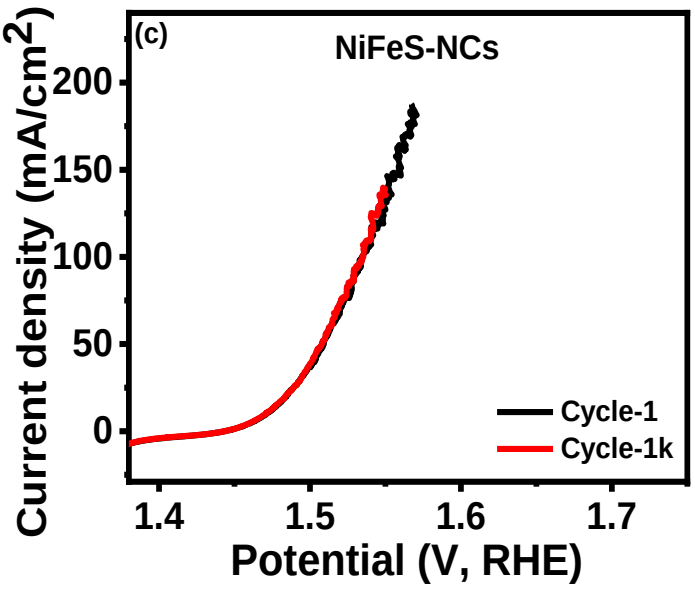

Figure 3.15c: LSV curves of NiFeS-NCs at 1 and 1000 cycles.

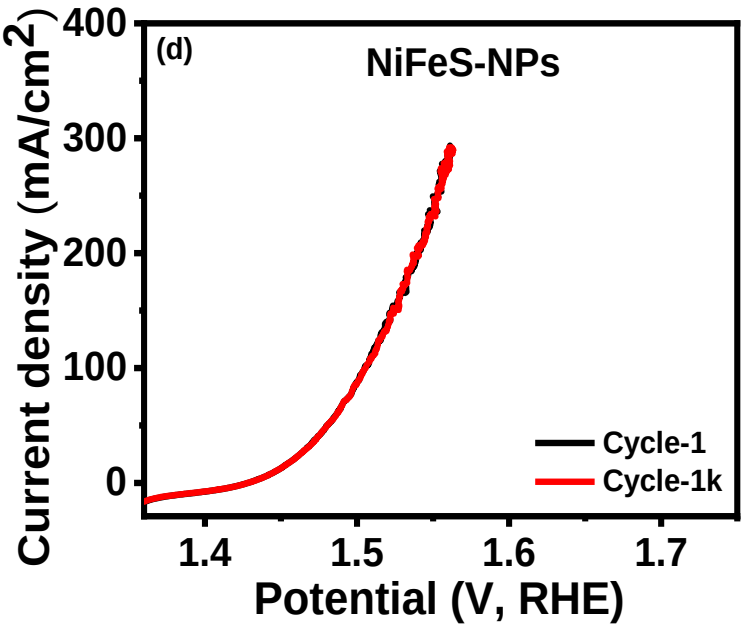

Figure 3.15d: LSV curves of NiFeS-NPs at 1 and 1000 cycles.

The electrochemical impedance spectroscopy (EIS), Figures 3.16a-d, showed a decrease in internal resistance after sulfurization. This is also reflected in the decrease of overpotentials after sulfurization (Figure 3.14a).

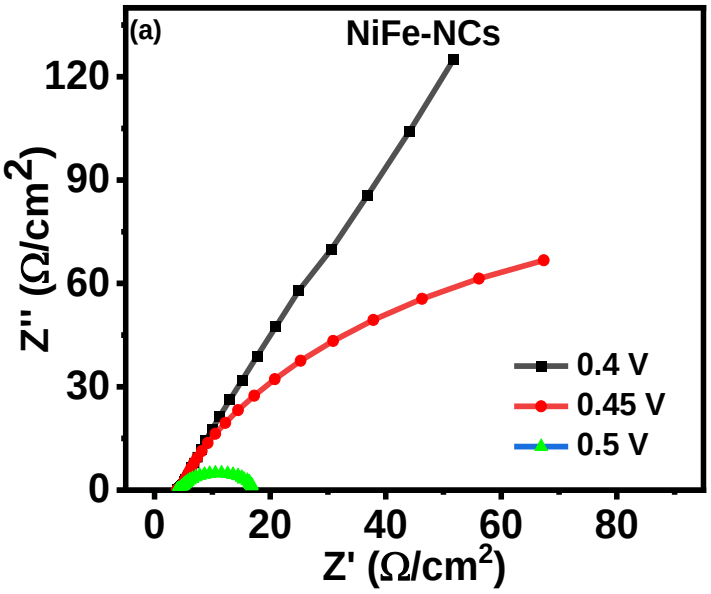

Figure 3.16a: Zim versus Zre of NiFe-NCs at different potentials.

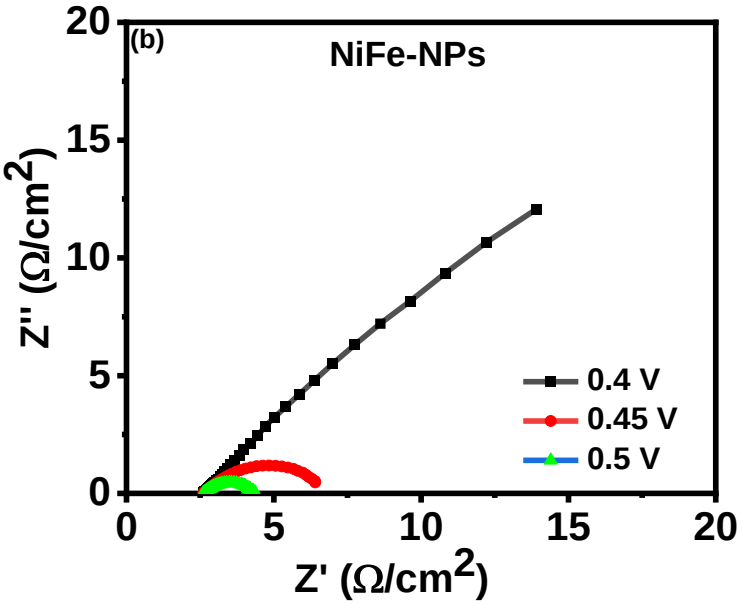

Figure 3.16b: Zim versus Zre of NiFe-NPs at different potentials.

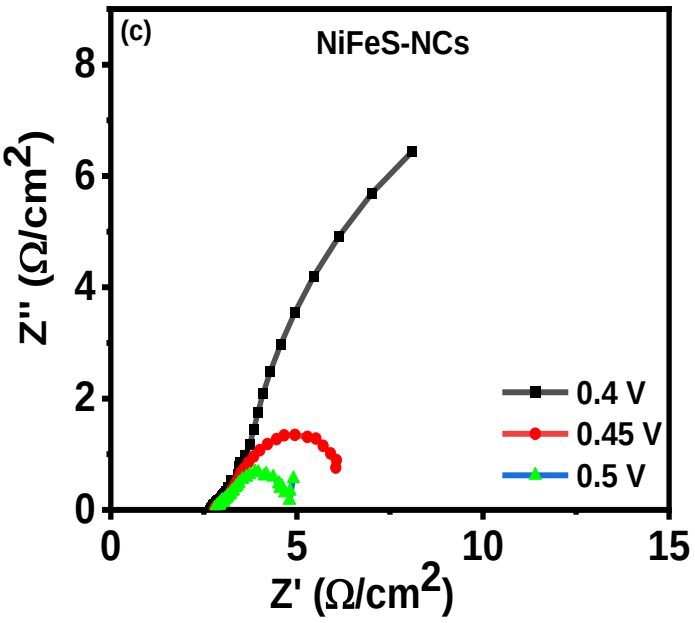

Figure 3.16c: Zim versus Zre of NiFeS-NCs at different potentials.

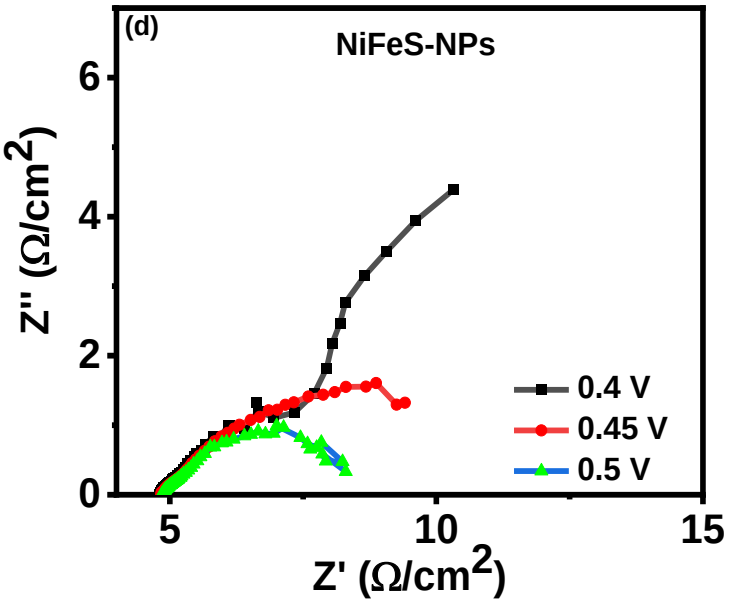

Figure 3.16d: Zim versus Zre of NiFeS-NPs at different potentials.

In general, all four of the NiFe samples demonstrated impressive small overpotentials for OER; sulfurized NiFe nanoparticles outperformed the rest of the samples with the smallest onset overpotential of 216 mV from 258 mV to attain a current density of 10 mA/cm^2. Similarly, the overpotential for NiFeS-NCs improved from 298 mV to 241 mV. The reason for the impressive catalytic effect of NiFe-NPs is their large surface area (high surface area to volume ratio), which enhances electrons mobility. In either case, the exposed edges and vertices of NiFe-NCs provide active sites that speed the electrocatalytic process. Both NCs and NPs show improved overpotentials after sulfurization. It suggests that the mobility interference imposed by sulfur atoms was lower than its electrical conductivity effect in the host materials, and therefore the improvement of electrical conductivity of materials by sulfur donated electrons [27]. The Nyquist plots show the decrease in impedance after sulfurization (Figures 3.17a-d below).

The formation rate of oxygen is figured out by Tafel slopes. The Tafel slopes were calculated (Figure 3.15b), where NiFe-NPs showed the smallest slope (55 mV/dec). The lower Tafel slope implies a high electrical current growth rate and fast chemical reaction. The Tafel slopes were obtained by LSV polarization curves using the Tafel equation [28].

$\eta = b\log(j)+a$ ..... (6)

where η is the overpotential, j is the current density and b is the Tafel slope.

3.2.1.1 Durability test

To ascertain how durable the samples could be, chronoamperometric (CA) testing was conducted for 20 hours. The overall performance showed all samples have good stability (Figures 3.17a-d), at a potential of 550 mV; sulfurized samples were more stable as shown in the following figures.

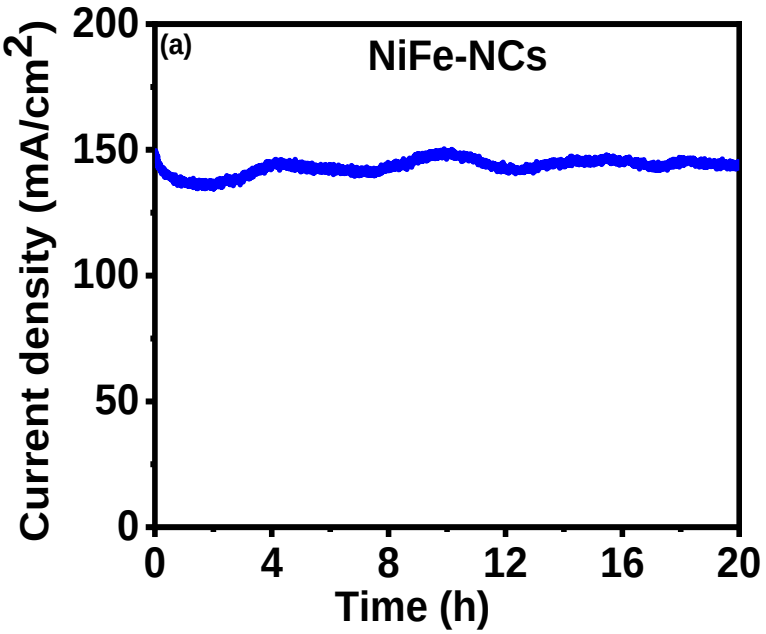

Figure 3.17a: CA plot of NiFe-NCs for 20 hours.

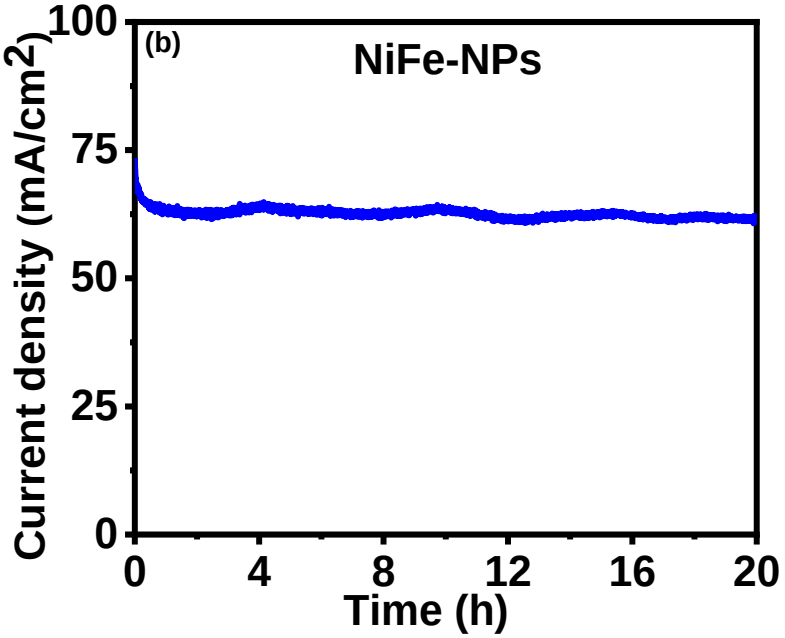

Figure 3.17b: CA plot of NiFe-NPs for 20 hours.

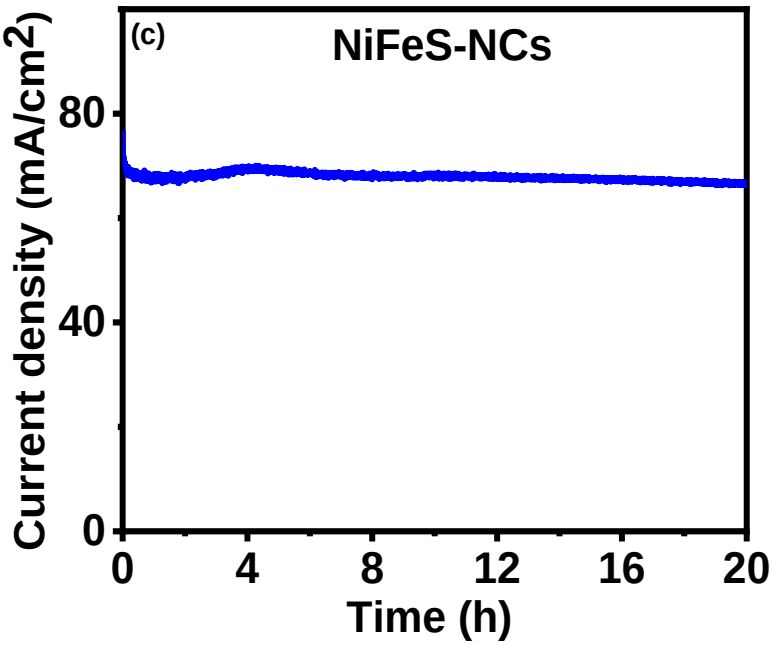

Figure 3.17c: CA plot of NiFeS-NCs for 20 hours.

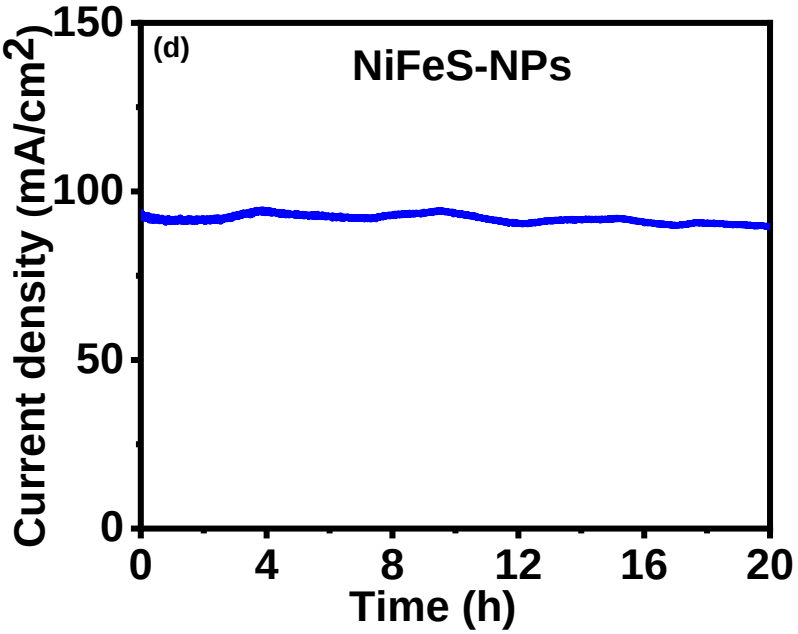

Figure 3.17d: CA plot of NiFeS-NPs for 20 hours.

3.2.2 Hydrogen evolution reaction

The hydrogen evolution reaction of NiFe samples was also studied. The electrocatalytic performance was examined at the scanning rate of 2 mV/s in 1M KOH. The HER linear sweep voltammetry polarization curves with their overpotentials are shown in Figure 3.18a, NiFe-NCs indicating the lowest overpotential of 54 mV in delivering a current density of 10 mA/cm^2. The Tafel slopes (Figure 3.18b) were roughly the same for NiFe-NCs, NiFe-NPs, NiFeS-NCs, and NiFeS-NPs samples (116, 122, 114, and 116 mV/dec, respectively). A lower overpotential of 54 mV to reach a current of 10 mA/cm^2 by the NiFe-NCs is the implication of their lower resistance to charge flow and possession of favorite kinetics for HER as a result of their unique exposed active sites [29]. The LSV

polarization curves of samples at 1 and 1000 cycles were very close, indicating the materials' stability (Figures 3.19a-d). The HER results are as shown in the following figures.

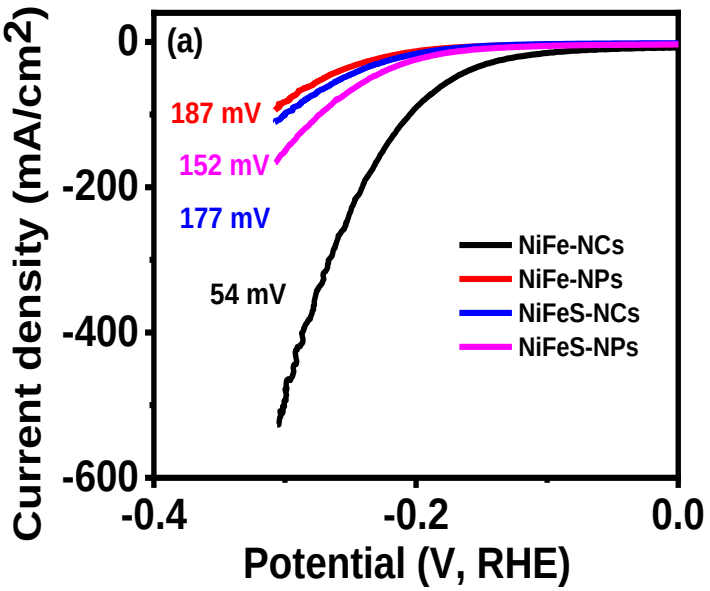

Figure 3.18a: LSV curves of NiFe samples.

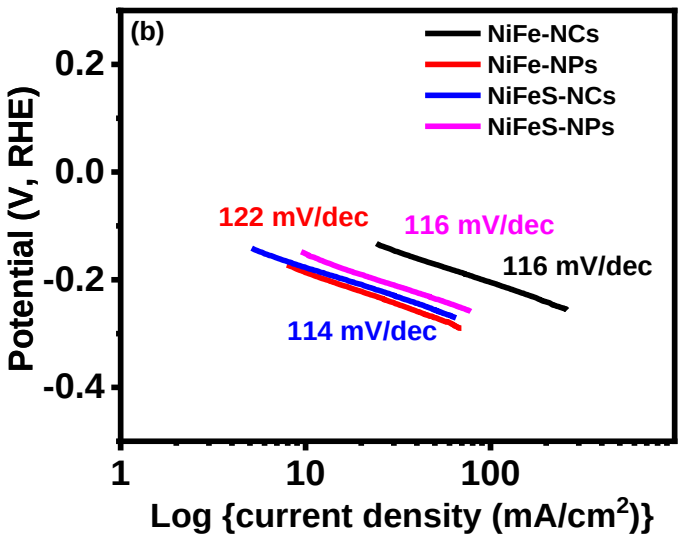

Figure 3.18b: Tafel plots of NiFe samples.

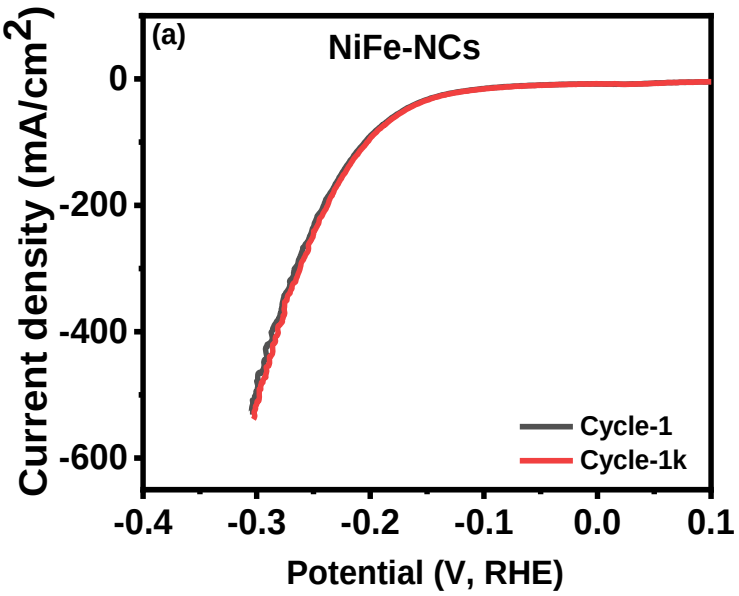

Figure 3.19a: LSV curves of NiFe-NCs at 1 and 1000 cycles.

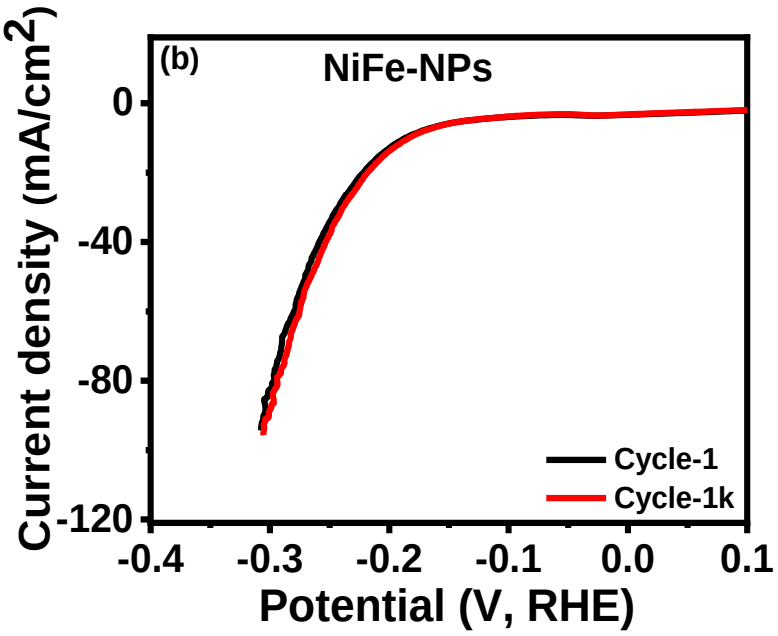

Figure 3.19b: LSV curves of NiFe-NPs at 1 and 1000 cycles.

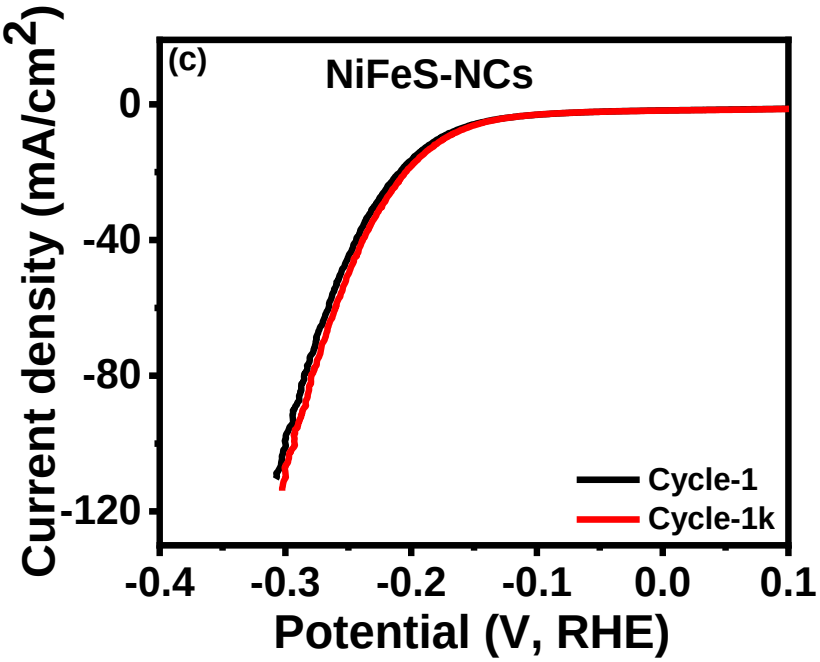

Figure 3.19c: LSV curves of NiFeS-NCs at 1 and 1000 cycles.

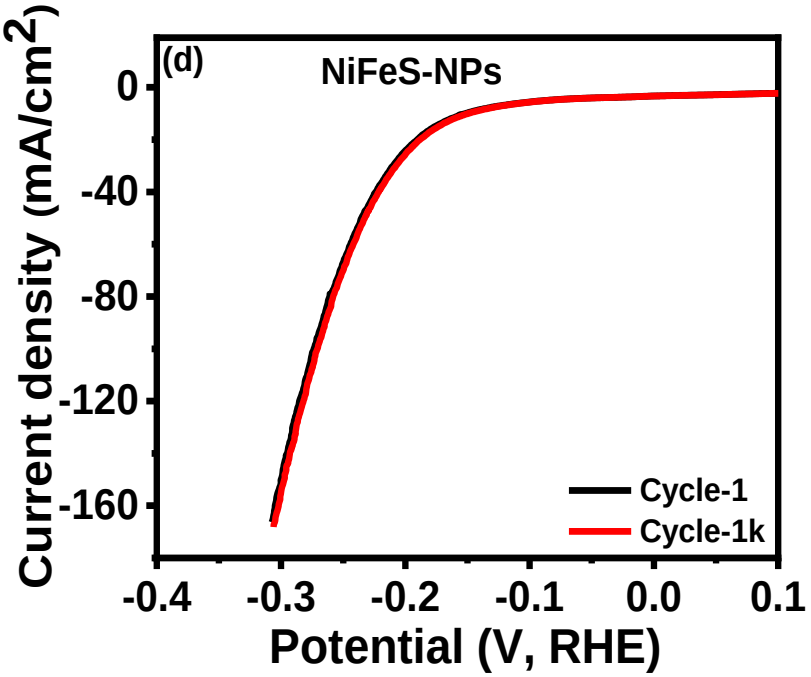

Figure 3.19d: LSV curves of NiFeS-NPs at 1 and 1000 cycles.

3.2.3 Supercapacitance

3.2.3.1 Cyclic voltammetry and galvanostatic charge-discharge characteristics

Cyclic voltammetry and galvanostatic charge-discharge measurements were carried out at 3M KOH by applying a potential window of 0 to 0.6 V to study the charge storage/capacitance of the synthesized materials. Generally, the results showed improved capacitances of the materials after sulfurization. At various scan rates, cyclic voltammograms showed perfect reversible trends, implying that the materials are electrochemically stable. Higher scan rates showed higher current densities and vice versa. High scan rates do not provide sufficient time for deposition layer formation over the electrode surface, which would increase resistance. The cyclic voltammetry curves of the samples (Figures 3.20a, c, e, and g), seemed to have identical reversible shapes, implying good stability and perfect reversible reaction kinetics (oxidation-reduction) of the materials. Galvanostatic charge-discharge curves of the samples (Figures 3.20b, d, f, and h), were obtained at 1−20 A/g. Their nearly isosceles triangular shapes suggest good capacitive traits [30]. The results for cyclic voltammograms and charge-discharge characteristics are shown in the following diagrams.

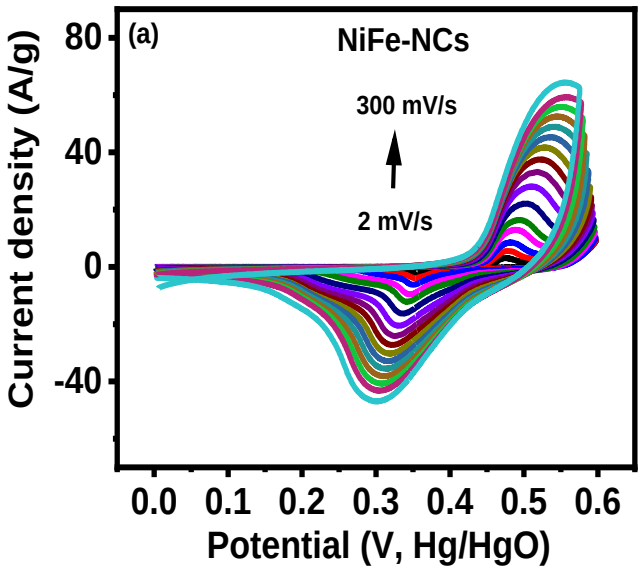

Figure 3.20a: Cyclic voltammograms of NiFe-NCs at various scan rates.

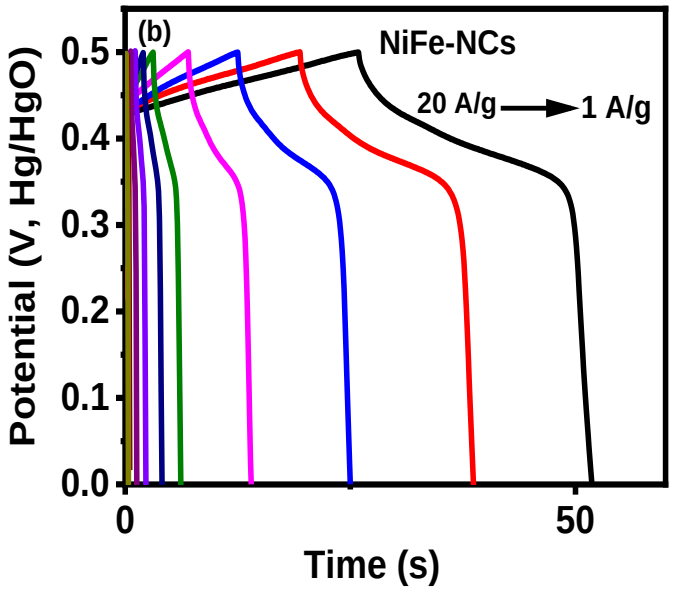

Figure 3.20b: Charge-discharge characteristics of NiFe-NCs at various currents.

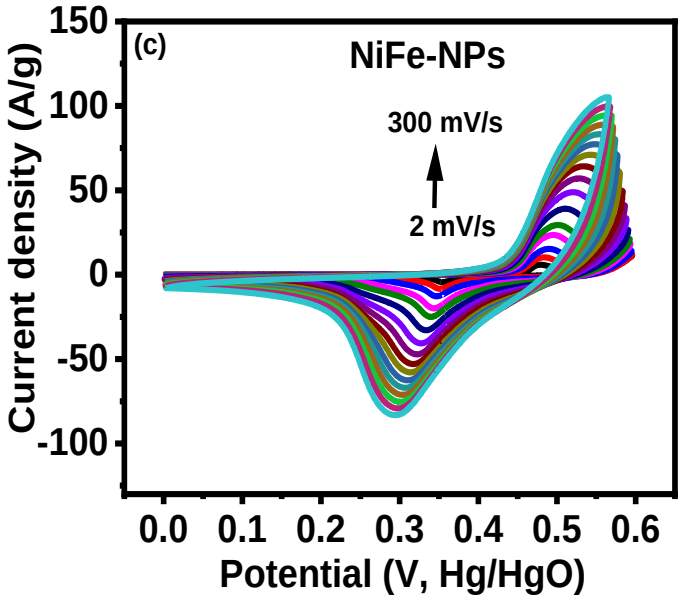

Figure 3.20c: Cyclic voltammograms of NiFe-NPs at various scan rates.

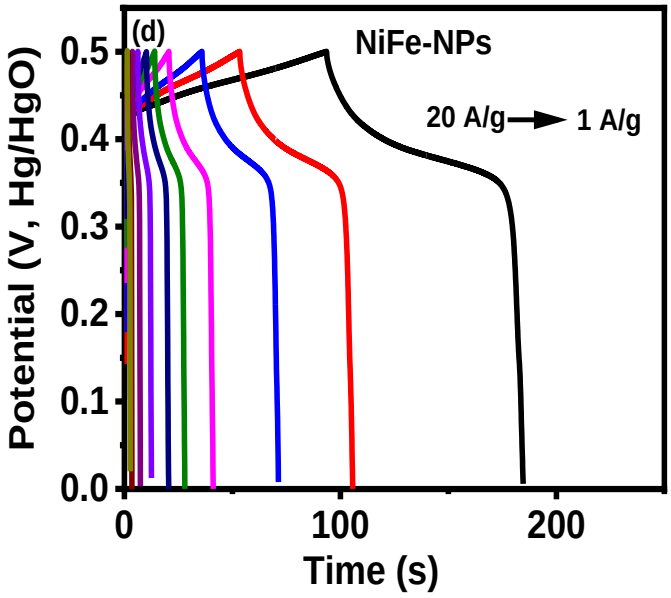

Figure 3.20d: Charge-discharge characteristics of NiFe-NPs at various currents.

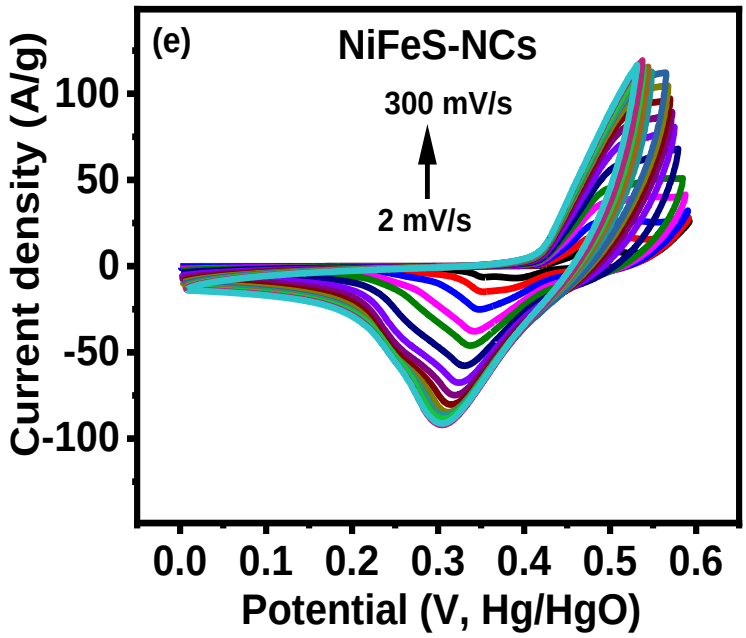

Figure 3.20e: Cyclic voltammograms of NiFeS-NCs at various scan rates.

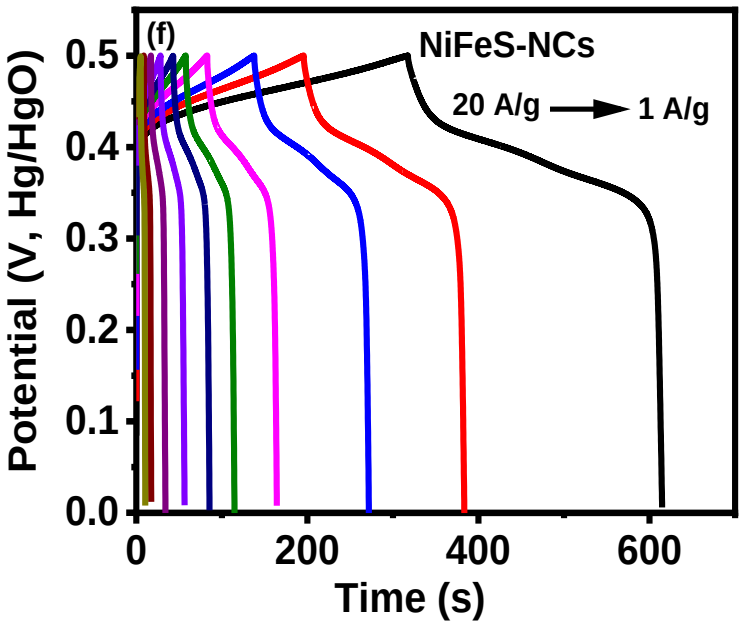

Figure 3.20f: Charge-discharge characteristics of NiFeS-NCs at various currents.

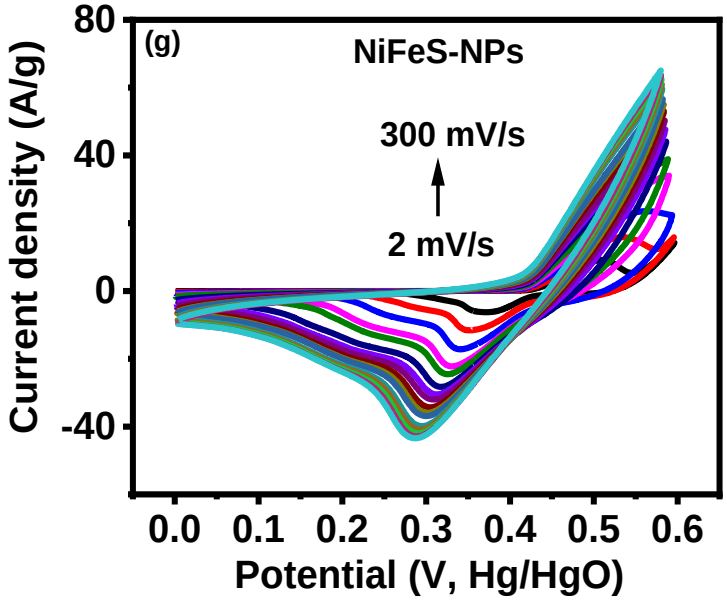

Figure 3.20g: Cyclic voltammograms of NiFeS-NPs at various scan rates.

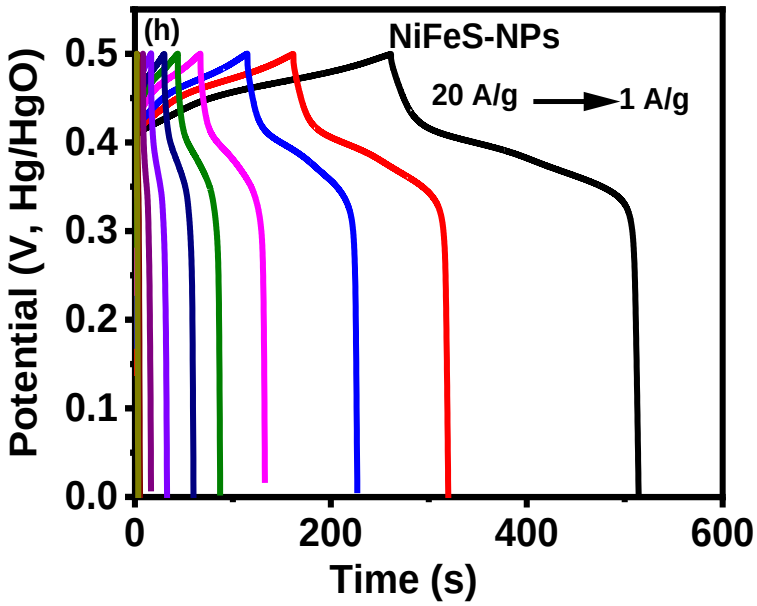

Figure 3.20h: Charge-discharge characteristics of NiFeS-NPs at various currents.

3.2.3.2 Specific capacitance

Data from the charge-discharge measurements were used to calculate the specific capacitance of the as-prepared electrodes. The specific capacitance (*Csp*) of the electrodes was calculated using the following expression [11].

$$C_{sp} = \frac{I\Delta t}{\Delta V m} \quad \text{.....(7)}$$

where *I* is the current (A), Δt is the discharge time (s), ΔV is the potential window (V) and *m* is the active mass of the material on the electrode.

The variation of specific capacitance as a function of current density for the NiFe samples is shown in Figure 3.21. With increasing current, the specific capacitance decreased in all the studied electrodes. This could be due to the lack of time for the redox reactions at electrodes and a significant potential drop at higher current discharges [31]. On the other hand, sulfurization of the samples showed an increment of specific capacitance. The specific capacitance of NiFe-NCs and NiFe-NPs increased from 69 to 605 F/g and from 186 to 515 F/g, an increment of about 9 times and 3 times respectively at a current density of 1 A/g (Table 3.1).

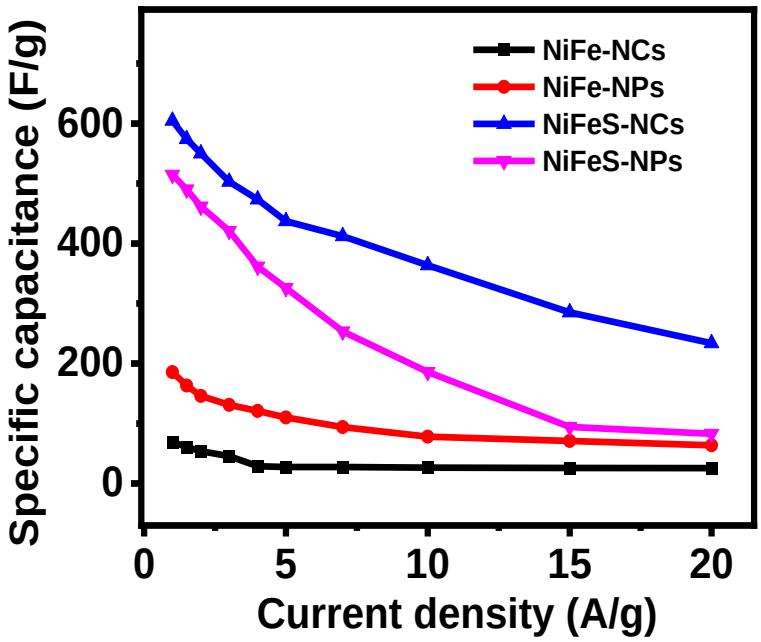

Figure 3.21: Variation of specific capacitance with current density.

Table 3.1: Comparison of specific capacitance of NiFe samples at 1 A/g before and after sulfurization.

Sample name	Specific capacitance (F/g)	Increment factor
NiFe-NCs	69	9
NiFeS-NCs	605	
NiFe-NPs	186	3
NiFeS-NPs	515	

3.2.3.3 Power density and energy density

To assess the supercapacitance performance, the energy and power density of materials were calculated. The equations given below were used to calculate the energy and power densities of the materials [32].

$$E\left(\frac{Wh}{Kg}\right) = \frac{Csp \times \Delta V^2}{7.2} \quad \text{..} (8)$$

$$P\left(\frac{W}{Kg}\right) = \frac{E \times 3600}{t} \quad \text{..} (9)$$

where *Csp* is the specific capacitance (F/g), Δ*V* is the potential window (V), and t is the discharge time (s).

The power and energy density of NiFe samples were studied in 3M KOH electrolyte and their relationship is shown in Figure 4.1a (Ragone plot). As seen from the figure, the power density and energy density are inversely related. Lower discharge currents corresponded to higher energy density while higher power density was observed at higher current discharge. The energy density of sulfurized samples was greatly improved, from 2 to 20 Wh/kg for NiFe-NCs and NiFeS-NCs, and from 6 to 17 Wh/kg for NiFe-NPs and NiFeS-NPs respectively, at 1 A/g.

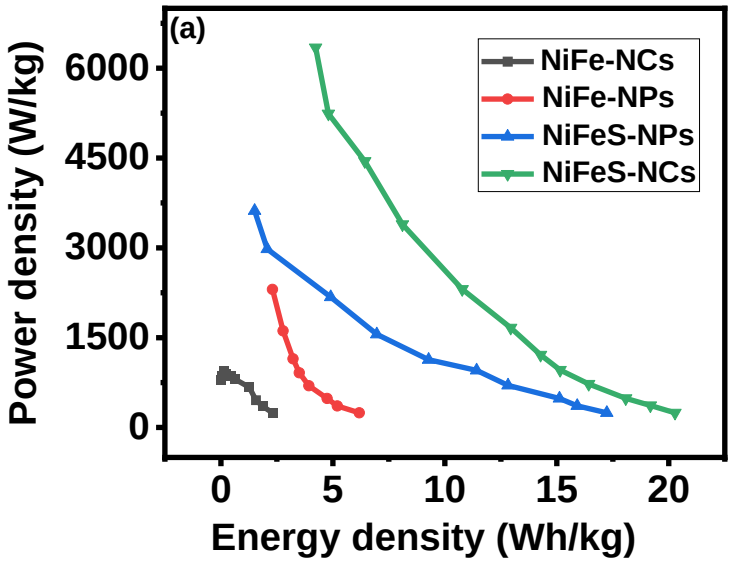

Figure 3.22a: Ragone plot of NiFe samples.

Table 3.2: Comparison of energy densities of NiFe samples at 1 A/g before and after sulfurization.

Sample name	Energy density (Wh/kg)	Increment factor
NiFe-NCs	2	10
NiFeS-NCs	20	
NiFe-NPs	6	3
NiFeS-NPs	17	

The electrochemical impedance spectroscopy was carried out to study the internal resistance of the synthesized samples; the sulfurized samples seemed to have lower resistance. This is evidenced from the Nyquist plot (Figure 3.22b) where the impedance of the sulfurized materials is decreased. Reduced resistance can also be interpreted from

porous SEM images of sulfurized samples, where the electrons' mobility would have been facilitated (Figure 3.1 and Figure 3.2), where the sulfurized samples have more compatibility with materials as compared to NiFe-NPs which seemed to have empty spaces between the particles.

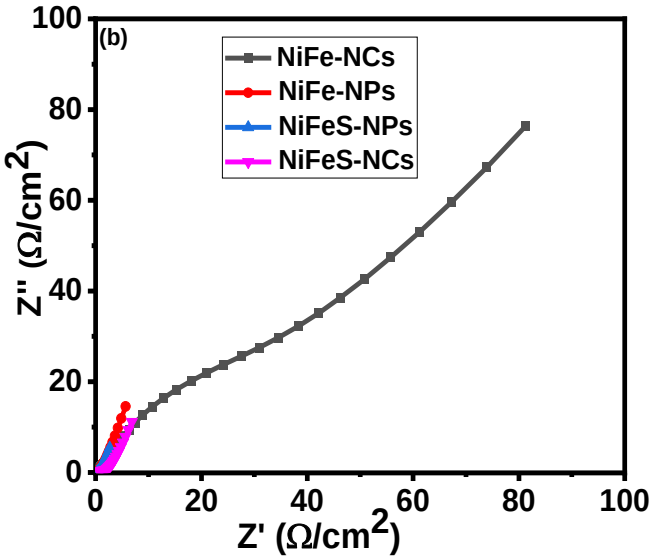

Figure 3.22b: Zim versus Zre showing reduced impendence after sulfurization.

Electrochemical measurements for CoFe samples were also carried out and showed great improvement in some parameters. The samples showed nearly the same overpotentials of ≈300 mV for oxygen evolution reactions (Figure 3.23a). Introducing sulfur to the CoFe-NCs and CoFe-NPs did not significantly change their OER overpotentials, as is evidenced from EIS plots, where their internal resistances remained fairly the same before and after sulfurization (Figures 3.26a-d). The OER results for CoFe samples are shown in the following figures.

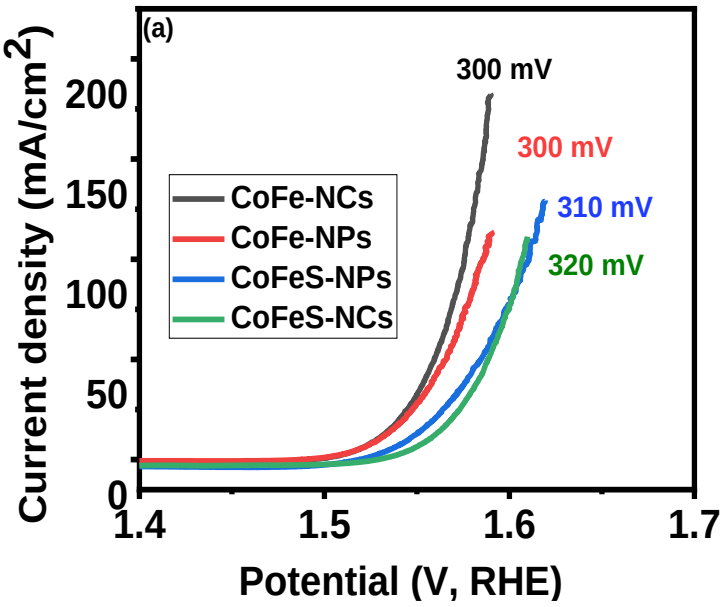

Figure 3.23a: LSV curves of CoFe samples.

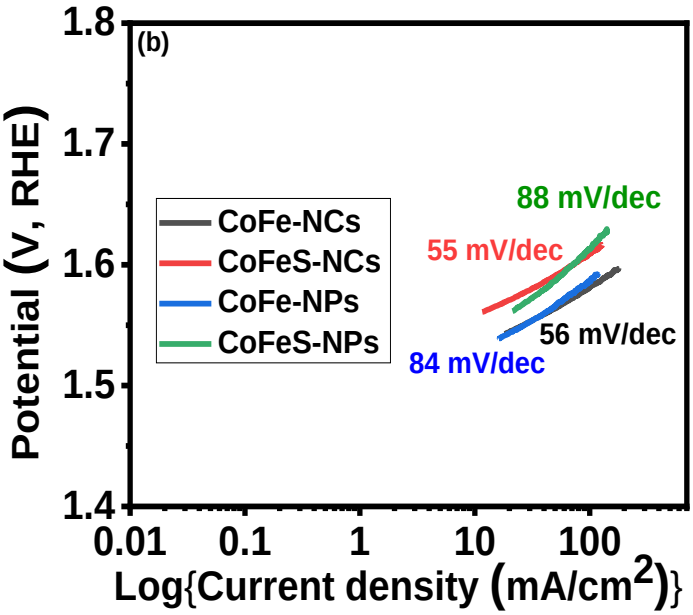

Figure 3.23b: Tafel plots of CoFe samples.

The OER linear sweep voltammetry polarization curves of the samples showed good stability at 1 and 1000 cycles. CoFe-NCs showed high stability after sulfurization (Figure 3.24c). The LSV polarization curves are shown in the following figures.

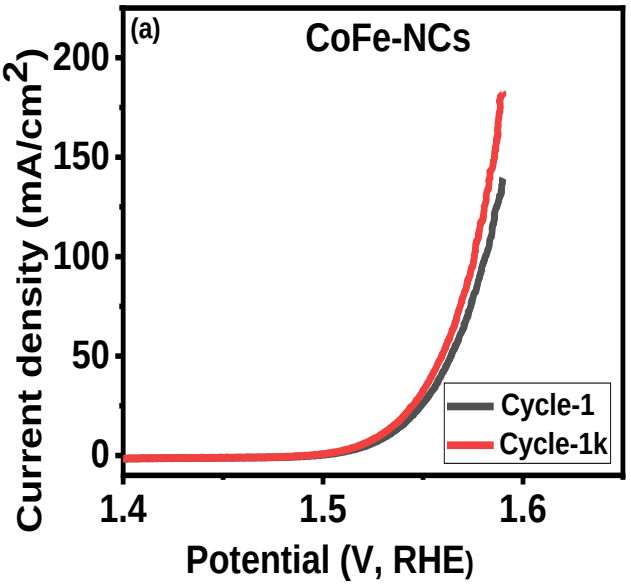

Figure 3.24a: LSV curves of CoFe-NCs at 1 and 1000 cycles**.**

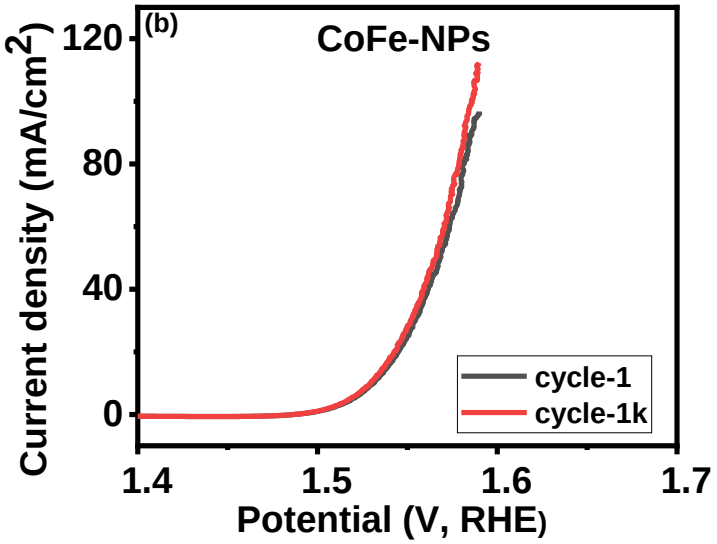

Figure 3.24b: LSV curves of CoFe-NPs at 1 and 1000 cycles.

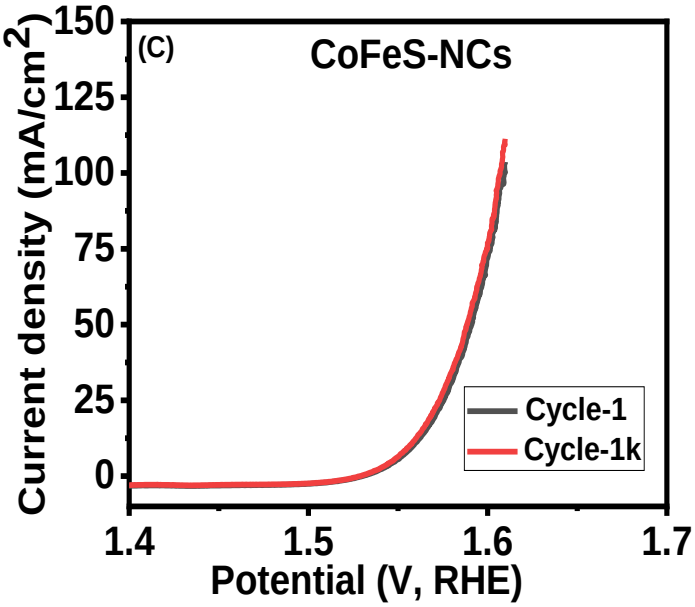

Figure 3.24c: LSV curves of CoFeS-NCs at 1 and 1000 cycles.

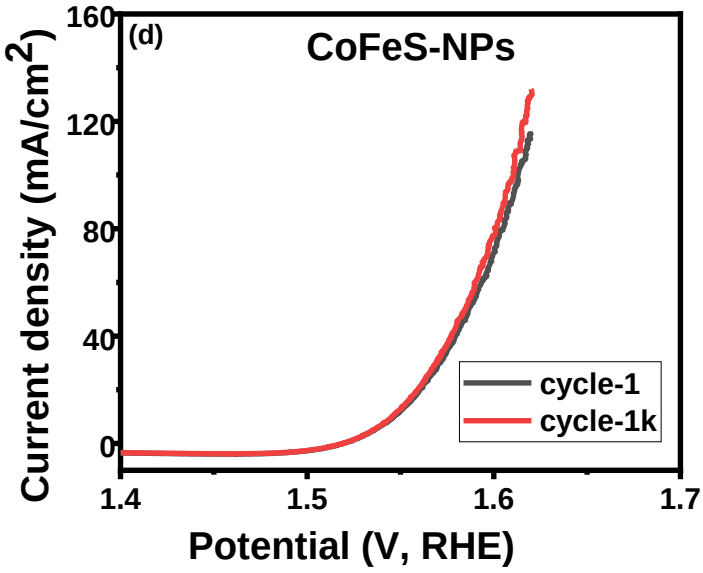

Figure 3.24d: LSV curves of CoFeS-NPs at 1 and 1000 cycles**.**

The durability test was performed at 550 mV for 20 hours, and materials showed a fairly steady current flow as shown from the following figures.

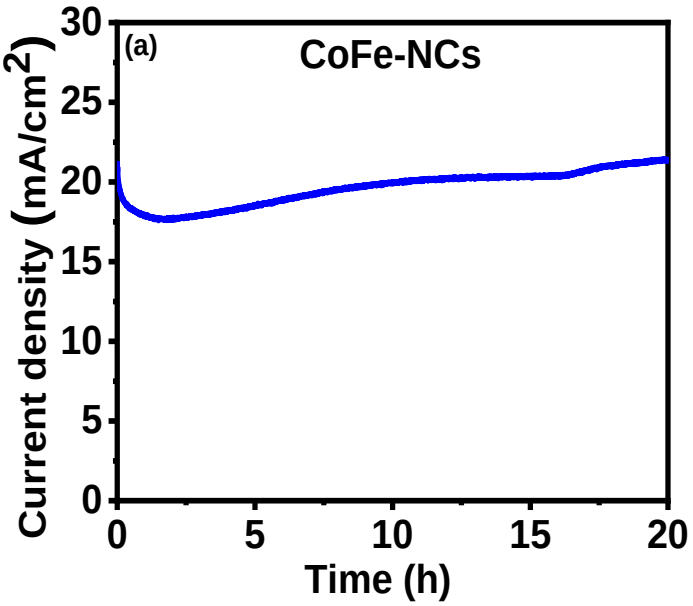

Figure 3.25a: CA plot of CoFe-NCs for 20 hours.

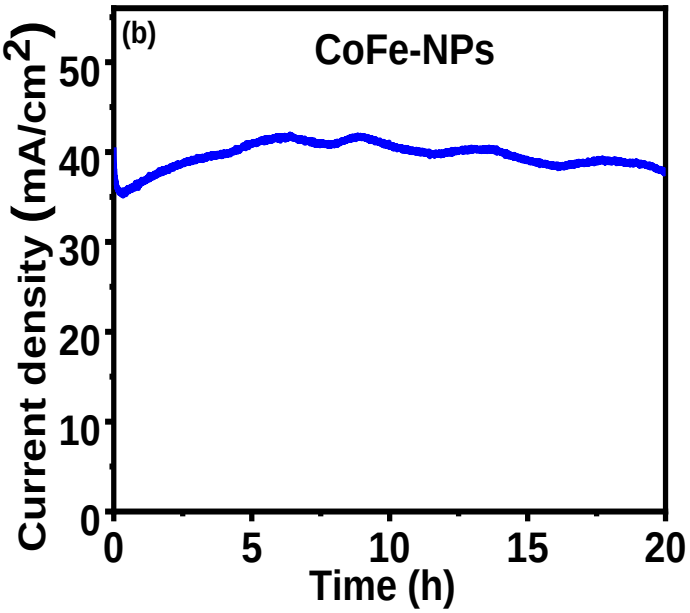

Figure 3.25b: CA plot of CoFe-NPs for 20 hours.

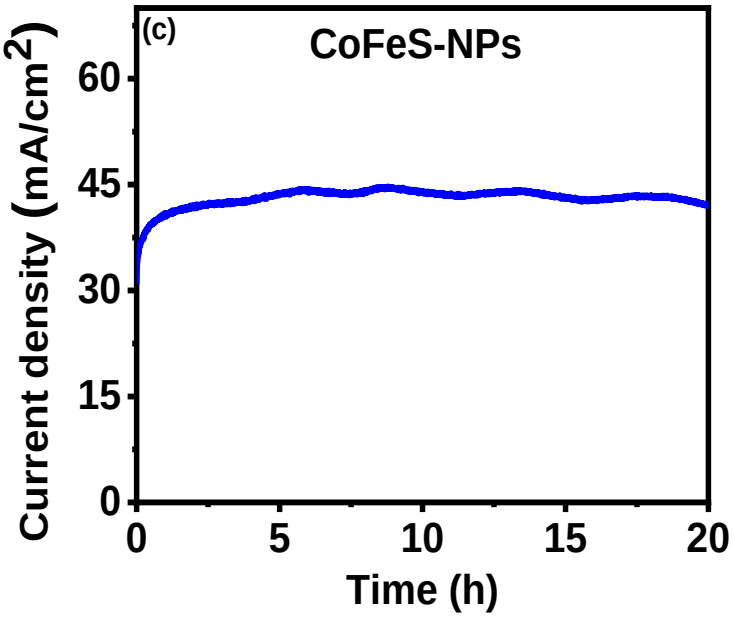

Figure 3.25c: CA plot of CoFeS-NPs for 20 hours.

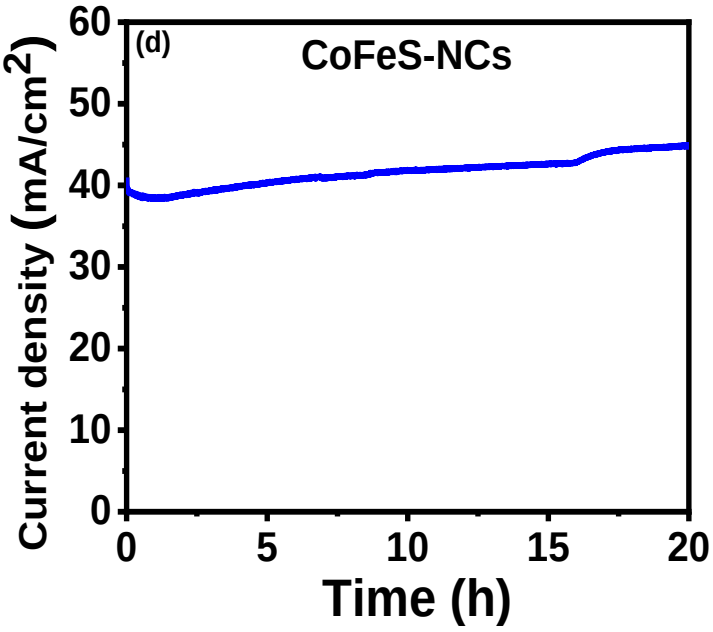

Figure 3.25d: CA plot of CoFeS-NCs for 20 hours.

The electrochemical impedance spectroscopy showed insignificant change in the internal resistance of the samples upon sulfurization; and therefore, a small change in OER overpotentials. The EIS results of CoFe samples are shown in the following figures.

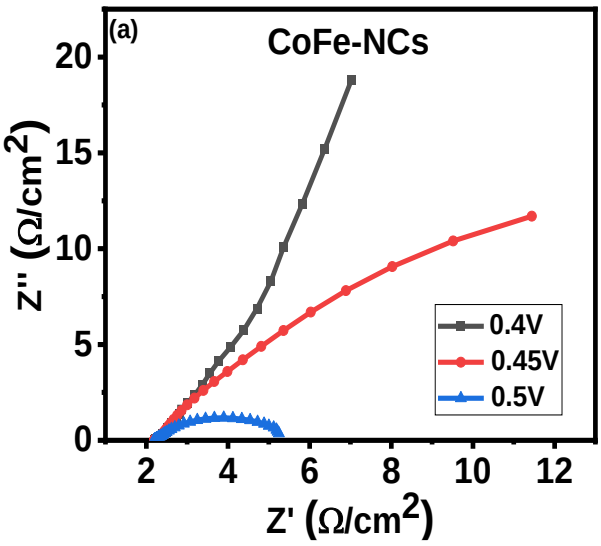

Figure 3.26a: Zim versus Zre of CoFe-NCs at different potentials.

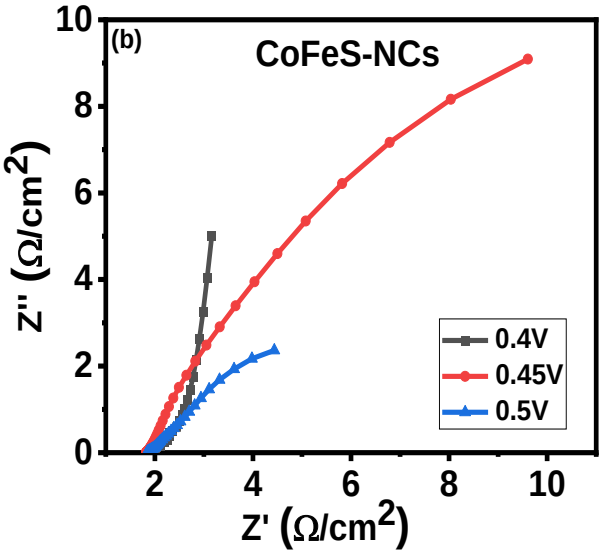

Figure 3.26b: Zim versus Zre of CoFeS-NCs at different potentials.

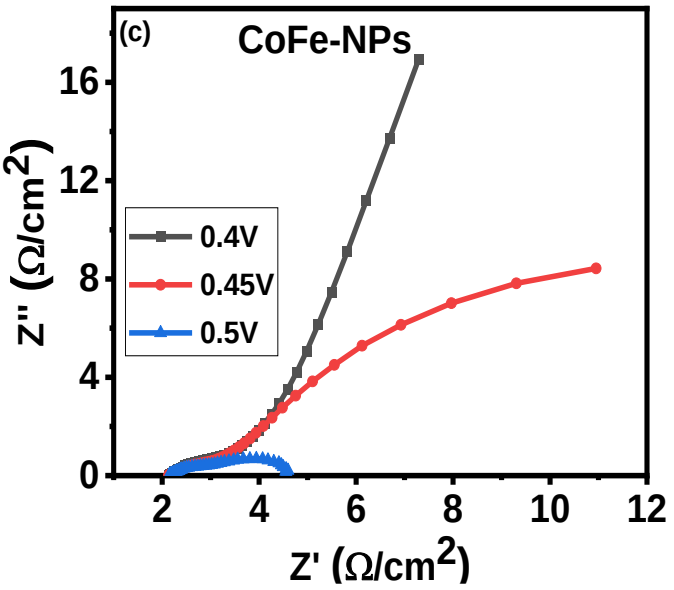

Figure 3.26c: Zim versus Zre of CoFe-NPs at different potentials.

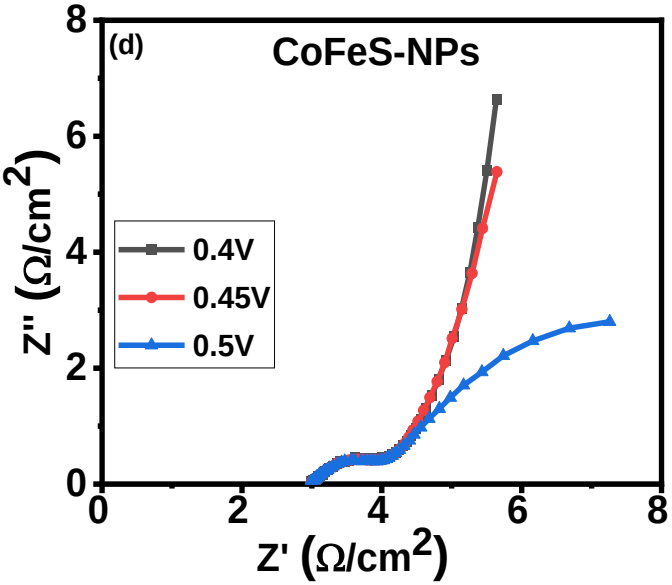

Figure 3.26d: Zim versus Zre of CoFeS-NPs at different potentials.

For the HER, there was a change in overpotentials after sulfurization. HER overpotentials changed from 113 mV for CoFe-NCs to 52 mV for CoFeS-NCs and from 161 mV for CoFe-NPs to 122 mV for CoFeS-NPs (Figure 3.27a). The linear sweep polarization curves showed resemblance for 1 and 1000 cycles. The HER results for CoFe samples are shown in the following figures.

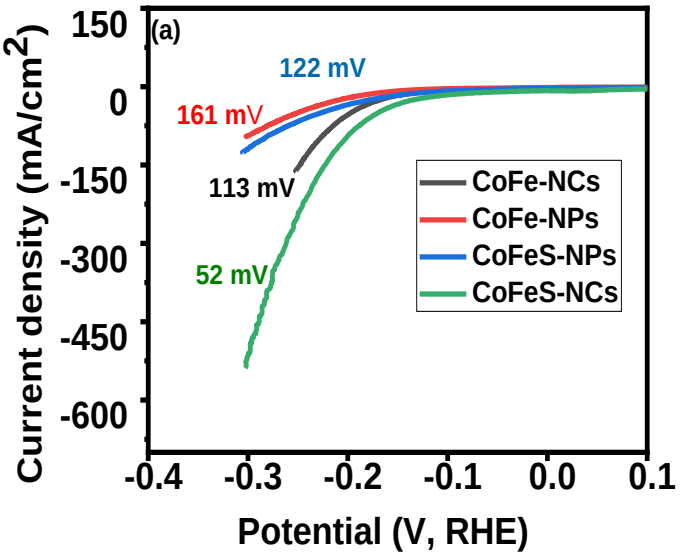

Figure 3.27a: LSV curves of CoFe samples.

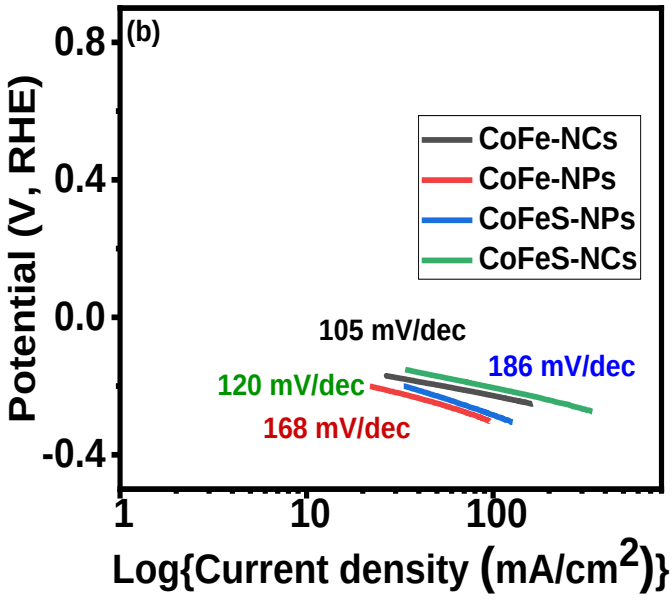

Figure 3.27b: Tafel plots and Tafel slopes of CoFe samples.

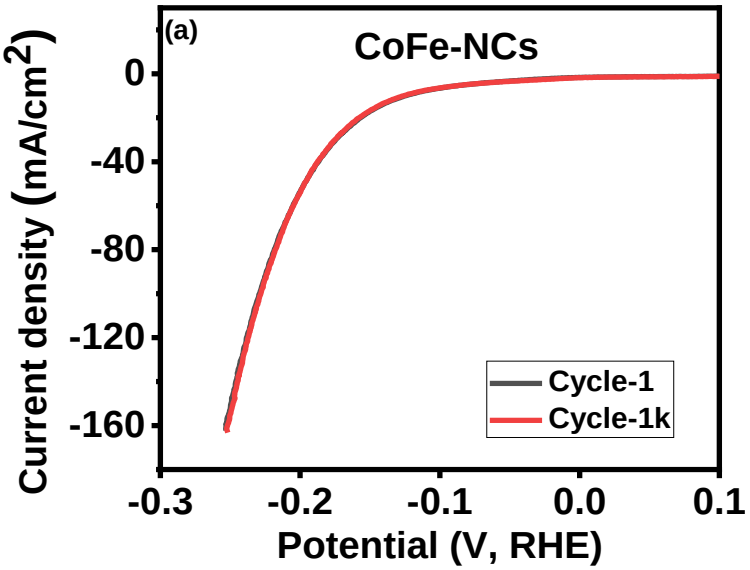

Figure 3.28a: LSV curves of CoFe-NCs at 1 and 1000 cycles.

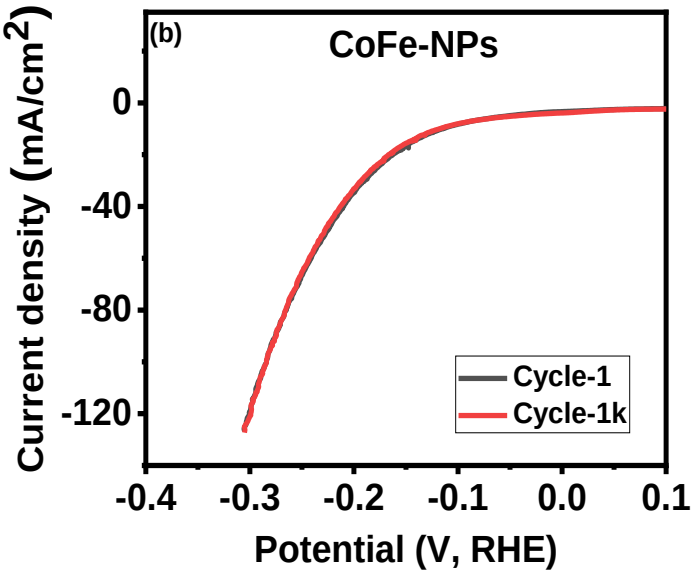

Figure 3.28b: LSV curves of CoFe-NPs at 1 and 1000 cycles.

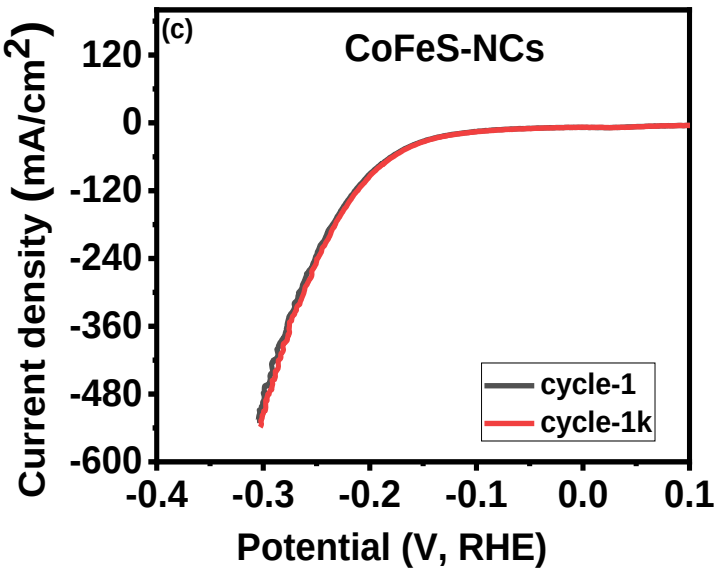

Figure 3.28c: LSV curves of CoFeS-NCs at 1 and 1000 cycles.

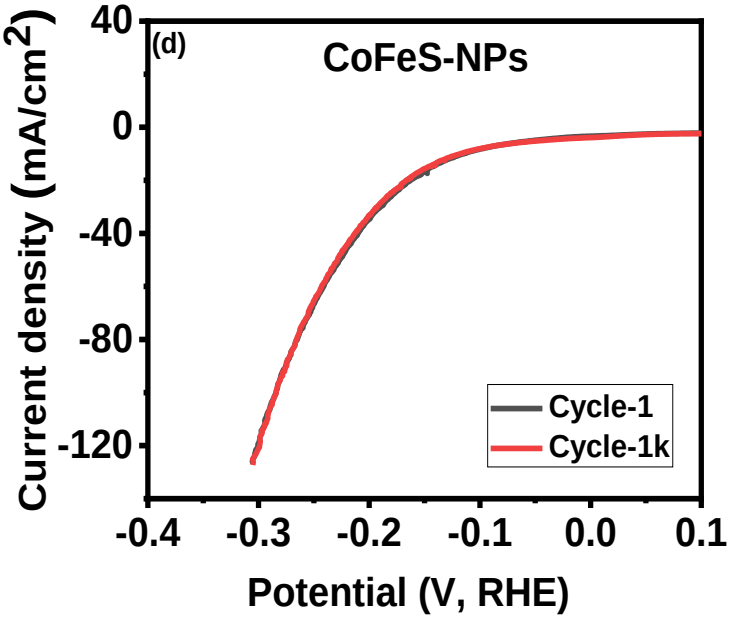

Figure 3.28d: LSV curves of CoFeS-NPs at 1 and 1000 cycles.

Cyclic voltammograms and galvanostatic charge-discharge of CoFe samples showed impressive reversible characteristics which suggest electrochemical stability of the materials, as revealed from the diagrams (Figures 3.29a-h).

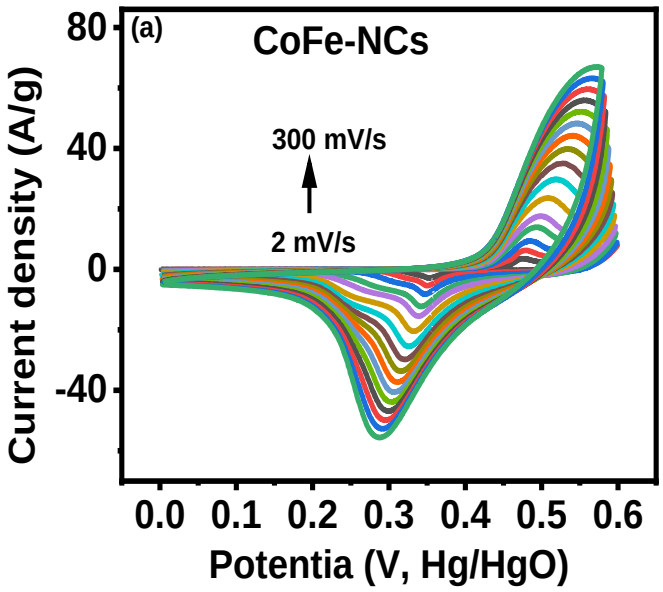

Figure 3.29a: Cyclic voltammograms of CoFe-NCs at various scan rates.

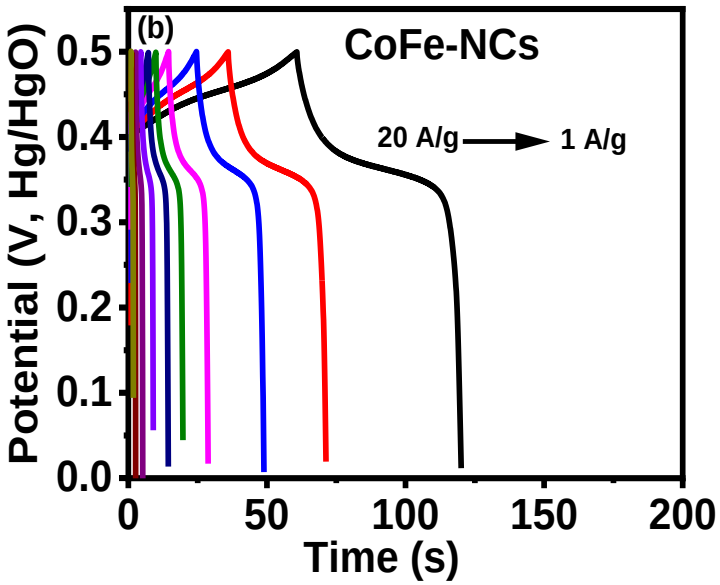

Figure 3.29b: Charge-discharge characteristics of CoFe-NCs at various currents.

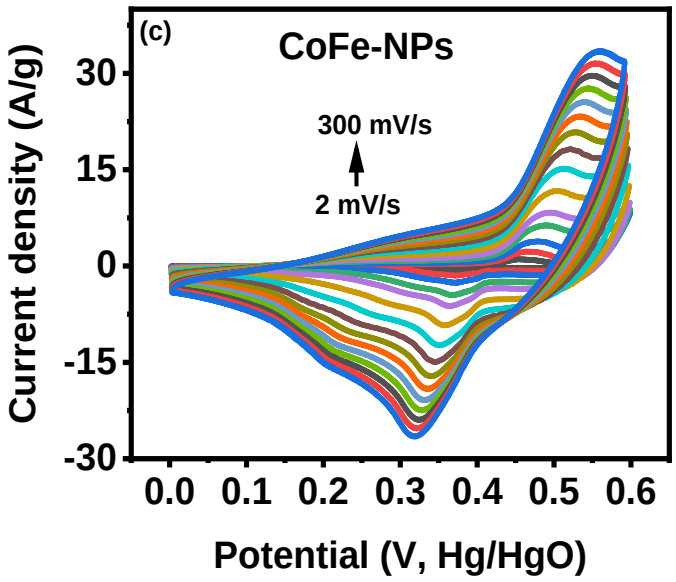

Figure 3.29c: Cyclic voltammograms of CoFe-NPs at various scan rates.

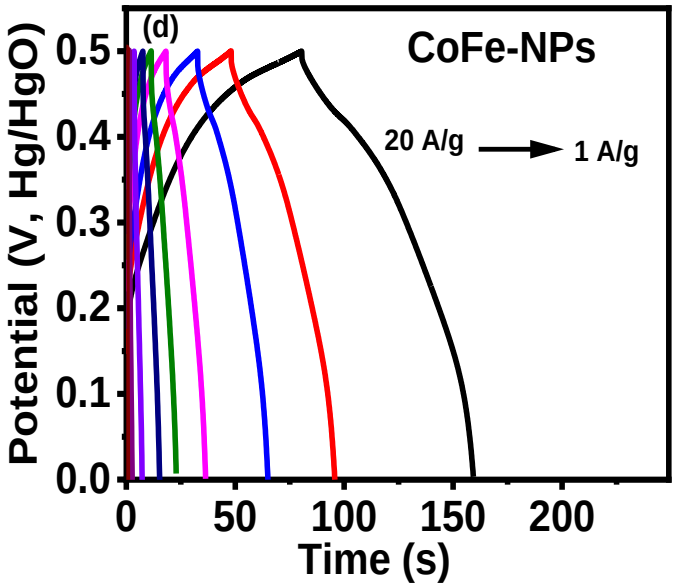

Figure 3.29d: Charge-discharge characteristics of CoFe-NPs at various currents.

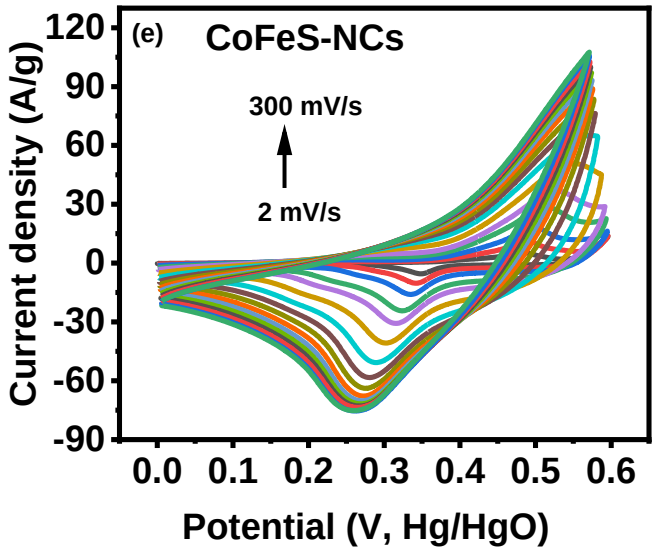

Figure 3.29e: Cyclic voltammograms of CoFeS-NCs at various scan rates.

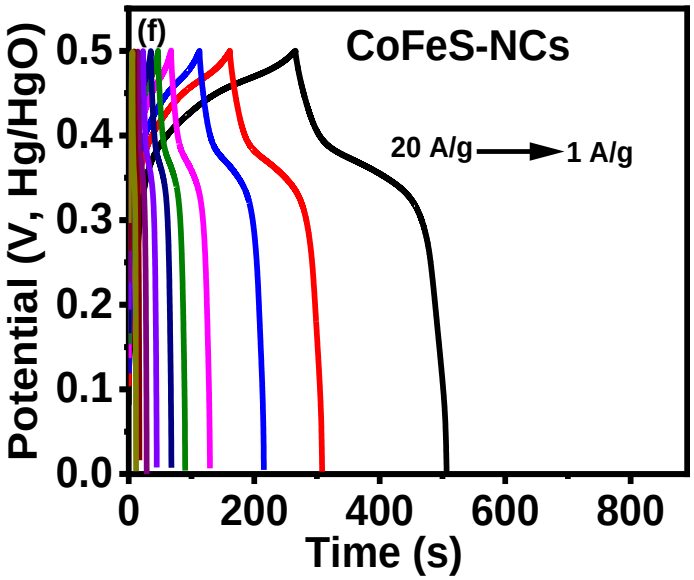

Figure 3.29f: Charge-discharge characteristics of CoFeS-NCs at various currents.

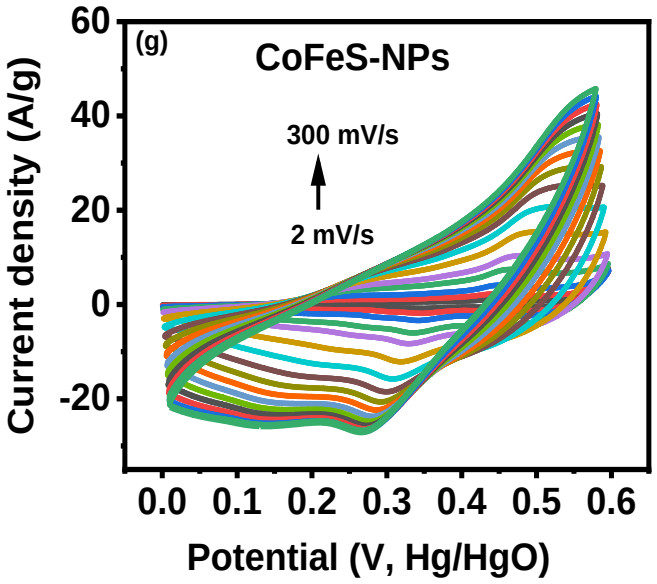

Figure 3.29g: Cyclic voltammograms of CoFeS-NPs at various scan rates.

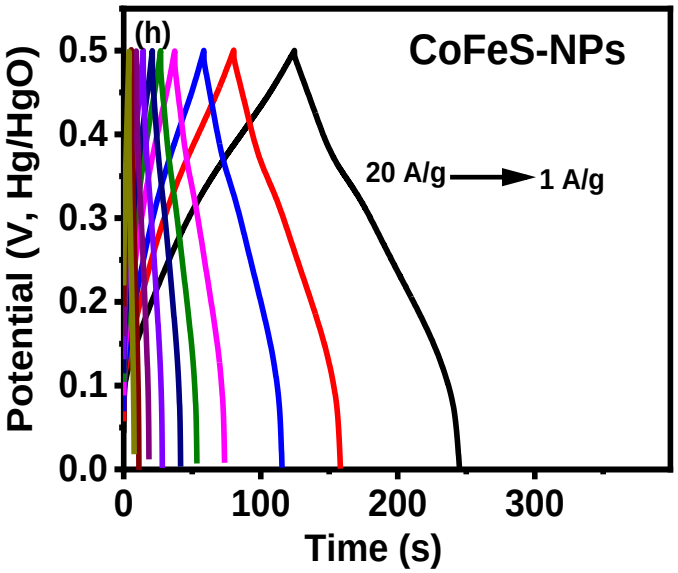

Figure 3.29h: Charge-discharge characteristics of CoFeS-NPs at various currents.

The specific capacitance improved for both NCs and NPs following sulfurization; where by 123 F/g specific capacitance of CoFe-NCs increased to 484 F/g for CoFeS-NCs and 161 F/g of CoFe-NPs to 244 F/g for CoFeS-NPs as shown in Figure 3.30.

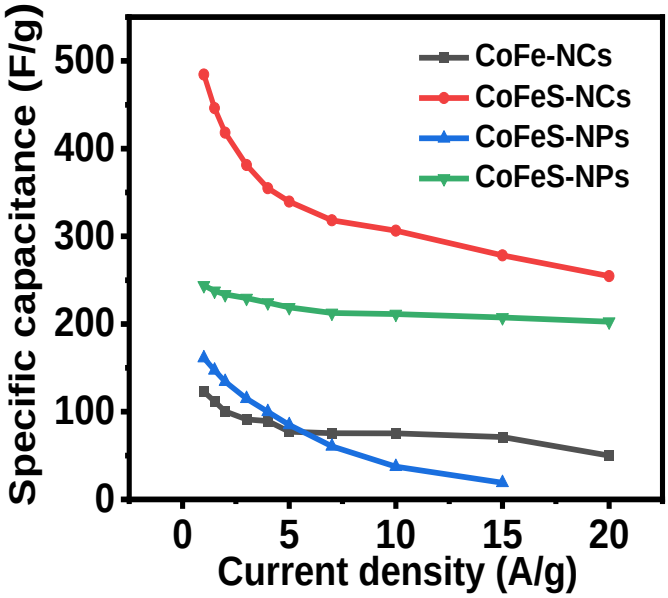

Figure 3.30: Variation of specific capacitance with current density.

Table 3.3: Comparison of specific capacitance of CoFe samples at 1 A/g before and after sulfurization.

Sample name	Specific capacitance (F/g)	Increment factor
CoFe-NCs	123	4
CoFeS-NCs	484	
CoFe-NPs	161	2
CoFeS-NPs	244	

The energy density of CoFe-NCs increased from 4 to 17 Wh/kg after sulfurization and for CoFe-NPs, the energy density increased from 5 to 8 Wh/kg (Figure 3.31a). The electrochemical impedance spectroscopy study showed a decrease of internal resistance

after sulfurization of materials (Figure 3.31b). The improvement of properties after sulfurization indicates that there were added electrons to the host materials and that the added electrons did not interfere the mobility of host materials electrons. The addition of sulfur must have changed and improved the materials' electric configuration [33].

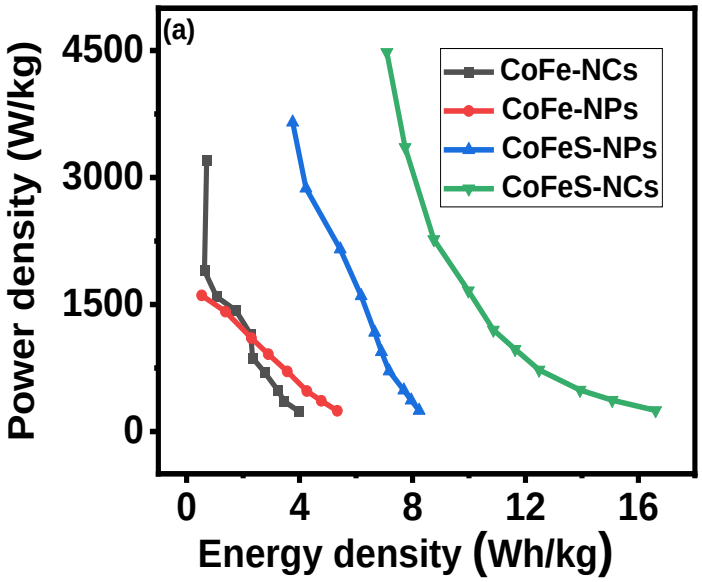

Figure 3.31a: Ragone plot of CoFe samples.

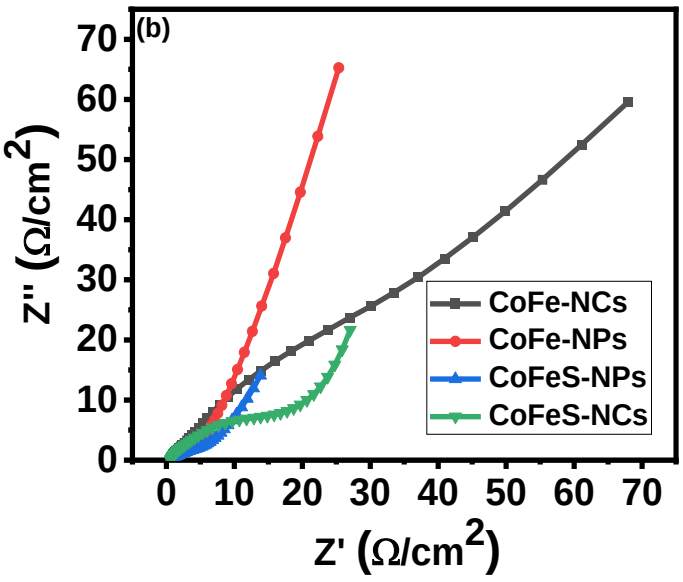

Figure 3.31b: Zim versus Zre showing reduced impendence after sulfurization.

Table 3.4: Comparison of energy densities of CoFe samples at 1 A/g before and after sulfurization.

Sample name	Energy density (Wh/kg)	Increment factor
CoFe-NCs	4	4
CoFeS-NCs	17	
CoFe-NPs	5	2
CoFeS-NPs	8	

To further investigate the properties, NiFe and CoFe samples were phosphorized and their properties were evaluated. The OER overpotentials seemed to increase for all samples after phosphorization, and so their Tafel slopes with 300, 330, 340, and 360 mV overpotentials for NiFeP-NPs, CoFeP-NCs, NiFeP-NCs, and CoFeP-NPs, respectively (Figure

3.32a), were higher than their respective unphosphorized counterparts which showed 256, 300, 298, and 300 mV overpotentials (Figures 3.14a and 3.23a). This was evidenced from OER EIS plots where the internal resistance of samples seemed to increase as compared to the unphosphorized samples (Figures 3.16a, 3.16b, 3.26a, 3.26c, and 3.34a-d) and hence lead to an increase of overpotentials. The 1 and 1000 cycles OER LSV polarization curves were highly stable as they seemed to be alike and coincide (Figures 3.34a-d). The OER results for phosphorized samples are shown in the following diagrams.

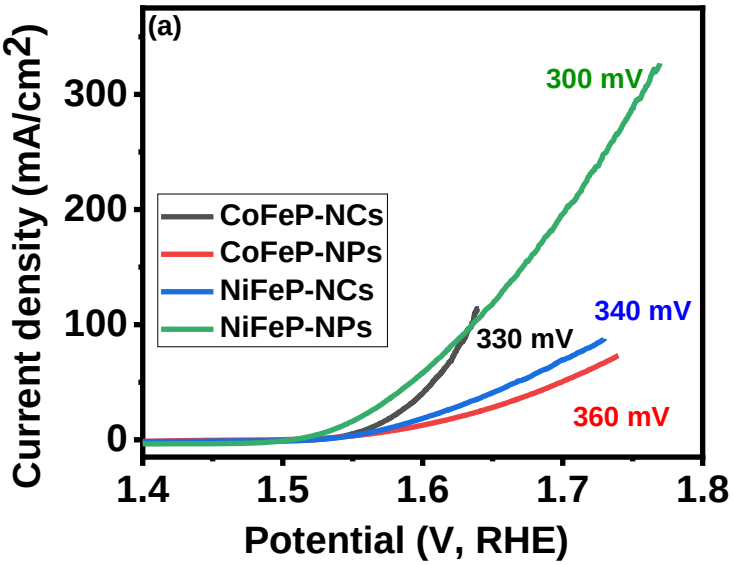

Figure 3.32a: OER LSV curves of phosphorized samples.

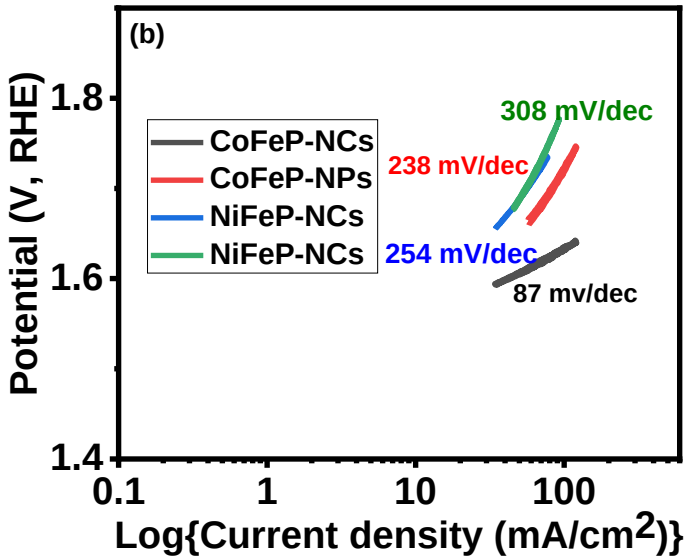

Figure 3.32b: Tafel plots of phosphorized samples.

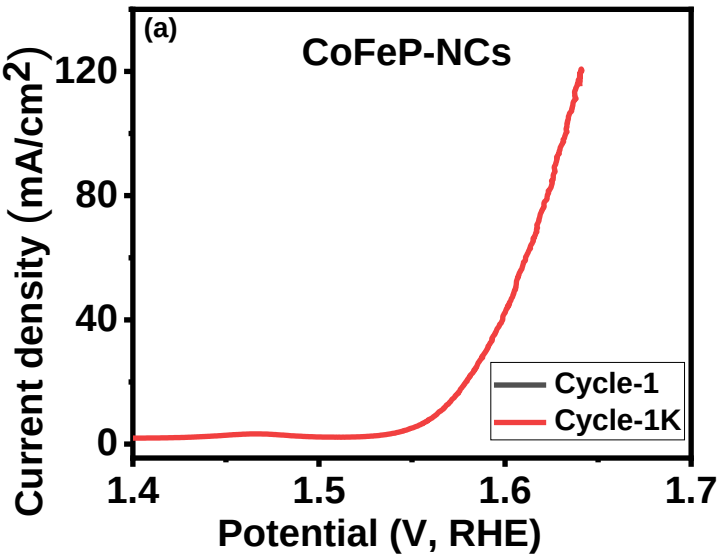

Figure 3.33a: LSV curves of CoFeP-NCs at 1 and 1000 cycles.

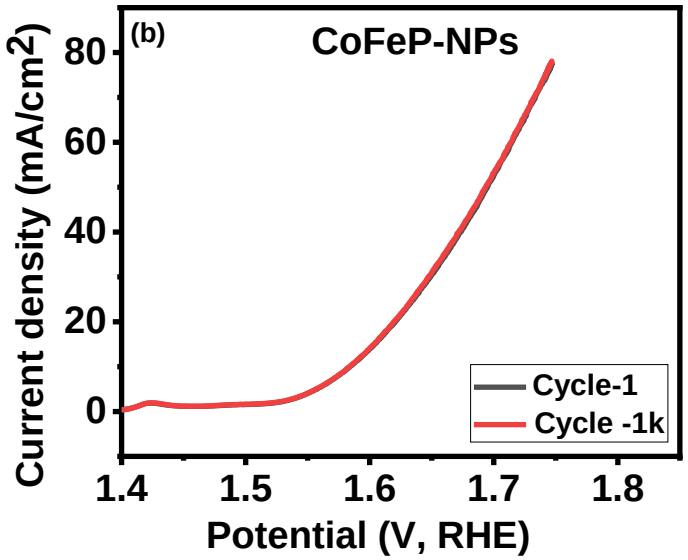

Figure 3.33b: LSV curves of CoFeP-NPs at 1 and 1000 cycles.

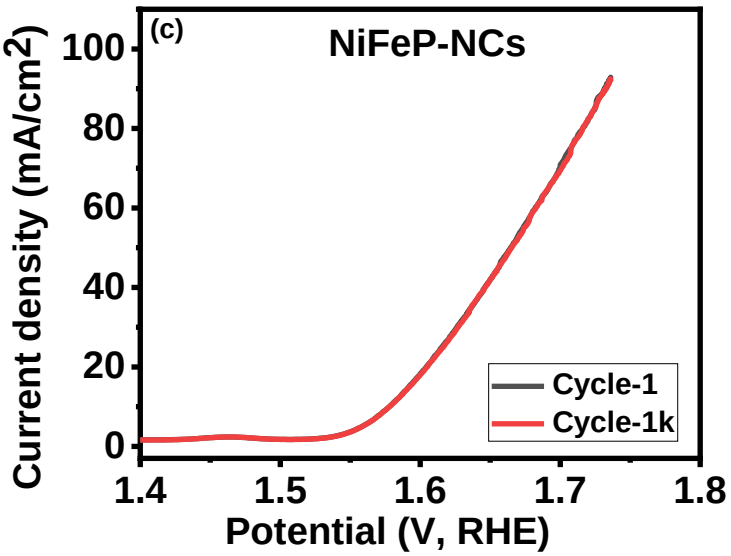

Figure 3.33c: LSV curves of NiFeP-NCs at 1 and 1000 cycles.

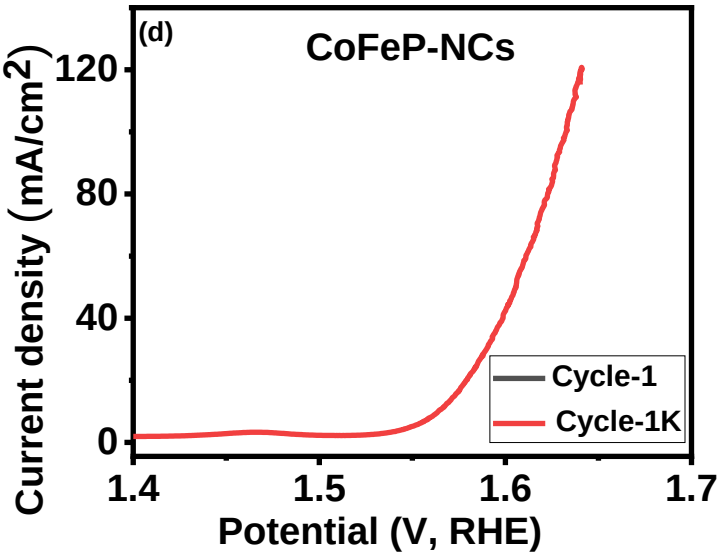

Figure 3.33d: LSV curves of CoFeP-NCs at 1 and 1000 cycles.

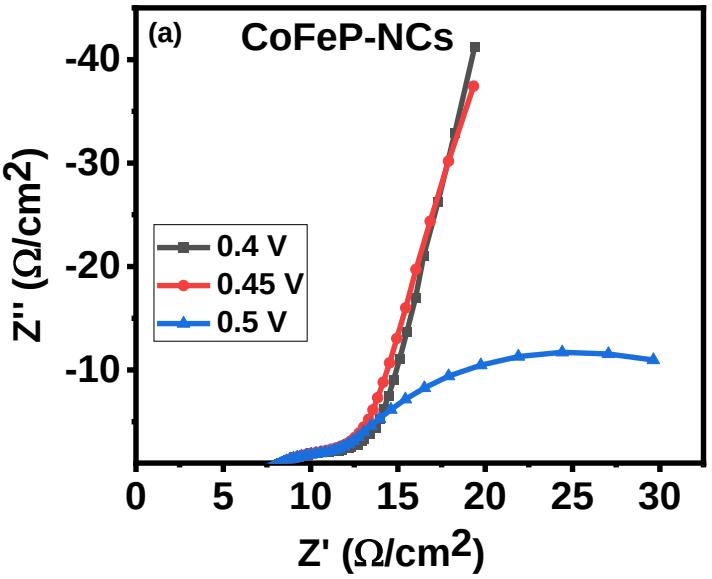

Figure 3.34a: Zim versus Zre of CoFeP-NCs at different potentials.

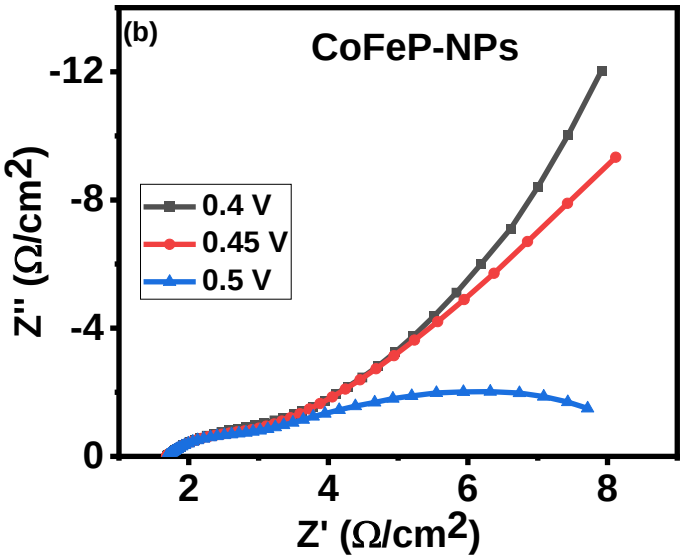

Figure 3.34b: Zim versus Zre of CoFeP-NPs at different potentials.

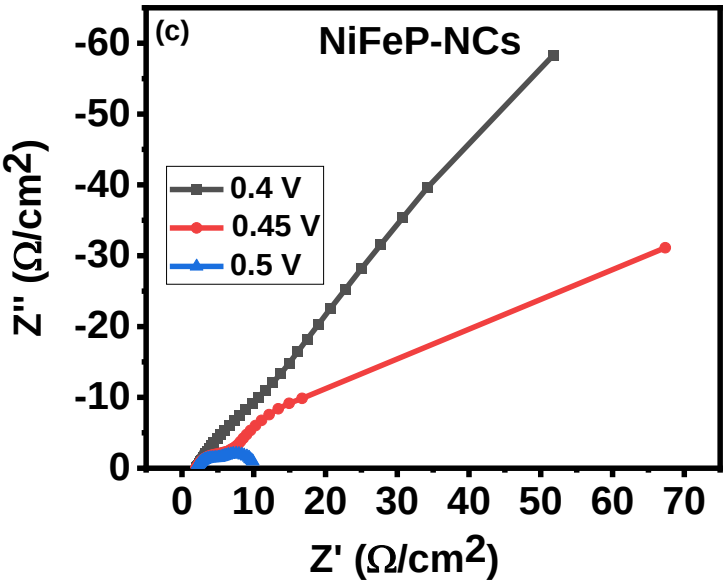

Figure 3.34c: Zim versus Zre of NiFeP-NCs at different potentials.

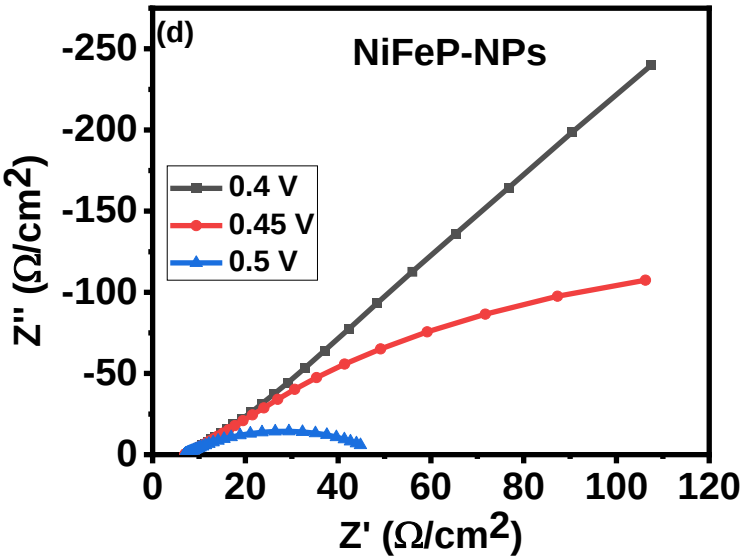

Figure 3.34d: Zim versus Zre of NiFeP-NPs at different potentials.

The 20 hours chronoamperometric test showed good durability of the samples. The electric current potentially remained steady as shown in the following figures.

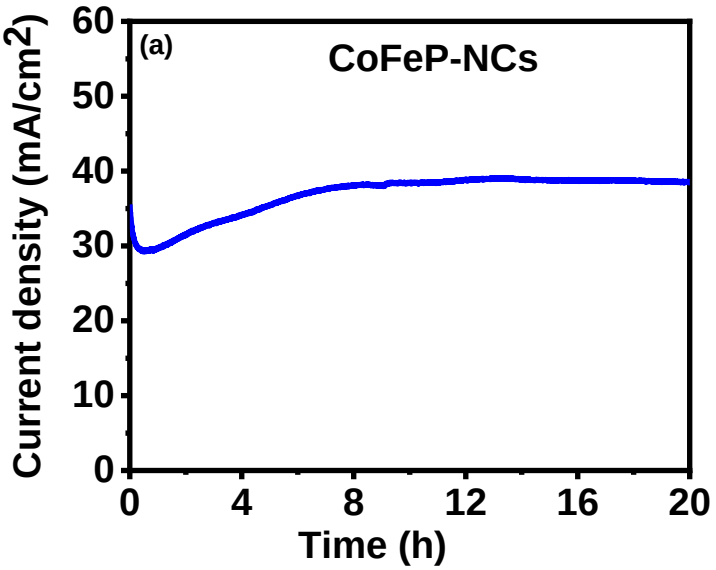

Figure 3.35a: CA plot of CoFeP-NCs for 20 hours.

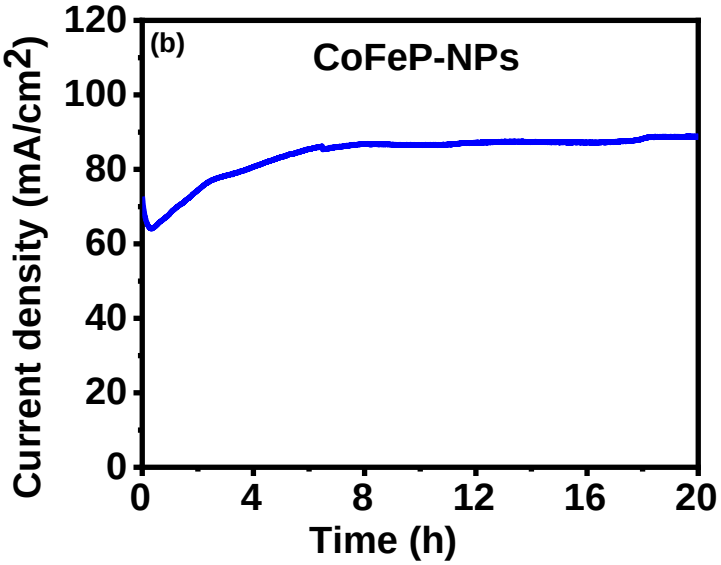

Figure 3.35b: CA) plot of CoFeP-NPs for 20 hours.

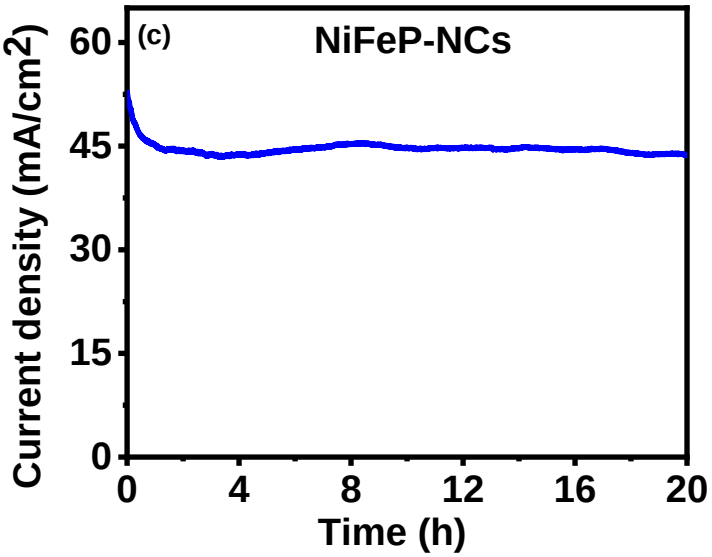

Figure 3.35c: CA plot of NiFeP-NCs for 20 hours.

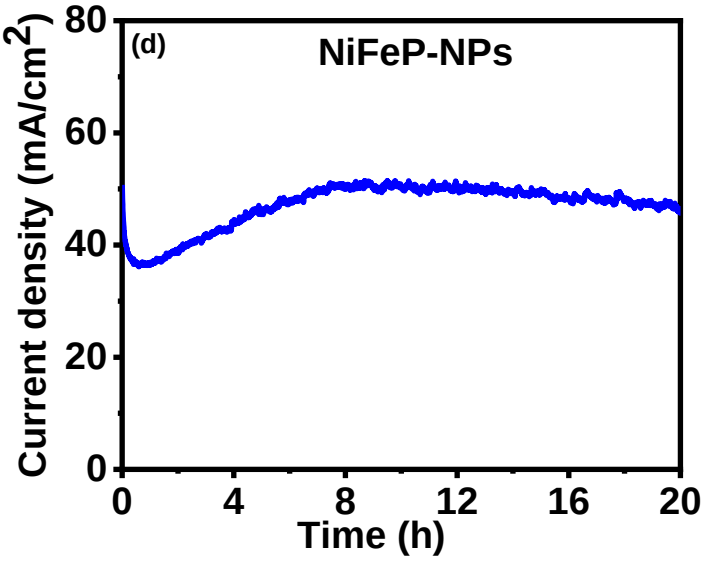

Figure 3.35d: CA plot of NiFeP-NPs for 20 hours.

For most of the samples, HER overpotentials seemed to improve/decrease when compared to their unphosphorized counterparts, where by 135, 121, 118, and 84 mV were determined for NiFeP-NPs, NiFeP-NCs, CoFeP-NPs, and CoFeP-NCs, respectively (Figure 3.36a). The respective unphosphorized samples HER overpotentials were 187, 54, 161, and 113 mV (Figures 3.18a and 3.27a). The materials showed good stability as seen in the LSV polarization curves. The results for HER are shown in the following figures.

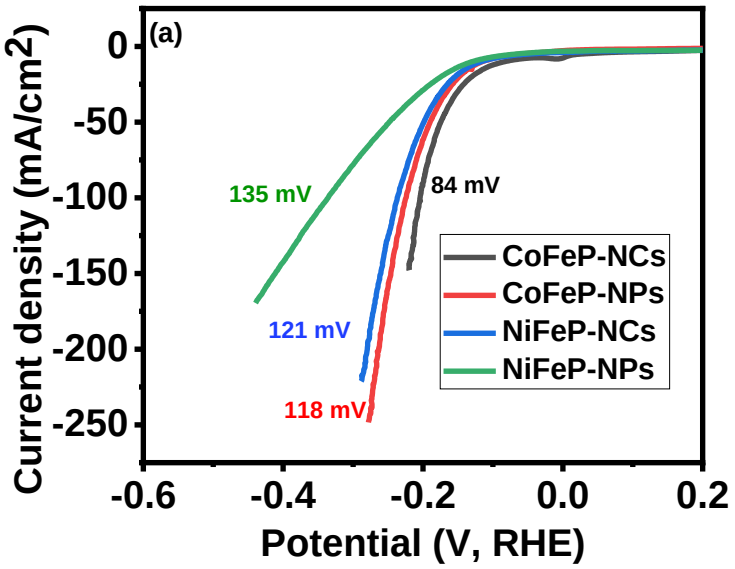

Figure 3.36a: LSV curves of phosphorized samples.

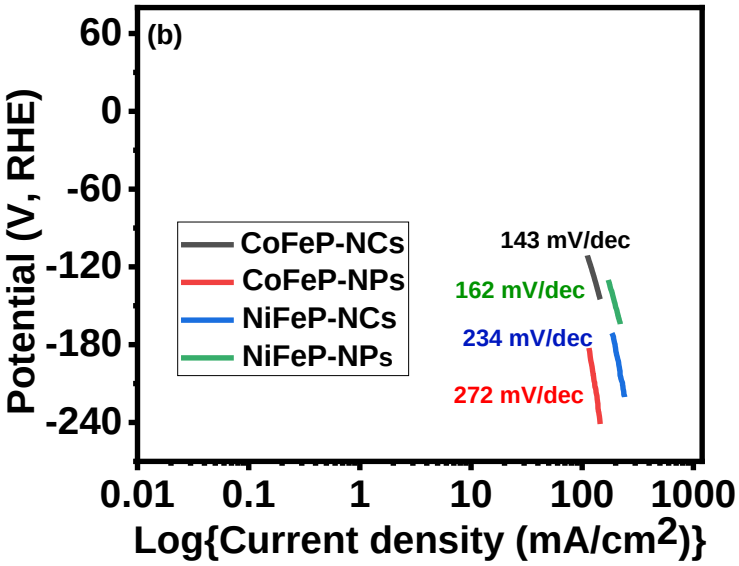

Figure 3.36b: Tafel plots of phosphorized samples.

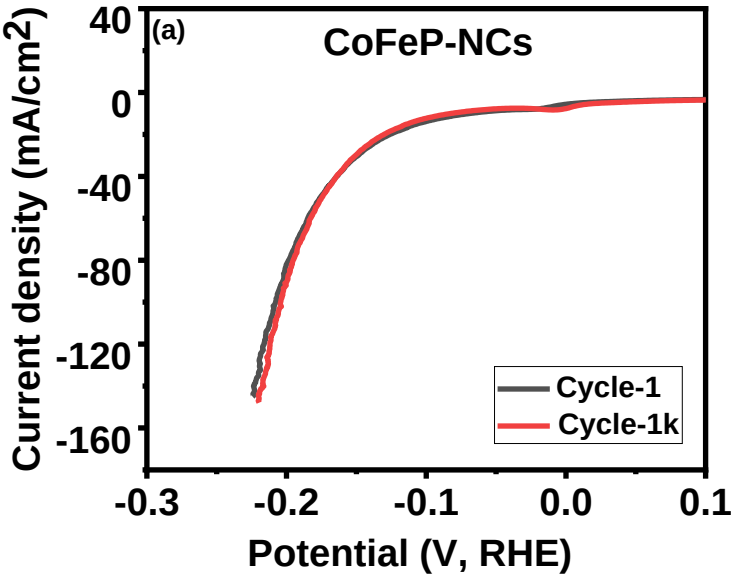

Figure 3.37a: LSV curves of CoFeP-NCs at 1 and 1000 cycles.

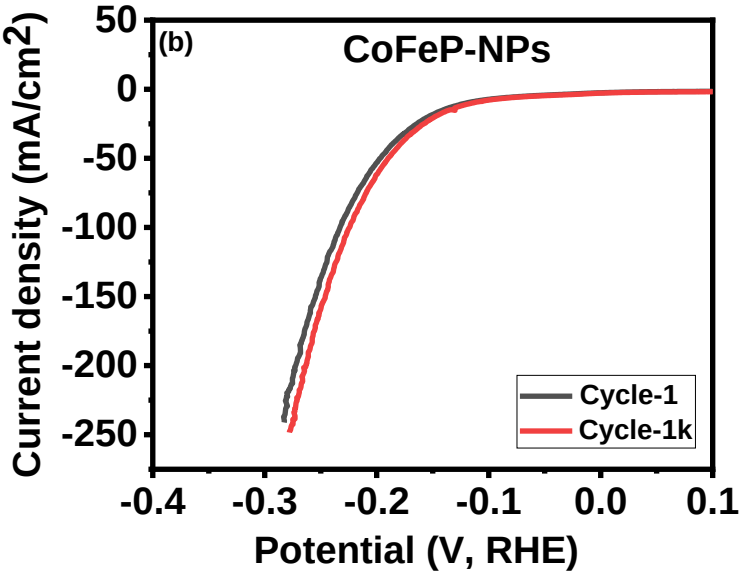

Figure 3.37b: LSV curves of CoFeP-NPs at 1 and 1000 cycles.

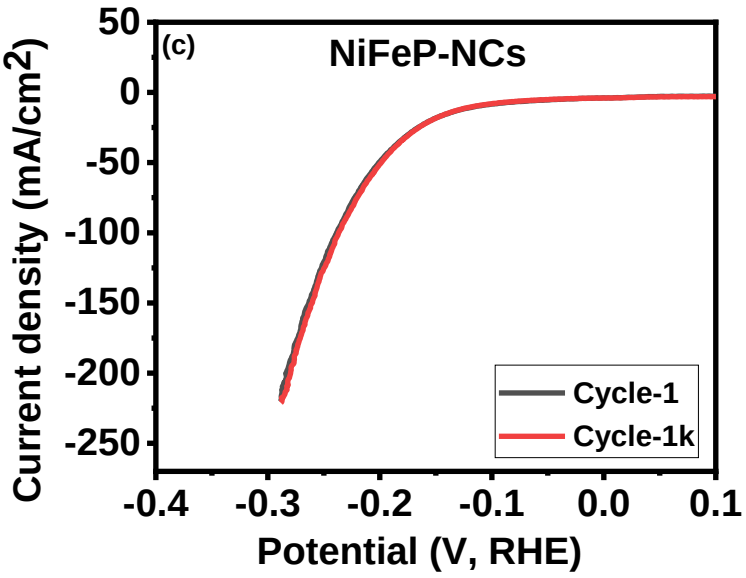

Figure 3.37c: LSV curves of NiFeP-NCs at 1 and 1000 cycles.

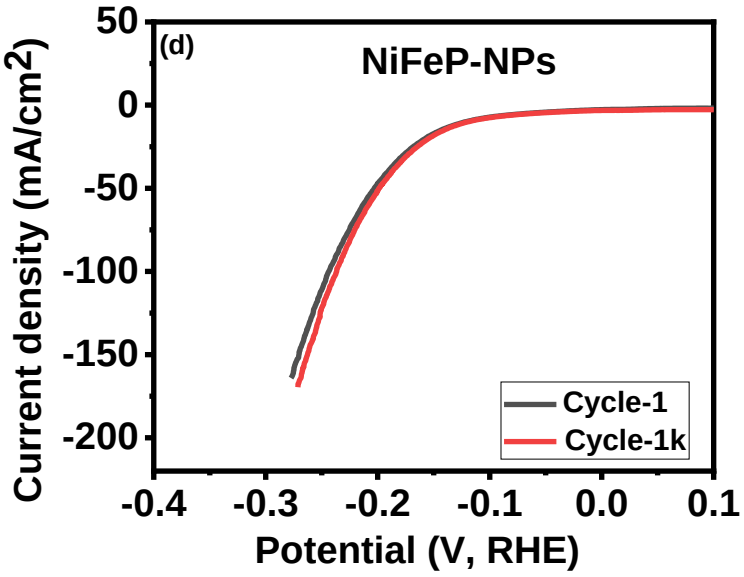

Figure 3.37d: LSV curves of NiFeP-NPs at 1 and 1000 cycles.

The excellent cyclic voltammograms and galvanostatic charge-discharge curves signify good electrochemical stability and that the added phosphorus significantly improved the materials' structure and conductivity (Figures 3.38a-h). Previous research has shown that phosphate-doped materials achieve good capacitive behavior [34]. The results for cyclic voltammograms and galvanostatic charge-discharge characteristics of phosphorized samples are shown in the following figures.

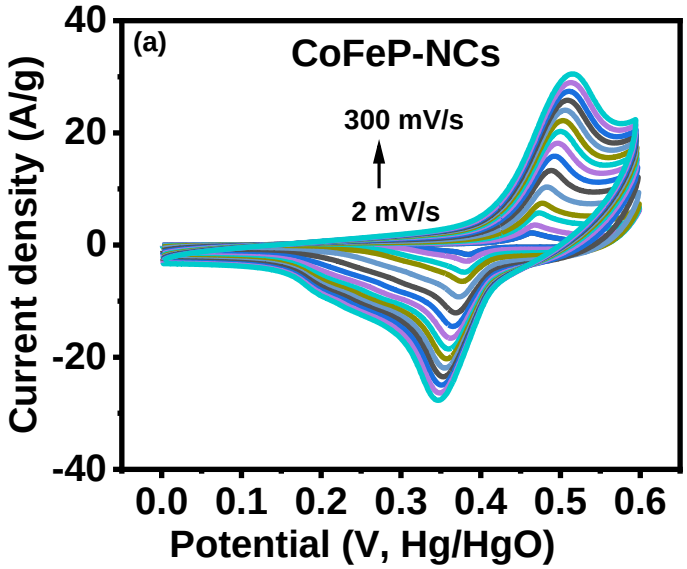

Figure 3.38a: Cyclic voltammograms of CoFeP-NCs at various scan rates.

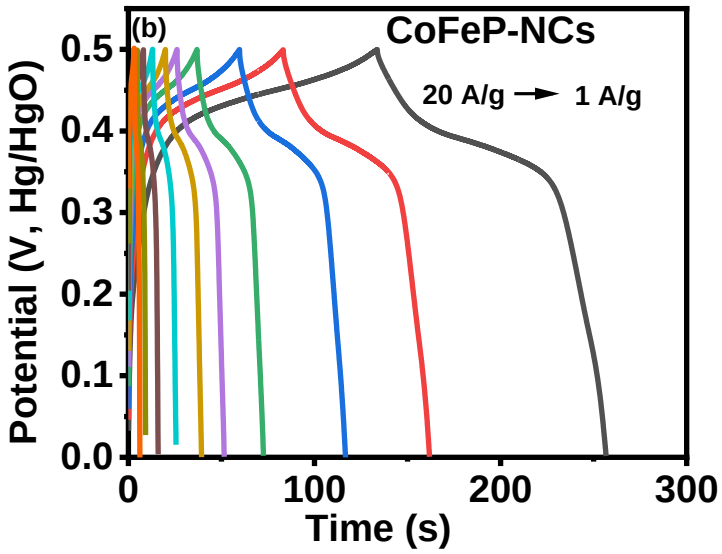

Figure 3.38b: Charge-discharge characteristics of CoFeP-NCs at various currents.

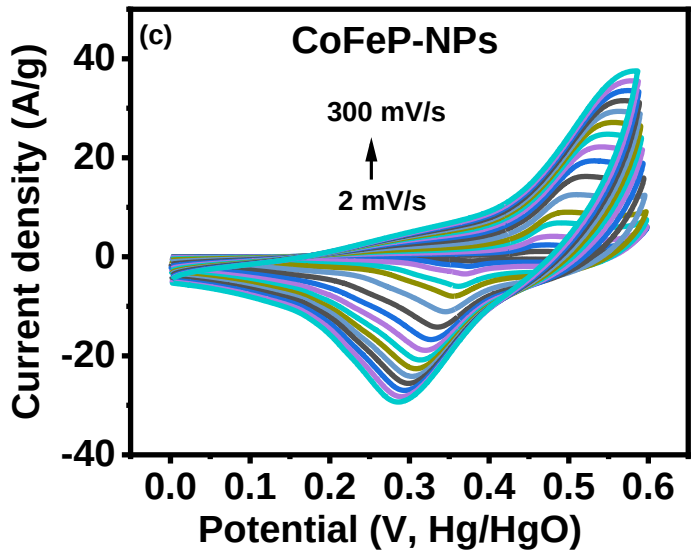

Figure 3.38c: Cyclic voltammograms of CoFeP-NPs at various scan rates.

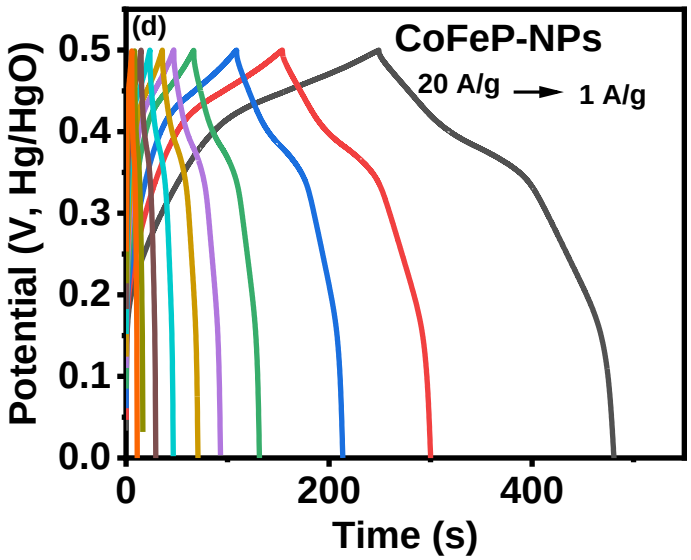

Figure 3.38d: Charge-discharge characteristics of CoFeP-NPs at various currents.

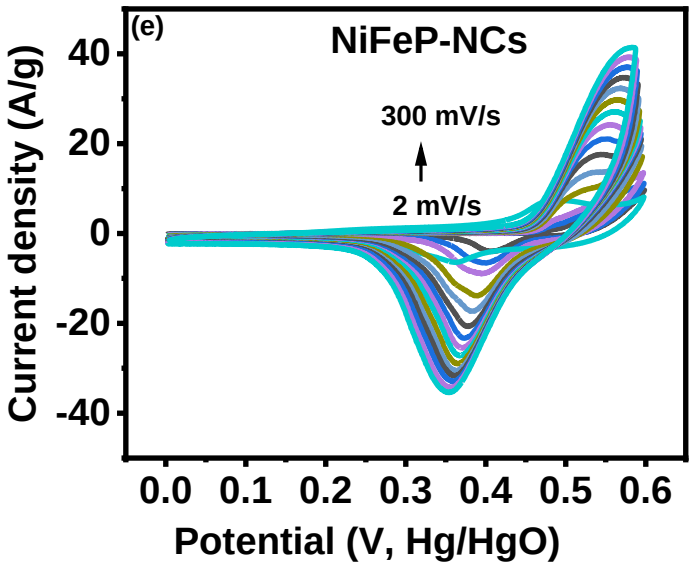

Figure 3.38e: Cyclic voltammograms of NiFeP-NCs at various scan rates.

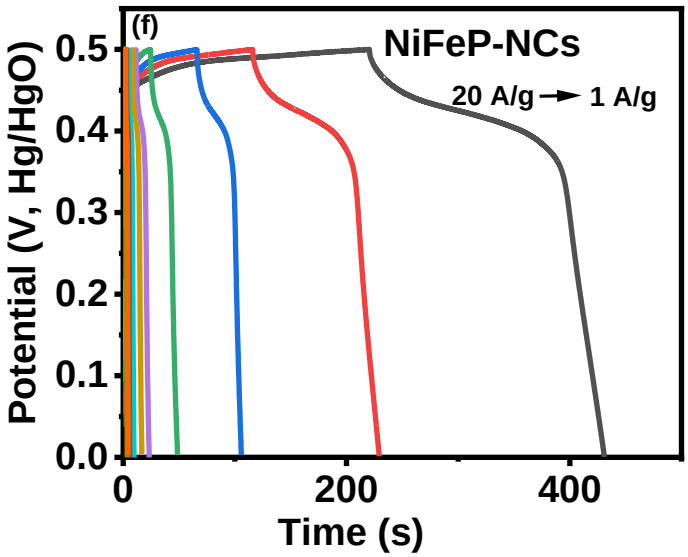

Figure 3.38f: Charge-discharge characteristics of NiFeP-NCs at various currents.

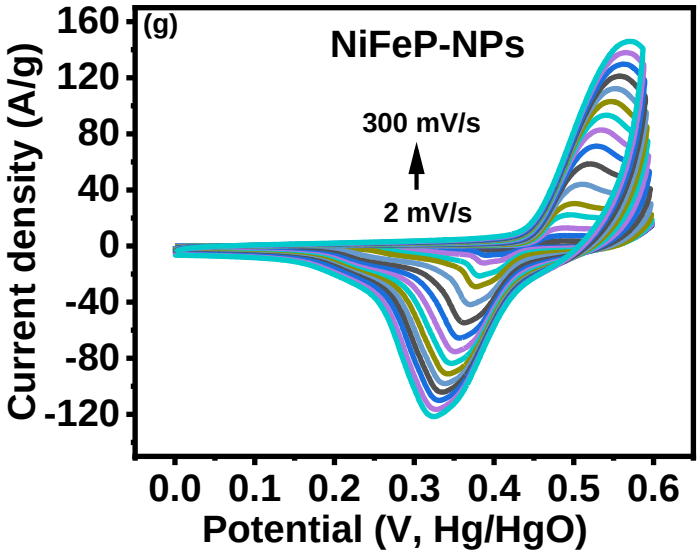

Figure 3.38g: Cyclic voltammograms of NiFeP-NPs at various scan rates.

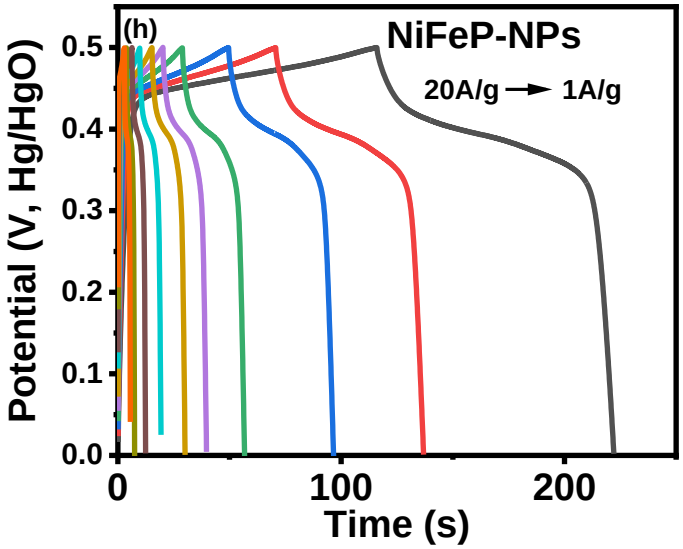

Figure 3.38h: Charge-discharge characteristics of NiFeP-NPs at various currents.

On the other hand, the specific capacitance of the phosphorized samples was improved as shown in table 3.5 and Figure 3.39.

Table 3.5: Comparison of specific capacitance at 1 A/g before and after phosphorization of samples.

Sample name	Specific capacitance (F/g)	Increment factor
CoFe-NCs	123	2
CoFeP-NCs	248	
CoFe-NPs	161	3
CoFeP-NPs	464	
NiFe-NCs	69	6
NiFeP-NCs	424	
NiFe-NPs	186	1
NiFeP-NPs	214	

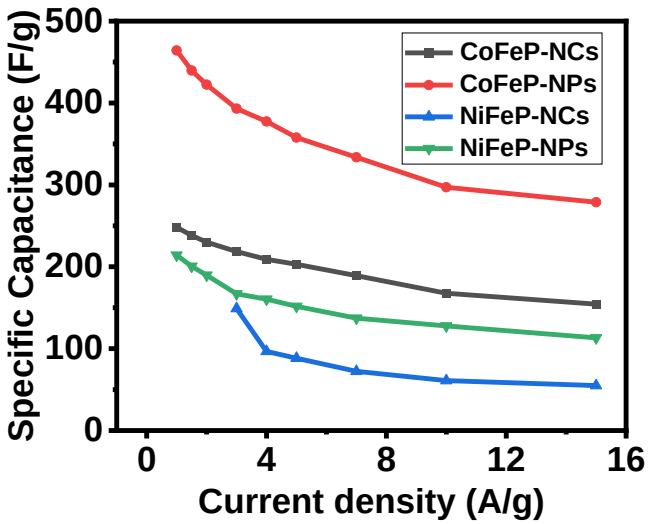

Figure 3.39: Variation of specific capacitance with current density.

The energy and power density of the phosphorized samples were evaluated as shown in the Ragone plot (Figure 3.40a). Table 3.6 illustrates the improved energy densities of phosphorized NiFe and CoFe samples.

Table 3.6: Comparison of energy densities before and after phosphorization of samples.

Sample name	Energy density (Wh/kg)	Increment factor
CoFe-NCs	4	2
CoFeP-NCs	8	
CoFe-NPs	5	3
CoFeP-NPs	16	
NiFe-NCs	2	7
NiFeP-NCs	15	
NiFe-NPs	6	1
NiFeP-NPs	7	

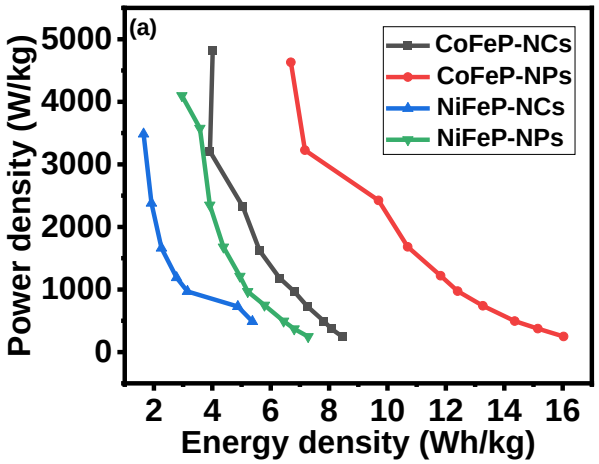

Figure 3.40a: Ragone plot of phosphorized samples.

The electrochemical impedance spectroscopy (Figure 3.40b) depicts the properties shown by individual samples; where by CoFeP-NPs, which should have the lowest internal resistance, has the highest specific capacitance and energy density.

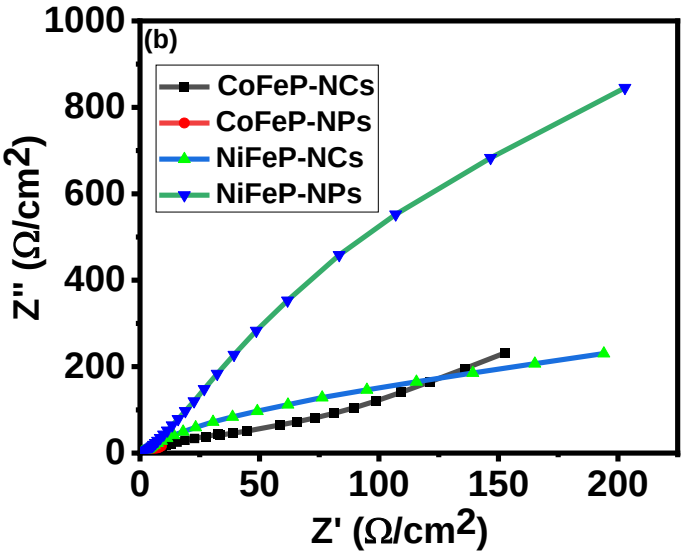

Figure 3.40b: Zim versus Zre of phosphorized samples.

CHAPTER IV

CONCLUSION

In summary, the synthesized materials revealed promising outcomes for energy solutions. The fabricated and studied materials were in three categories; NiFe nanoparticles and nanocubes, CoFe nanoparticles and nanocubes, and phosphorized NiFe and CoFe nanoparticles and nanocubes; and were synthesized by a facile coprecipitation method. NiFe-oxide nanoparticles and nanocubes showed good OER and HER results, with NiFe-NCs indicating 298 mV and 54 mV as OER and HER onset overpotentials respectively, while NiFe-NPs had overpotentials of 258 mV and 187 mV for OER and HER respectively. On sulfurization, their results were further improved, with the exception of NiFe-NCs, whose HER overpotential was increased from 54 to 177 mV after doping with sulfur; the rest of the samples showed improvement in their OER and HER overpotentials, from 298 mV for NiFe-NCs to 241 mV for NiFeS-NCs in OER, 258 mV for NiFe-NPs to 216 mV for NiFeS-NPs in OER; and 187 mV for NiFe-NPs to 152 mV for NiFeS-NPs in HER. On the other hand, the materials' specific capacitance seemed to increase from 69 to 605 F/g for sulfurized NiFe-NCs and 186 to 515 F/g for sulfurized NiFe-NPs. Furthermore, the energy density of materials increased from 2 to 20 Wh/kg for NiFe-NCs and NiFeS-NCs, and from 6 to 17 Wh/kg for NiFe-NPs and NiFeS-NPs respectively, at 1 A/g.

CoFe oxide nanocubes and nanoparticles showed tremendous electrocatalytic and storage behavior. The samples showed nearly the same overpotentials of ≈300 mV for oxygen evolution reactions, and improved overpotentials for hydrogen evolution reactions after sulfurization; overpotentials decreased from 113 mV for CoFe-NCs to 52 mV for CoFeS-NCs and from 161 mV for CoFe-NPs to 122 mV for CoFeS-NPs. The specific capacitance improved for both NCs and NPs after sulfurization; where by 123 F/g specific capacitance of CoFe-NCs increased to 484 F/g for CoFeS-NCs and 161 F/g of CoFe-NPs to 244 F/g for CoFeS-NPs. The energy density of CoFe-NCs increased from 4 to 17 Wh/kg after sulfurization, whereas for CoFe-NPs, the energy density increased from 5 to 8 Wh/kg, at 1 A/g.

It was also observed that phosphorization of materials might greatly tune their properties; OER overpotentials increased for all samples after phosphorization, with 300, 330, 340, and 360 mV for NiFeP-NPs, CoFeP-NCs, NiFeP-NCs, and CoFeP-NPs respectively, as compared to their unphosphorized counterparts, with 256, 300, 298, and 300 mV overpotentials. The overpotentials for HER seemed to decrease when compared to their unphosphorized counterparts, where by the 135, 121, 118, and 84 mV were determined for NiFeP-NPs, NiFeP-NCs, CoFeP-NPs, and CoFeP-NCs as compared to their unphosphorized samples overpotentials of 187, 54, 161, and 113 mV respectively. The specific capacitances of phosphorized samples were significantly improved; whereby for CoFe-NCs, it increased from 123 to 248 F/g, 161 to 464 F/g for CoFe-NPs, 69 to 424 F/g for NiFe-NCs, and 186 to 214 F/g for NiFe-NPs. The energy densities were also greatly improved after doping with phosphorus in which for CoFe-NCs, the energy density

increased from 4 to 9 Wh/kg, from 5 to 16 Wh/kg for CoFe-NPs, from 2 to 15 Wh/kg for NiFe-NCs, and 6 to 7 Wh/kg for NiFe-NPs. The research study suggests that a facile sulfurization and phosphorization process could significantly improve the catalytic and capacitive behavior of metal oxides.

REFERENCES

1. Sharma S, Jain KK, Sharma A (2015) Solar Cells: In Research and Applications—A Review. Mater Sci Appl 06:1145–1155
2. Winter M, Brodd RJ (2004) What are batteries, fuel cells, and supercapacitors? Chem Rev 104:4245–4269
3. Smith MJ, Vincent CA (2001) Structure and content of some primary batteries. J Chem Educ 78:519–521
4. Kumari YASJP, Padmaja K, Kumari PR (2018) A fuel cell and its applications. AIP Conf Proc 1992:40013–40016
5. Huang ZH, Song Y, Feng DY, et al (2018) High Mass Loading MnO2 with Hierarchical Nanostructures for Supercapacitors. ACS Nano 12:3557–3567
6. Zhang M, He L, Shi T, Zha R (2018) Nanocasting and Direct Synthesis Strategies for Mesoporous Carbons as Supercapacitor Electrodes. Chem Mater 30:7391–7412
7. Kim BK, Sy S, Yu A ZJ (2015) Electrochemical Supercapacitors for Energy Storage and Conversion. In: Handbook of Clean Energy Systems. John Wiley & Sons, Ltd, pp 2775–2800
8. Lian C, Liu K, Van Aken KL, et al (2016) Enhancing the Capacitive Performance of Electric Double-Layer Capacitors with Ionic Liquid Mixtures. ACS Energy Lett 1:21–26
9. Jilei L, Jin W CX et al (2017) Advanced Energy Storage Devices: Basic Principles,Analytical Methods, and Rational Materials Design. Adv Sci 5:1700322
10. Lu P, Xue D, Yang H, Liu Y (2013) Supercapacitor and nanoscale research towards electrochemical energy storage. Int J Smart Nano Mater 4:2–26
11. Zheng J, Zhang R, Cheng K, et al (2019) Research on the high-performance electrochemical energy storage of a NiO@ZnO (NZO) hybrid based on growth time. Crystals 9:1–14

12. Young KH, Ouchi T, Huang B, Nei J (2015) Structure, hydrogen storage, and electrochemical properties of body-centered-cubic Ti 40 V 30 Cr 15 Mn 13 X 2 Alloys (X = B, Si, Mn, Ni, Zr, Nb, Mo, and La). Batteries 1:74–90

13. Inkson BJ (2016) Scanning electron microscopy and Transmission electron microscopy for materials characterization. In: Materials Characterization Using Nondestructive Evaluation (NDE) Methods. Elsevier, pp 17–43

14. J. Epp (2016) X-ray diffraction (XRD) techniques for materials characterization. In: Materials Characterization Using Nondestructive Evaluation (NDE) Methods. Elsevier, pp 81–124

15. Ganesan P, Sivanantham A, Shanmugam S (2016) Inexpensive electrochemical synthesis of nickel iron sulphides on nickel foam: Super active and ultra-durable electrocatalysts for alkaline electrolyte membrane water electrolysis. J Mater Chem A 4:16394–16402

16. Long X, Li G, Wang Z, et al (2015) Metallic Iron-Nickel Sulfide Ultrathin Nanosheets As a Highly Active Electrocatalyst for Hydrogen Evolution Reaction in Acidic Media. J Am Chem Soc 137:11900–11903

17. Biju V, Abdul Khadar M (2002) Electronic structure of nanostructured nickel oxide using Ni 2p XPS analysis. J Nanoparticle Res 4:247–253

18. Wenxin Z, Xiaoyue Y WZ et al (2016) Nickel sulfide microspheres film on Ni foam as an efficient bifuctional electrocatalyst for overrall water splitting. Chem Commun 52:1486–1489

19. Niu S, Li S, Hu J, et al (2019) Fabrication of uniform Ru-doped NiFe2O4 nanosheets as an efficient hydrogen evolution electrocatalyst. Chem Commun 55:14649–14652

20. Shi Z, Zhang J, Gao D, et al (2013) Magnetic resonance of the NiFe2O4 nanoparticles in the gigahertz range. Nanoscale Res Lett 8:1–5

21. Gao D, Zhang J, Yang G, et al (2010) Ferromagnetism in ZnO nanoparticles

induced by doping of a nonmagnetic element: Al. J Phys Chem C 114:13477–13481

22. Claros M, Setka M, Jimenez YP, Vallejos S (2020) Aacvd synthesis and characterization of iron and copper oxides modified zno structured films. Nanomaterials 10:1–16

23. Zeng L, Liu X, Chen X, Soutis C (2018) Surface Modification of Aramid Fibres with Graphene Oxide for Interface Improvement in Composites. Appl Compos Mater 25:843–852

24. Alistair R. Lennie and David J. Vaughan (1996) Spectroscopic Studies of iron sulfide formation and phase relations at low temperatures. Geochemical Soc 5:117–131

25. Descostes M, Mercier F, Thromat N, et al (2000) Use of XPS in the determination of chemical environment and oxidation state of iron and sulfur samples: Constitution of a data basis in binding energies for Fe and S reference compounds and applications to the evidence of surface species of an oxidized pyrite in a carbonate medium. Appl Surf Sci 165:288–302

26. Yamashita T, Hayes P (2008) Analysis of XPS spectra of Fe2+ and Fe3+ ions in oxide materials. Appl Surf Sci 254:2441–2449

27. Wang Z, Li P, Chen Y, et al (2014) Pure thiophene-sulfur doped reduced graphene oxide: Synthesis, structure, and electrical properties. Nanoscale 6:7281–7287

28. Kumar A, Bhattacharyya S (2017) Porous NiFe-Oxide Nanocubes as Bifunctional Electrocatalysts for Efficient Water-Splitting. ACS Appl Mater Interfaces 9:41906–41915

29. Wang J, Han L, Huang B, et al (2019) Amorphization activated ruthenium-tellurium nanorods for efficient water splitting. Nat Commun 10:1–11

30. Wu MF, Hsiao CH, Lee CY, Tai NH (2020) Flexible Supercapacitors Prepared Using the Peanut-Shell-Based Carbon. ACS Omega 5:14417–14426

31. Mitchell E, Jimenez A, Gupta RK, et al (2015) Ultrathin porous hierarchically textured NiCo2O4-graphene oxide flexible nanosheets for high-performance supercapacitors. New J Chem 39:2181–2187

32. Xiang C, Li M, Zhi M, et al (2013) A reduced graphene oxide/Co3O4 composite for supercapacitor electrode. J Power Sources 226:65–70

33. Hu K, Tao L, Liu D, et al (2016) Sulfur-Doped Fe/N/C Nanosheets as Highly Efficient Electrocatalysts for Oxygen Reduction Reaction. ACS Appl Mater Interfaces 8:19379–19385

34. Rodríguez RA, Montoro LA, Ávila Santos M, et al (2020) Impact of phosphorus structural position on the electrochemical enhancement of phosphorus doped LiMn2O4. Electrochim Acta 337:1–9